Thesis for the degree of Doctor of Philosophy

Ionization of large molecules with short laser pulses

Mikael Kjellberg

UNIVERSITY OF GOTHENBURG

Department of Physics
University of Gothenburg
Gothenburg, Sweden 2010

Ionization of large molecules with short laser pulses
Mikael Kjellberg
ISBN 978-91-628-8032-3

Department of Physics
University of Gothenburg
412 96 Gothenburg, Sweden
Telephone: +46 (0)31 772 1000

Chalmers Reproservice
Göteborg, Sweden 2010

Ionization of large molecules with short laser pulses

Mikael Kjellberg
Department of Physics
University of Gothenburg
412 96 Gothenburg, Sweden

Abstract

The decay dynamics of fullerenes and polyaromatic hydrocarbons (PAH) after femtosecond-laser excitation have been studied experimentally by electron momentum mapping and mass spectrometry. The electron spectra of fullerenes and large PAH-molecules were found to be exponentially decreasing with energy without any distinct peaks outside the photon energy. This is interpreted as a statistical electron emission from a transient hot, highly excited, electron system where vibrations are still cold. The smooth electron distributions observed were shown not to be due to tunneling ionization. The photoelectron distributions showed a prolongation along the laser field polarization axis, which was interpreted as field-assisted thermal ionization. For the smallest molecule in the study, anthracene, a transition to atomic like, above threshold ionization, was observed. Molecular fusion of clusters of fullerenes, formed at liquid nitrogen temperature, after fs-laser excitation has also been studied. Products of up to five fused molecules were observed. The mass spectra are the results of several processes including multiple ionization, evaporation of intact fullerenes and post-fusion C_2 evaporation.

Keywords: Photoelectron spectroscopy, Momentum mapping imaging, thermal ionization, above threshold ionization, molecular fusion, fullerenes, polyaromatic hydrocarbons, femtosecond-laser.

Appended Papers

This thesis is partly based on work reported in the following papers, referred to by Roman numerals in the text:

I. M. Kjellberg, O. Johansson, F. Jonsson, A.V. Bulgakov, C. Bordas, E.E.B. Campbell and K. Hansen, *Phys. Rev. A*, **81**, 023202, (2010)
Momentum map imaging photoelectron spectroscopy of fullerenes with femtosecond laser pulses

II. M. Kjellberg, O. Johansson, A.V. Bulgakov and K. Hansen, *Submitted to J. Chem. Phys.*
Femtosecond electron spectroscopy of coronene, benzo[GHI]perylene and anthracene

III. M. Hedén, M. Kjellberg, A.V. Bulgakov, K. Hansen, and E.E.B. Campbell, *Eur. Phys. J. D*, **43**, 255, (2007)
Molecular fusion within fullerene clusters induced by femtosecond laser excitation C_{60}

IV. K. Hansen, M. Kjellberg, A.V. Bulgakov and E.E.B. Campbell, *Israel J. Chem.*, **47**, 43, (2007)
Competition between fission and intra-cluster fusion in highly excited fullerene clusters C_{60}

V. E.E.B. Campbell, K. Hansen, M. Hedén, M. Kjellberg, and A.V. Bulgakov, *Photochem. Photobiol. Sci.*, **5**, 1183, (2006)
Ionisation of fullerenes and fullerene clusters using ultrashort laser pulses

My contributions to the appended papers.

- Paper I: I was responsible for installation of the electron spectrometer. I did the experiments and data analysis and wrote the first version of the paper.
- Paper II: I did most of the experiments and all data analysis.
- Paper III: I participated in the experiments and the data analysis.
- Paper IV: I participated in the experiments and the data analysis.
- Paper V: I was partly responsible for the experiments and data analysis of the "Ionisation and fragmentation of fullerene clusters" section.

Contents

Chapter 1

Introduction

Molecules are very small objects, typically a billion times smaller than a human. Putting it in our perspectives it means that the human is equally big to a molecule as the sun is to the human. Apart from being very small, molecules and atoms also live a very hectic life. In one second I can react and pull my hand away from the hot stove or push the brakes in the car. To a molecule or atom, one second is however a tremendously long time. Take for example the time it takes for an electron to orbit the nucleus, which is about 100 attoseconds (10^{-16} s) or a molecular vibration, typically 10 femtoseconds (10^{-14} s). Those numbers scale to a second as the time since the dinosaur era (200 million years ago) and the time (2.5 million years) it takes for light to travel to our nearest galaxy, Andromeda.

With electron microscopes we can resolve individual atoms in matter and by light interaction we can probe the quantum states of atoms and molecules but there is no camera which is fast enough to see the electrons moving around a nucleus or to see when a molecular bond breaks. However, with the rapid developments of femtosecond- and attosecond-lasers we now have tools that serve as indirect cameras. Such lasers allow researchers to take snapshots of the motion of electrons [1] and study the flow of energy between quantum states in atoms and molecules [2].

Apart from being extremely fast, the short pulse durations of the fs-lasers, imply that the power of the laser pulses are enormous, 10 GW and higher, which is more than the power of most nuclear reactors. The electric field strength is comparable to the Coulomb potential of the atom and gives yet another aspect to fs-laser spectroscopy which is fundamentally different from

traditional laser spectroscopy. Today fs-laser spectroscopy is well developed and used in many different fields in both physics and chemistry, and the rapid development of new lasers which deliver shorter and shorter pulses at higher and higher intensities leads theory and inspires new experiments.

The work presented in this thesis concerns the interaction of large molecules, fullerenes and polyaromatic hydrocarbons in the gas phase, with fs-laser pulses. Compared to state-of-the-art laser technology the laser pulses used here are relatively long, 150 fs, and of moderate intensity. Further, the exact motion of electrons or the exact time of molecular bond breaking are not the interest here. Questions that underlie the work are instead: How do large molecules ionize after intense fs-laser excitation? How many electrons are active in the ionization process? How fast does energy couple between electronic and vibrational states?

Chapter 2

Background

2.1 Ionization dynamics in strong laser fields

The photoelectric effect states that an atom or molecule can be ionized only if the photon energy exceeds the ionization potential of the element regardless of the light source intensity, where multi-photon ionization via long lived resonances is an exception. However, with the ultra short pulse and high intensity laser systems that are available commercially today, a modified version of the photoelectric effect is observed. Multi-photon Ionization (MPI), where the ionization is instant and no intermediate resonances are involved, becomes possible at intensities on the order of 10^{10} W/cm^2, where the exact limit depends on, at least, photon energy and ionization potential [3]. That is, the kinetic energy of the photoelectron is described by $E_k = nh\nu - IP$, where n is the number of absorbed photons, $h\nu$ the photon energy and IP the ionization potential. The ionization rate, Y_n, for MPI is well described by lowest order perturbation theory and is given by

$$Y_n = \sigma_n I^n, \tag{2.1}$$

where σ_n is the generalized cross section and I the laser intensity [4].

At higher laser intensities (I>10^{11} W/cm^2), a pioneering discovery was made in 1979 by Agostini *et al.* where it was observed that photoelectrons can absorb photons in excess of the ionization potential [5]. This is also a MPI-process and was given the name 'above threshold ionization' (ATI). Hence, the kinetic energy for an s-order ATI-electron is

$$E_k = (n + s)h\nu - IP. \tag{2.2}$$

Consequently, an ATI-photoelectron spectrum is dominated by peaks separated by the photon energy, see Fig. 3.7. So far, even though extreme intensities are required, the photon energy together with the ionization potential is the most important parameter to characterize the photoelectron spectrum. But at the highest intensities obtained with focused femtosecond laser pulses, the electric field becomes so strong that it suppresses the binding potential and tunneling or above barrier ionization becomes possible, see Fig. 2.1. These processes will be referred to as field ionization throughout this thesis. A clear indication of field ionization, stated by many studies [6–9], is a transition from an ATI-peaks dominated spectrum to a smooth photoelectron spectrum. Also, in the field ionization regime the photoelectron distribution is, to a large extent, well described by a classical propagation of the electron in the electric field. Field ionization of both atoms and molecules is a well studied area, where the perhaps most interesting, recent, finding is the re-collision [10] of a photoelectron in one optical cycle followed by the generation of high harmonic attosecond light pulses [11].

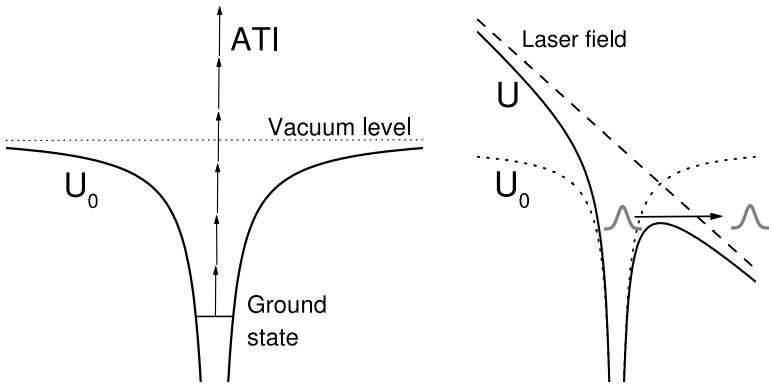

Figure 2.1: Illustration of above threshold ionization (ATI) and tunneling ionization. See the main text for a discussion.

Several theoretical tunneling ionization models such as Keldysh-Fasail-Reiss (KFR) and Ammosov-Delone-Krainov (ADK) have been used to predict ionization rates in the ATI and tunneling regime. Common for those is that they are based on a zero-range potential and a single active electron (SAE) treatment where only the outermost electron is active and all the others are spectators in a frozen core. In fact, the SAE- and zero-range potential based theories can predict ionization rates of rare gas atoms very well [12].

An obvious question is, however, to what accuracy does a zero-range potential describe large molecules and can one assume a single active electron

when there are several delocalized electrons in the system? Several publications on this matter point to a breakdown of the, for atoms so successful theories, when they are applied to larger molecular systems. This will be discussed below.

2.1.1 The ponderomotive energy and the Keldysh parameter

In connection to early experiments on high intensity laser ionization of rare gas atoms there were two parameters introduced which play a decisive role for the ionization mechanism and for the photoelectron spectrum, those of the ponderomotive energy, U_p, and the Keldysh parameter, γ.

The ponderomotive energy, sometimes called quiver energy, corresponds to the energy that a loose electron acquires in an oscillating laser (electric) field. A photoelectron emitted after laser ionization of an atom or molecule, has to traverse the focal volume of the laser field before it reaches the field free vacuum level (this assumes that the ionization takes place during the laser pulse duration). As the photoelectron flies through the laser field it experiences an oscillating force according to the electric field $E{=}E_0\cos(\omega t)$, where E_0 is the amplitude of the electric field, and ω is the frequency. Averaging over an integer number of laser cycles gives the ponderomotive energy,

$$U_p = \frac{q^2 E_0^2}{4 m_e \omega^2} = \frac{q^2 I}{2 c \epsilon_0 m_e \omega^2} \tag{2.3}$$

where q is the charge, m_e is the electron mass, c is the speed of light, I the intensity, and ϵ_0 the vacuum permittivity. Hence, U_p increases linearly with laser intensity and with wavelength squared. For low intensity lasers, nanosecond- and CW-lasers, this is a very small energy and it can safely be ignored in most experiments regarding laser-matter interactions. However, entering the high intensity regime, $>10^{10}$ W/cm^2, which is reached by most amplified femtosecond lasers, the ponderomotive energy can be large and play a central role in the ionization process of atoms and molecules. As an example, an intensity of 10^{14} W/cm^2, which is a typical intensity used in experiments on photoionization of atoms, and a laser wavelength of 775 nm, which corresponds to the fundamental wavelength of the commonly used Titanium:Sapphire fs-laser, gives a ponderomotive energy of 6 eV which is on the order of the ionization potential of an atom.

The ponderomotive potential has been used to explain many signatures in

photoelectron spectra of atoms that are only observed after intense laser ionization. Freeman *et al.* observed that the ATI-peaks in a photoelectron spectrum of xenon were shifted to lower energies as the laser intensity was increased [13]. This was explained in terms of a raised ionization potential due to the laser field. High lying, loosely bound, Rydberg states are AC-stark shifted almost like a free electron in an oscillating field, while low lying, strongly bound states, are AC-stark shifted only slightly. Hence, the effective ionization potential is raised by approximately U_p [14]. This effect can be seen in electron spectra of atoms as long as the laser pulse is not too long. A long pulse would correspond to the case when the laser intensity remains practically constant during the ionization. The emitted photoelectron will in that case regain exactly the same energy, U_p, which was lost inside the atom due to the raised ionization potential, as it leaves the laser field and acquires the quiver energy U_p. In other words, the intensity dependent ionization potential is not observed in the spectra since the energetic losses inside the atom are exactly canceled by the winnings outside the atom. On the other hand, if the pulse is short and changes in intensity during the ionization, then the emitted electron does not have time to accelerate to the same U_p in the laser field outside the atom which means that the ponderomotive shifts inside and outside the atom are not balanced. A schematic picture of the above discussion is seen in Fig. 2.2. The transition from long to short pulses is of course not sharp, but typically a pulse shorter than 10 ps can be considered short for rare gas atoms [13]. The 10 ps can be understood as the time it takes for a photoelectron with kinetic energy in the 10 eV range to travel through the focal volume of the laser beam which, typically, is on the order of 20 μm. The time it takes for the electron to leave the atom (ca. 1 Å) is on the other hand only on the fs-timescale.

To characterize the laser pulse duration as long or short by considering the ponderomotive shifts of ATI peaks does however seem to depend on the atomic or molecular system as well. In [9] the photoelectron spectra of C_{60} ionized with a 25 fs, 790 nm, laser are studied for different laser intensities. The intensities in the ATI-regime span a range from 3.7×10^{13} W/cm^2 to 7.5×10^{13} W/cm^2 corresponding to ponderomotive energies of 2.16 eV and 4.37 eV respectively. But even though the ponderomotive shifts are this large the ATI peaks are seen to just slightly wiggle on the energy scale with at maximum ca 0.2 eV. In fact, all the photoelectron spectra of the molecules, C_{60}, C_{70}, coronene, benzo[GHI]perylene and anthracene reported in this thesis do confirm the observation that ATI-peaks do not move on the energy scale as laser intensity is varied. Already at this point it is clear that rare gas atoms and molecules ionize differently and it is clear that applying the

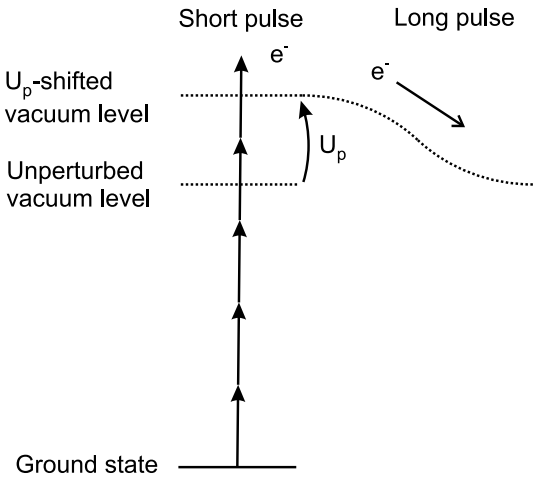

Figure 2.2: Illustration of the effect of the ponderomotive energy in the short and long pulse regime. See the main text for a discussion.

models developed for rare gas atoms, discussed in this chapter, to molecules is questionable.

In a similar way, as discussed above, the ponderomotive energy shift was used to explain the observed resonances inside ATI peaks and also the broadening of ATI peaks in xenon photoelectron spectra after intense multi-photon ionization with short laser pulses [13, 15–17]. Due to the spatial profile of the laser pulse the ponderomotive shift is not the same over the whole focal volume. This means that electrons are emitted from atoms with different effective ionization potentials which gives a broadening of the ATI-peaks. Also, at different positions in the laser focus, different Rydberg states of the atom are driven into resonance with a number of photons from which the atom is ionized, resulting in resonance-peaks inside the ATI-peaks. For the same reason as stated above these effects are not seen for long pulses.

A third, high intensity effect, related to the ponderomotive shift is peak suppression [18]. In photoelectron spectra of xenon, in the long pulse regime, it was observed that the lowest order ATI-peaks were strongly suppressed. The reason for this is that due to the increased ionization potential the first order ATI-electrons cannot reach the vacuum level. High order ATI-electrons on the other hand are released from the atom into the laser field where they gain quiver energy and end up in the photoelectron spectra at a position corresponding to a non-ponderomotive shift. This will create a gap in the photoelectron spectra at low energies.

As was discussed above, the ionization mechanisms change drastically from the perturbative regime to the ATI and field ionization regimes as the laser intensity is increased. To distinguish between ATI- and field ionization and to give a reference point on the intensity scale for the transition from multi-photon ionization to field ionization, the Keldysh parameter, γ, is commonly used in high laser intensity experiments. The Keldysh theory for tunneling ionization rates is based on dc-tunneling ionization and a zero-range potential [19]. If the laser frequency, ω, is low enough so it can be considered static for the valence electrons and the peak intensity is high enough to bend the Coulomb potential to the extent that the probability for an electron to tunnel through the barrier is significant, the Keldysh parameter is simply the ratio of the tunneling frequency, ω_t, and the optical frequency. This can be expressed in terms of ionization potential, IP, and the ponderomotive potential as

$$\gamma = \frac{\omega}{\omega_t} = \sqrt{\frac{IP}{2U_p}}. \tag{2.4}$$

If $\gamma \gg 1$, the multi-photon ionization mechanism is considered to dominate and if $\gamma \ll 1$ the field ionization mechanism dominates.

Even though, as will be discussed below, the relevance of the Keldysh parameter when applied to molecular systems is unclear, it will be used as reference point throughout this thesis. Attempts have been made to introduce size dependent γ-values. Those calculations point to a reduced value of the Keldysh parameter which means that molecules would field ionize more easily than atoms [7]. However, experiments on large molecules like ethene, propane, propyne, benzene, toluene and methanol [20, 21] and long chain molecules; hexatriene, decatetraene and β-carotene, suggest a screening effect of the electric field due to the large extent of delocalized electrons and consequently a decreased probability for field ionization [20–22].

2.2 Short pulse, high intensity, ionization of molecules

The interaction of large molecules of many different kinds with intense ultrashort laser pulses is frequently studied [7–9, 20–39], even though not to the same extent as atoms and diatomic molecules. Most of these studies focus on the absolute, positively charged, ion yields and whether the above discussed

theoretical models for laser-atom interactions can be applied to large molecular systems. Many of those high intensity effects that are observed for atoms, like ATI and field ionization, are also observed for molecules. But there are also major differences observed. Below follows a summary of selected publications where the difference between atomic and molecular ionization is observed. The concept of *hot electron thermal ionization* is also introduced, which is the underlying understanding of the experimental results reported in this work.

Alcohol and chain molecules

D. Mathur *et al.* and T. Hatamoto *et al.* have measured photoelectron spectra of methanol, ethanol and 1-propanol upon 100 fs laser radiation at wavelengths 400 nm and 800 nm and at different peak intensities [8, 23]. It is observed, in the case of 800 nm radiation, that these molecules behave similar to atoms in the sense that a transition from ATI dominated spectra to smooth spectra occurs at $\gamma \approx 1$, rather than at the same laser intensity. Also plateaux like structures are observed in the spectra, similar to those of rare gas atoms [40]. A small change of the γ value, 0.8 for methanol and 1.2 for 1-propanol, is observed for the ATI to field ionization regime transition. Hence, a small structure dependence of the γ-parameter could be considered even though it is not nearly as dramatic as in the case of polycyclic aromatics, reported by Dewitt and Levis [7], where for example the γ-value for anthracene at a field strength of 0.75 V/Å changes from 3.08 to 0.47 by introducing a length correction. By changing the wavelength to 400 nm, and consequently also lowering the optical field strength and moving away from field ionization, the authors find a dramatic change of the photoelectron spectra. The characteristic structures ($2U_p$ and $10U_p$ cut offs and a plateaux [6]) due to classical propagation in the field ionization regime are now gone and the ATI peaks are superimposed on a smooth "baseline" of exponential character. This baseline increases in magnitude relative to the ATI-peaks as laser intensity is increased and it is also more prominent for the largest molecule in the study, 1-propanol. The origin of this baseline is not given but could be due to inelastic rescattering of the electron wavepacket according to the authors. Another explanation for this baseline is thermal ionization, see below.

Lezius and co-workers have studied the response of the linear molecules; hexatriene (HT), (C_6H_8), length 7.2 Å, decatetraene (DT), ($C_{10}H_{14}$), length 13.5 Å and β-carotene (βC), ($C_{40}H_{56}$), length 32 Å, to 40 fs laser ionization in the wavelength range 400-1500 nm by mass spectrometry [22, 24]. These

molecules have similar electronic structures so the main difference between them is that they are different in size and number of constituent atoms. It is observed that, regardless of wavelength, the mass spectra for the smallest molecule in the study, HT, are dominated by intact mother ions of single and multiple charge states, which is in good agreement with what would be expected from a quasi-static field ionization process of one active electron. For the second largest molecule, DT, the fragmentation pattern is strongly wavelength dependent, with strongly enhanced fragmentation for short wavelengths and for βC, heavy fragmentation is observed at all intensities and at all wavelengths. These two findings are inconsistent with an adiabatic, SAE, field ionization process since it is wavelength independent and would have resulted in a much more intensity dependent fragmentation than what is observed. Instead a Non adiabatic Many Active Electron process (NMAE) is used to explain the observed fragmentation spectra. Highly, multiply excited ions of single or multiple charge are produced from which heavy fragmentation sets in after the laser pulse has passed. In fact, for the largest molecule, βC, the authors argue that NMAE is the dominant ionization process even in the classical field ionization regime of γ-values smaller than unity. Further it was shown that the molecule cyclooctatetraene, COT, which is a ring-shaped molecule with the same number of delocalized π-electrons as DT does not ionize to equally high charge states as DT and almost does not fragment at all. This indicates that it is not the number of electrons that is the crucial parameter for the ionization and fragmentation process, but rather the electronic and/or geometric form of the molecule.

Cyclic aromatic molecules

Merrick *et al.* [7, 25] and Markevitch [26] have studied the ionization and fragmentation processes for cyclic aromatic molecules after fs-laser radiation. In [7] benzene, naphthalene and anthracene were interacting with a 780 nm, 170 fs laser at varying intensities. At 3.8×10^{13} W/cm^2 a transition from an ATI-dominated photoelectron spectrum for benzene, to a smooth spectrum of exponential form for anthracene, was observed. It was explained in terms of a superposition of ATI and tunnel ionization spectra where the tunnel ionization probability grew relative to ATI for larger molecules. According to the Keldysh parameter, γ, this interpretation is incorrect since these molecules have similar γ-values at identical laser intensity. But it was shown with a numerical model assuming a one-dimensional potential, that the Keldysh parameter is strongly structure dependent and that large molecules reach the field ionization region already at $\gamma>1$. For example, at field strengths of 0.75 V/Å the structure dependent γ-value for anthracene is 0.47 instead of

3.08 for the ordinary calculated γ. These arguments were strengthened by ion yield measurements where it was shown that the ion yields of benzene, naphthalene and anthracene fit well with the new structure-dependent field ionization model [26]. The arguments were based on the observation that the fragmentation and kinetic energy release of small fragments increases super-linearly with the number of atoms in the molecule, indicating that the molecule interacts with the laser field as a whole and not as independent substructures leading to larger energy deposition in big molecules. Hence, it was concluded that the tunneling ionization rates and the Keldysh-parameter are structure dependent.

However, later experiments on organic molecules [20] and also the experiments performed by Lezius *et al.* suggest the opposite, that it is harder to field ionize large molecules due to a screening effect induced by the delocalized electrons [22, 24].

The fragmentation pattern of anthracene after fs-laser irradiation was examined by Murakami *et al.* [27, 28]. In [27] it was found that heavy fragmentation follows 800 nm excitation but with 1400 nm laser light the mother ion stays intact or just a small amount of fragmentation was observed. Charge states up to 3+ were observed at the highest intensity used, 5.0×10^{13} W/cm^2. It was suggested that the strong fragmentation is due to a resonance with electronic levels at 800 nm. It was further concluded that the fragmentation is not due to recolliding photoelectrons since the 1400 nm light in that case would result in the heaviest fragmentation. The resonance enhanced fragmentation argument was further strengthened in [28] where anthracene was exposed to circularly and linearly polarized 800 nm laser light. A higher yield of fragment ions was found for circularly polarized light. This is in contrast to what has been observed for C_{60} with 1500 nm light [29] where rescattering of photoelectrons was the reported mechanism behind the enhanced fragmentation for linearly polarized light. The explanation for the opposite results in [28] is that when the randomly oriented gas phase molecules are in line with the laser field polarization, fragmentation is induced by the resonance of the ${}^2A_u \leftarrow {}^2B_{2g}$ transition. This will always be the case for circularly polarized light but in the case of linear polarization the transition will be forbidden when the molecular axis and light polarization are perpendicular to each other which will result in a suppressed fragmentation.

$\mathbf{C_{60}}$

One of the most studied large molecules in the area of fs-laser excitation

and relaxation is the C_{60} fullerene. Below follows a summary of some of the studies from year 2000 and forward. Also the concept of thermal ionization of hot electrons will be introduced in connection with the reports on C_{60}.

In [9, 30] C_{60} was ionized with 800 nm and 400 nm fs-laser pulses with durations shorter than 70 fs at different intensities. It was found that the ion yield for all charge states followed the simple power law, equation 2.1, below saturation, and the authors therefore argued that C_{60} ionizes sequentially for these laser parameters. It was further concluded that tunneling ionization rates, calculated from ADK-theory, are orders of magnitude wrong compared to the experimental data and that such a model is not applicable even though the threshold for barrier suppression, calculated for atoms, is reached at the intensities used here. Once again, the proposed reason for that is the effective screening of delocalised electrons resulting in a raised threshold for field ionization. Further it is observed from photoelectron spectra that the transition from ATI-dominance to a smooth distribution happens at γ-values around unity. Hence, the previous suggested, size-corrected Keldysh parameter for cyclic aromatic molecules, seems not to be needed for C_{60}.

Even though the results in [9, 30] suggest that a SAE multi-photon ionization process is likely to be correct for these short and intense pulses the results of Shchatsinin *et al.* [31–33], where C_{60} is ionized with sub-30 fs laser pulses, points to a more complex scenario. In [31] it is suggested that the adiabatic SAE-picture is likely to be correct only for the first charge state. This statement is based on ion yield measurements that deviate from a I^n power law, where I is the intensity and n the minimum number of photons required to reach the specific charge state. The authors interpret this as an indication of multielectron dynamics in C_{60} and argue that the plasmon resonance [41] is involved in the onset of NMAE. It is however not clear how a number of 387 THz pulses adds up to a 4800 THz oscillation which is the center of the plasmon resonance in C_{60}. It was further observed that the autocorrelation function in a pump-probe scheme had a wider full width half maximum for C_{60} than for xenon where a SAE is expected. Shchatsinin *et al.* reported further evidence for multielectron dynamics in C_{60} after ionization with elliptically polarized fs-pulses [32]. It was observed that the polarization dependence was much stronger for ionization of xenon compared to C_{60}. For xenon, the ion yield peaks at linear polarization and drops going to circular polarization. The drop is consistent with a 8-photon ionization process, where 8 is the minimum number of 1.6 eV photons required to ionize xenon. This is understood in terms of a coherent ionization process for xenon. Going to C_{60}, the laser polarization dependence on the triply charged ion yield

fitted with a coherent two photon process, where an 11-photon process is expected. With 3.2 eV photons no ellipticity dependence is observed at all. The authors consider this to be evidence of a non coherent multielectron excitation process for C_{60}.

In [33] two-color pump probe experiments on C_{60} are presented. It is observed that with a weak 399 nm pump pulse and a strong 797 nm probe pulse the ion yield is greatly enhanced compared to the opposite order of the pulses. It is argued that the 399 nm prepares the molecule in a highly excited state where energy is shared between both electronic and nuclear degrees of freedom.

2.2.1 Thermal ionization

The above summary of publications regarding excitation of large molecules by fs-lasers all show a breakdown of the single active electron approximation and it is clear that multiple electrons are excited in these super intense fields. The natural question to ask now is how do multiply excited molecules ionize? There is no clear answer to that question but in this section a thermal ionization process will be described which is the way that the results presented in this thesis are understood and argued for.

In [34] photoelectron spectra of C_{60} were presented for different laser pulse durations ranging from 25 to 5000 fs. The wavelength was 790 nm. It was shown that the shortest pulse durations, <70 fs, give rise to ATI-dominated electron spectra, which is in agreement with what had been reported previously [9, 30]. Also, the corresponding mass spectra are dominated by intact C_{60} ions of different charge states. From these two observations it was concluded that the molecules ionize promptly in a MPI process where any excess energy is carried away by the photoelectrons. But as the pulse was stretched to durations in the 100-1000 fs time window the ATI-peaks were strongly suppressed and replaced by a structureless distribution of exponential form. For these pulse durations another ionization process becomes active. The absorption of photons is now slow enough for the excitation energy to dissipate into the electronic degrees of freedom of the fullerene, creating a highly excited, thermally equilibrated, electron system, which, due to the low heat capacity of electrons, can reach extremely high temperatures, on the order of tens of thousands of Kelvin. If an electron is emitted from this hot electron

bath, it is called *transient hot electron emission* and can be described statistically [34, 35, 42]. The extreme heating of the electron system is only short lived, up to a picosecond approximately. After that time this decay path disappears when energy couples between the electronic system and nuclear vibrations. Energy is assumed to leak from the electronic to the vibrational system with a characteristic time constant of 240 fs in C_{60} [35], which is on the order of a vibrational period (longest and shortest observed vibrational periods are 122 and 21 fs respectively [43]). This was verified by the mass spectra in [34] where the onset of heavy fragmentation appeared at ca 500 fs.

On the timescale of electron motion, which is on the order of femtoseconds or less, the thermal ionization is a delayed process. But on the timescale of a mass spectrometer, which typically has a resolution, at best, in the nanosecond range, it can be considered as a prompt process. Notice that the description of this ionization process does not involve any specific states or resonances like the plasmon resonance. The transient hot electron ionization process is described in detail in [35]. The emission process is described with detail balance which was originally inspired by Weisskopf's work on statistical emission of neutrons from excited nuclei [44] and also used to describe nanosecond thermal ionization [45].

As the pulse duration was extended to 5 ps in [34] delayed ionization [46], characteristic for thermionic emission, and the bimodal fragmentation [47] pattern which is characteristic for ns-ionization of fullerenes was observed in the mass spectra. Also multiple charge states were no longer present and the electronic temperatures were lower. Hence, energy is now equilibrated in both electronic and vibrational degrees of freedom and electron emission and fragmentation processes are purely statistical [45, 48–53].

Other systems where the transient hot electron ionization has been observed are for example sodium clusters in the gas phase after fs-laser irradiation [54, 55] and it has also been used to rationalise the fragmentation pattern obtained subsequent to fusion of fullerene clusters in the gas phase after fs-laser excitation (see chapter 7). It is also closely analogous to the two-temperature model [56], frequently used in solid state experiments to interpret sub-picosecond relaxation processes of solids after fs-laser irradiation. [57–61].

An interesting parallel to the idea of equilibration of energy in the electronic systems of molecules is discussed in [62–64], this time for atomic ions. In these studies the whole electronic system of Au^{25+}, after electron recombina-

tion, is considered to be excited. For atoms there is of course no quenching of energy to vibrations so the excess energy from the recombination is emitted either via electron or photon emission. The authors show, theoretically, that the rate of electron emission is about 200 times higher than the photon emission and that the spectrum of emitted electrons from the highly excited ion is of thermal nature. The key point in this theory is a strong interaction between the electrons of the outer unfilled electron shell, and the authors point to a many body quantum chaotic system.

Electronic temperature fits

The apparent electronic temperature, T_a, which is frequently mentioned in the following chapters to describe and understand the photoelectron spectra, will be defined here. As discussed in the section above, "Thermal Ionization", the spectra of thermionic and transient hot electron emission resemble the shape of a Boltzmann distribution,

$$P(\epsilon) \propto \mathrm{e}^{-\epsilon/k_b T_a}. \tag{2.5}$$

where ϵ is the electron kinetic energy and k_b is Boltzmanns constant. k_b is set to 1 for convenience throughout this thesis and electronic temperatures are therefore given in units of eV. Equation 2.5 is just an approximation but gives a robust estimate of the electronic temperature for the interpretation of the electron spectra. For a rigorous discussion and the definition of a temperature in a microcanonical system see [35, 45].

The electronic temperatures are extracted from linear fits in semilogarithmic plots of the photoelectron distributions. The fits range from the photon energy out to the noise level. In a few of the electron spectra where strong peaks appear at high kinetic energies, the temperatures are estimated by eye.

Chapter 3

Experimental setup & analysis

3.1 Time of flight mass spectrometry

The mass spectrometer used in this work is a time of flight spectrometer (ToF). The principle of a time of flight mass spectrometer is to accelerate all ions to the same kinetic energy and then let them fly the same distance, in a field free region, to a detector. The ions are accelerated by an electric field to a kinetic energy $E = qU$, where q is the charge of the ion and U is the acceleration potential. There are no relativistic effects involved so we can simply put $qU = mv^2/2$, where m is the mass of the ion and v is the velocity. The velocity and flight time of the ions is thus only dependent on their mass to charge ratio. So, when the ions arrive at the detector they do so in bunches of constant mass to charge ratios. This will show up as peaks on the detector's time axis. By assigning the mass to known peaks in the time of flight spectrum it can be converted to a mass spectrum.

A schematic picture of the time of flight setup in Göteborg is seen in Fig. 3.1. It consists of two differentially pumped chambers, the interaction chamber and the flight chamber. The molecular source is placed in the interaction chamber. It is a resistively heated copper block which creates an effusive molecular beam. The molecular beam interacts with a laser field, perpendicularly aligned, between two electrodes named, HV1 and HV2. Ionized molecules are accelerated towards the flight chamber by a static electric field which is applied between the electrodes. Typically HV1=4.6 kV and HV2=3.1 kV. The potential on the third electrode is half the potential of HV2 and the fourth and final electrode is grounded. Further details are de-

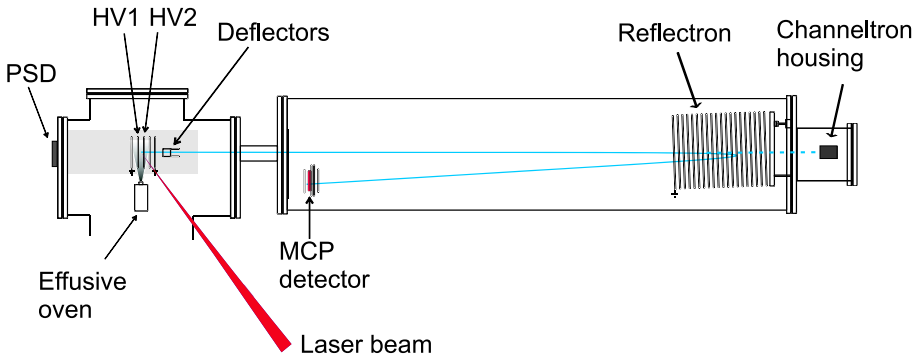

Figure 3.1: Schematic figure of the Time of Flight setup. See main text for details. Figure adapted from [66].

scribed in Paper I. After the acceleration stage there are two sets of deflection plates. These are used to steer the ion beam, vertically and horizontally, towards the detector. Deflection voltages are on the order of 100 V.

The second chamber is a 2 meter long field free flight chamber where the ions are separated in time according to their mass to charge ratio. The spectrometer can be used as a linear ToF, or as a Reflectron Time of Flight spectrometer (ReToF). The reflectron is placed at the end of the flight chamber. The reflectron consists of a long series of electrodes, where the ions experience a smooth increase of the retardation field. The first electrode is grounded and the second electrode usually put at 1.5 kV. From there the potential gradually increases for every electrode up to 4.6 kV on the last one. After the reflectron the ions fly back to the other end of the flight chamber where they are detected by a dual Multi Channel Plate detector. A -2 kV potential is typically applied over the MCPs and the detector is floated to -500 V. If the voltage over the reflectron is put to zero the ion beam simply goes through it and is detected by a channeltron at the end of the flight chamber. The channeltron is placed in a housing, on which a -2.1 kV potential is applied. The dynode of the channeltron is put at -2.4 kV.

At the spot of ionization the molecules have a spatial and kinetic energy spread. Some molecules will have a slightly longer flight distance than others and there will also be a spread in thermal velocity of the molecules. By tuning the ratio HV1/HV2, the shape of the acceleration field changes and one can correct for the spatial distribution and thus get a finer resolution [65].

The reflectron is used to improve the resolution due to the initial spread

in velocity. Ions with a higher velocity will spend more time in the reflectron compared to the ones with a slightly lower velocity. In this way ions of the same mass to charge ratio hit the MCP detector simultaneously. The reflectron can also be used to detect metastable fragments by detuning the electric field away from the values for optimal mass resolution [66].

A single ion counter card (FAST), of 125 ns channel width was used to record the signal from the detector in this setup. The mass resolution of the ReToF, $\delta m/m$ is over 300. Using the single ion counter it is reduced by a factor 3 because of the reduced digital resolution. One spectrum presented in chapter 5 was recorded with an oscilloscope (Tektronix TDS 520) of higher resolution, 500 MHz, than the counting card.

The laser beam focus was adjusted to be in the center of the acceleration stage of the spectrometer, above the center of the effusive oven.

By scanning the voltage of the deflection plates, different parts of the molecular ion beam can be selected. At most laser intensities the laser field is strong enough to ionize even slightly out of focus. The deflection voltage was therefore adjusted to give the highest yield of doubly charged ions, at relatively low laser intensities, in the mass spectra. This condition is assumed to correspond to the absolute focus of the laser beam.

The mass spectra are not corrected for the different detection efficiency of heavy and light ions. Therefore the yield of large ions is underestimated relative to the lighter ions of the same charge.

3.2 The momentum map electron spectrometer

The electron spectroscopy measurements reported in this thesis are done with a Momentum Map (MM) spectrometer, also called Velocity Map Imaging spectrometer (VMI). The momentum mapping technique has become a popular tool in many spectroscopy fields during the last decades and was first introduced by H. Helm *et al.* in 1993 [67]. There are two advantages with this type of spectrometer compared to a conventional time of flight electron spectrometer. It can measure very low kinetic energy electrons, below 0.1 eV, where the time of flight spectrometer fails. Secondly it gives the full three dimensional picture of the ionization dynamics. A time of flight spectrometer

will only give the energy spectrum, while the momentum map spectrometer in addition gives information about the angular distribution, relative to the laser polarization, of the photoelectrons studied.

3.2.1 The principle of momentum imaging

In contrast to the time of flight spectrometer where the kinetic energy information comes from the arrival time of electrons at a detector, the momentum mapping technique reveals the kinetic energy and angular distribution of the electrons from a two dimensional image. In Fig. 3.2 the principle of the momentum mapping method is shown. The interaction between the laser field

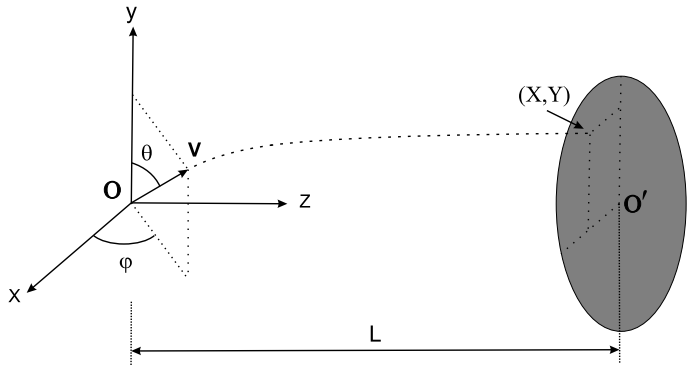

Figure 3.2: Principle of the momentum mapping detector. See main text for a discussion.

and the target atoms/molecules takes place at point *O*. All photoelectrons with a certain kinetic energy, ϵ, will at some time, t, after ionization be found on the surface of a sphere of radius $r=\sqrt{2\epsilon/m}t$, where m is the electron mass. An electric field, **F**, collapses the photoelectron sphere on a screen, which is positioned a distance L away from the ionization spot, *O*. The further away from the center, *O'*, of the screen the electrons hit, the higher kinetic energy they have and depending on what angles φ and θ the electrons are emitted with, they will hit the screen at different positions.

3.2.2 Experimental

The experimental details of the electron spectrometer and the experimental procedure are described in section II of Paper I together with a schematic

figure. Some additional remarks not stated in the paper follow here.

The HV2 and the grounded electrode before the field free region have no meshes. That results in curved equipotential surfaces and for the right ratio of HV1/HV2 spatial focusing is achieved and photoelectrons of the same momentum are mapped onto the same coordinate (X,Z). This limits the spatial smearing of the photoelectron distribution which is present in Time of Flight spectrometers [68].

Neither the MCP nor the camera are triggered to the laser. The fact that MCPs are constantly active implies that direct and delayed photoelectrons are recorded in the same image. If only photoelectrons in a specific time window should be studied the detector needs to be synchronized with the laser. Electronic gating can however not be done on the fs-time scale but can be easily achieved on the ns-timescale [69].

3.2.3 The inversion method and calculation of a photoelectron spectrum

The image on the screen in Fig. 3.2 is a projection of a sphere of electrons and it is clear from the figure that photoelectrons of a speed, $|\mathbf{v}|$, but emitted at different angles, θ and φ, will end up at different positions (X,Y) on the screen. So to get the original 3D-photoelectron distribution it has to be reconstructed from the projection. That is possible if the photoelectron emission is isotropic (purely statistical) or in the case of direct emission if the laser polarization is linear, so that the emission is rotationally symmetric around the polarization axis. Suppose that the laser field in Fig. 3.2 propagates in the x-direction and is linearly polarized in the y-direction, then the photoelectron distribution is rotationally symmetric around the y-axis and independent of the angle φ. Hence, to reconstruct the full 3D-distribution it is enough to know the distribution of a slice, $\varphi = 0$, of the photoelectron sphere. The inversion algorithm used here for this purpose is called "direct back projection" and is described in detail in [70]. The analytical equivalence to this method is an inverse Abel transform. The inversion algorithm was written in MATLAB code and tested on simulated distributions in the Masters's thesis of Olof Johansson [71], with a later minor correction. The only input required is the projected image, G(X,Y). Through a back projection operator, $\mathcal{G}$ which integrates over φ, the slice, G($|\mathbf{p}|$,θ), of the 2D-distribution at $\varphi = 0$ is calculated, where $|\mathbf{p}|$ is the absolute value of the photoelectron's

momentum and θ is the emission angle relative to the laser polarization axis.

Multi-photon ionization of rare gases by pico- and femtosecond laser pulses has been studied extensively [13, 15, 17, 72] and provides a good reference to test the spectrometer and inversion algorithm. In Fig. 3.3 the effect of the inversion algorithm is demonstrated. Figure 3.3 **a** shows the projected image, G(X,Y), of photoelectrons of ionized xenon atoms. Figure 3.3 **b** shows the slice, G($|\mathbf{p}|$,θ), of the original 3D-distribution obtained with the inversion algorithm. In this figure the angle θ is the angle between momentum axes $\mathbf{p}_x$ and $\mathbf{p}_y$, where θ=0 corresponds to $\mathbf{p}_x$=0. The absolute momentum, $|\mathbf{p}|$, of the photoelectrons is directly proportional to the distance to the center of the image and hence, the kinetic energy of the photoelectrons is proportional to the square root of the distance. The momentum maps of xenon in Fig. 2 of Paper I and Fig. 3.7 can in a satisfactory way be compared to images presented in [17] for similar laser intensities. To obtain an ordinary photoelectron spectrum G($|\mathbf{p}|$,θ) is integrated over θ. This is shown in Fig. 3.7.

To energy-calibrate the photoelectron spectra (PES) the ATI-rings in the xenon spectrum, which are $h\nu$ separated, are utilized for a conversion from the CCD-chip pixel units to eV, see Paper I. The calibration is unique for every projection field, laser beam/molecular beam alignment and camera position. It is therefore always performed before every photoelectron measurement.

3.2.4 Detection efficiency and symmetrization

Ideally, the projected electron distribution should be symmetric around the laser polarization and propagation axes and the four quadrants (A1-A4) seen in Fig. 3.4**a** should be identical. Therefore, as stated above, only one quadrant needs to be inverted to get the photoelectron distribution. In reality the detection efficiency of the PSD is however not the same for the four quadrants and the projection of the electron cloud cannot be assumed perfect.

All the photoelectron spectra reported in this work are extracted from a symmetrization of the four quadrants of the raw image, defined as (A1+A2+A3+A4)/4. The effect of symmetrization will be discussed with reference to Fig. 3.4- 3.7. In Fig. 3.4**a** the raw image of projected photoelectrons from C_{70} ionized with the ns-laser is shown. It is well known that the dominant ionization channel of fullerenes after ns-laser excitation is thermionic emission. This means that the projected photoelectron cloud should be isotropic

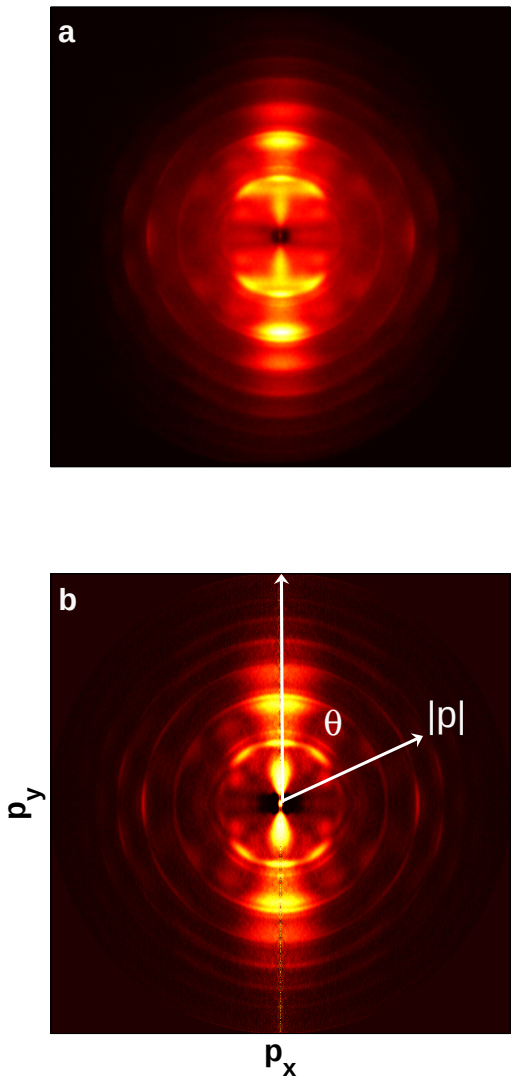

Figure 3.3: Photoelectron momentum map of xenon ionized with the 150 fs, 775 nm laser at peak intensity 9.8×10^{13} W/cm^2. **a**: raw image and **b**: inverted image. The laser polarization is in the y-direction. The absolute momentum, $|\mathbf{p}|$, is proportional to the radius and the emission angle θ is indicated relative to the laser polarization.

and the image in Fig. 3.4**a** completely symmetric. In Fig. 3.4**b** the four quadrants of the raw image have been divided into angular segments of 2° and the counts in those segments have been integrated. Quadrants A2, A3 and

A4 are shifted by factors 1.2, 1.4 and 1.6 respectively for display purpose. The detection efficiency shows no angular dependence, in agreement with an isotropic distribution. In Fig. 3.4**c** and **d** the same thing is shown but now the counts are integrated from 1.0 eV and 2.5 eV respectively. We are now much closer to the noise level of the detector but the detection efficiency still shows no major divergence from an isotropic distribution. A comparison with the distributions shown in Fig. 6.3 in chapter 6 also shows that the detector inhomogeneity is minor compared to the effect of laser polarization. The conclusion of these figures is that in terms of detection efficiency the symmetrization serves to improve the image and even out angular dependencies in the detector. It should be noted that the projection field is 2.3 times lower for the ns-spectrum in Fig. 3.4 compared to the fs-spectra below in Fig. 3.6 and 3.7 so even though it does not cover the same kinetic energy range it still covers the same detector area.

The next question is how the symmetrization of the raw image affects the photoelectron spectra. The PES corresponding to the image in Fig. 3.4**a** is shown in Fig. 3.5 for the four quadrants A1-A4, the average of these distributions, 'ave', and the PES of the symmetrized image, 'sym'. Below ca. 0.1 eV the distributions are clearly different which is caused by the electrons being emitted from a finite focal volume, creating a slight ellipticity at the center (This is a general problem using too energetic photons with the setup in Göteborg since they ionize from a larger focal volume). Apart from that, thermal distributions are obtained from all quadrants as well as from the symmetrized image, which is in agreement with a thermionic emission process. Thermal fits are seen as dashed lines with temperatures given in the caption of Fig. 3.5. There is no major difference between the four quadrants and the symmetrized image gives a PES with a temperature close to the average.

The same analysis of the symmetrization is shown again in Fig. 3.6 but here for 775 nm, 150 fs laser ionization and for coronene at 2.11×10^{13} W/cm^2. These spectra contain photoelectrons with much higher kinetic energies and have a higher count rate close to the edge of the detector, compared to the C_{70} ns-PES above. The effect of a too high count rate close to the detector edge is most clearly demonstrated in the coronene spectrum where the A2 and A4 spectra are seen to bend at energies above ca 8 eV. This effect is most prominent in the measurements on PAH molecules (chapter 5) since the count rate was much higher here than in the fullerene measurements (chapter 4). It does however not affect the interpretation of the measurements but the end point data should be interpreted with care and electronic

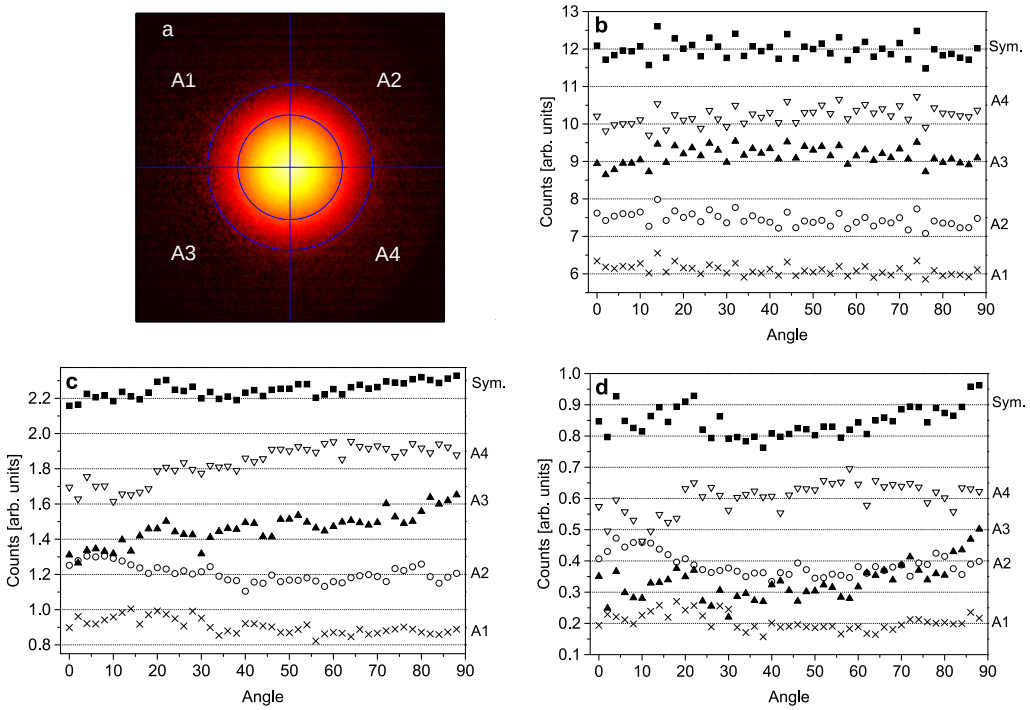

Figure 3.4: **a**: Raw image of C_{70} ionized with the nitrogen ns-laser (described below). The projection field, HV2/HV1, is -1000V/-670V. A1-A4 are the names of the four quadrants around the symmetry point, indicated by the cross and defined by the laser polarization and propagation axes. Blue circles corresponds to 1.0 eV and 2.5 eV. **b**: The four quadrants are divided into segments of 2° and the number of counts are integrated. Angle 0 is in the y-direction. A1: Crosses, A2: Circles, A3: Solid up triangle and A4: Open down-triangle. A2, A3 and A4 are shifted by factors 1.2, 1.4 and 1.6 respectively for display purposes. The solid squares correspond to a symmetrized image which is defined as (A1+A2+A3+A4)/4. These points are also shifted in magnitude. **c**: Same as **b** but from 1 eV and out. **d**: Same as **b** but from 2.5 eV and out.

temperatures are therefore only fitted to where the spectra bends off.

The electronic temperatures of the different quadrants are given in the caption of Fig. 3.6. Similar discrepancies are observed for other spectra. The symmetrized image is used to cancel the errors to first order.

Finally in Fig. 3.7 the same analysis as above has been done for the PES of xenon. The vertical dotted lines are separated by the photon energy, 1.60 eV. At high energies, above 8 eV, the A1 quadrant is shifted to low

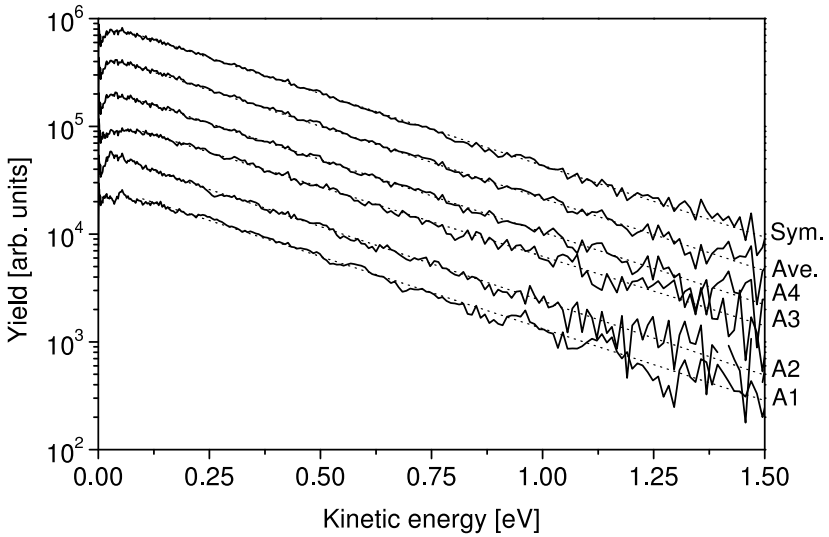

Figure 3.5: The photoelectron spectrum of C_{70}, obtained from the image in Fig. 3.4**a**. From bottom to top the spectra correspond to quadrant A1, A2, A3, and A4. "Ave" is the average spectrum of the 4 bottom spectra. Spectrum "Sym" is calculated from the symmetrized raw image. The electronic temperatures are; A1=0.32 eV, A2=0.31 eV, A3=0.34 eV, A4=0.32 eV, with a mean value of 0.32±0.003 eV. The temperature of the average,"ave" is 0.32 eV and the temperature of the symmetrized raw image, "sym", is 0.33 eV. The spectra are shifted in magnitude for display purposes. See section 2.2.1 for the definition of the electronic temperature and how it is extracted from the electron spectra.

energies compared to the others. The shift is on the order of 1-2%, consistent with the uncertainties in finding the center of the image, and results in a smearing of the spectra at the edge of the detector. The electronic temperatures measured here for ns-laser ionization of C_{70} and C_{60}, see Paper I, are similar to what was reported for ns-laser ionization of C_{60} in [53]. Also the photoelectron spectra, electronic temperatures and temperature dependence on laser fluence of C_{60} after fs-laser ionization, reported in Paper I, are similar to those of [35] and therefore confirm that the momentum map detector operates satisfactory. At the end point, close to the detector edge, the spectra are however not reliable.

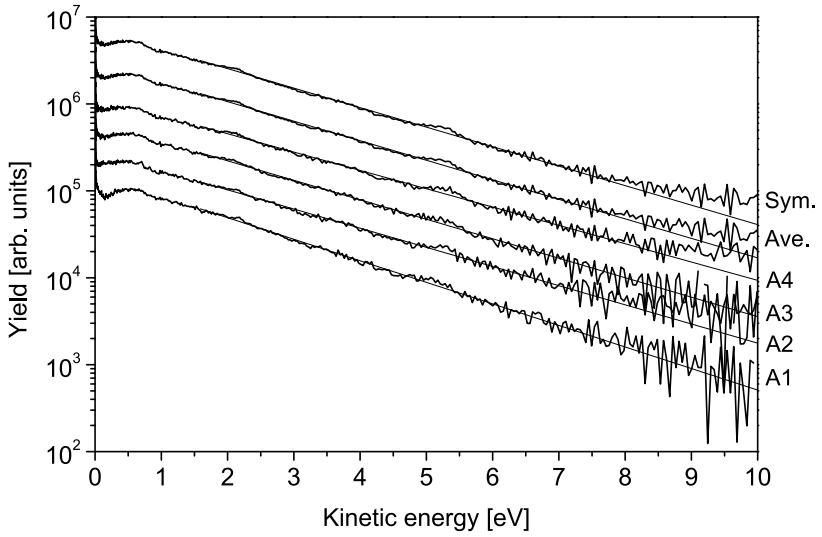

Figure 3.6: Same as in Fig. 3.5 but here 775 nm 150 fs-laser ionization of coronene at 2.11×10^{13} W/cm^2. The projection field is -2300V/-1500V. Electronic temperatures are for coronene; A1=1.75 eV, A2=1.97 eV, A3=1.94 eV and A4=2.06 eV with a mean value of 1.93±0.06, "ave"=1.93 eV and "sym"=1.94 eV. The spectra are shifted in magnitude for display purposes.

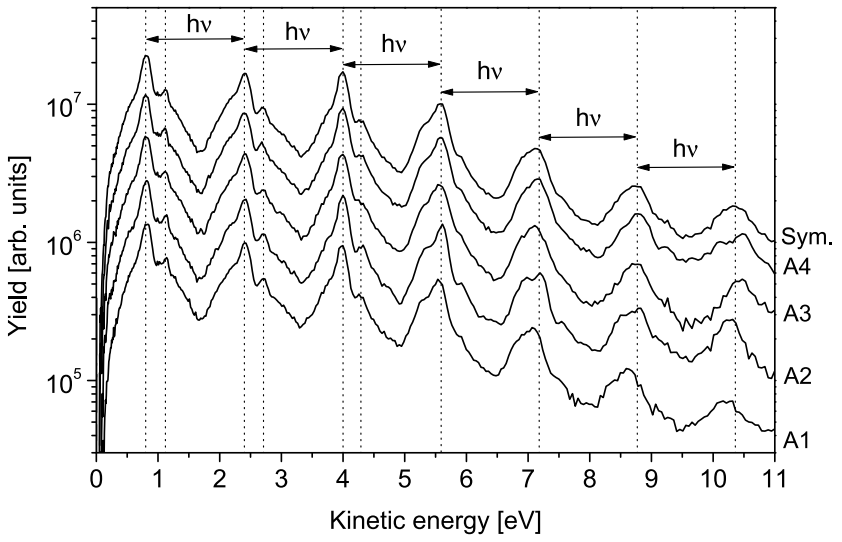

Figure 3.7: Same as in Fig. 3.5 but here for xenon ionized with the 775 nm 150 fs-laser. Dashed lines guide the eye for the overlap of the ATI-peaks, separated by the photon energy 1.60 eV. The spectra are shifted in magnitude for display purposes.

Extraction fields

The condition for momentum mapping corresponds to the best possible resolution of the image of projected photoelectrons. This is found visually by looking at the ATI-rings of xenon photoelectrons. The HV2-electrode is set to a fixed value and the HV1-electrode is scanned until the optimum ratio is found. Typically, -2300 V is applied to HV2 and the range for HV1 where the optimum momentum mapping is obtained is -1520±20 V. The exact number changes from time to time due to laser beam realignment. The typical ratio, HV2/HV1, for best resolution is close to 1.5 regardless of the absolute voltage applied to the electrodes.

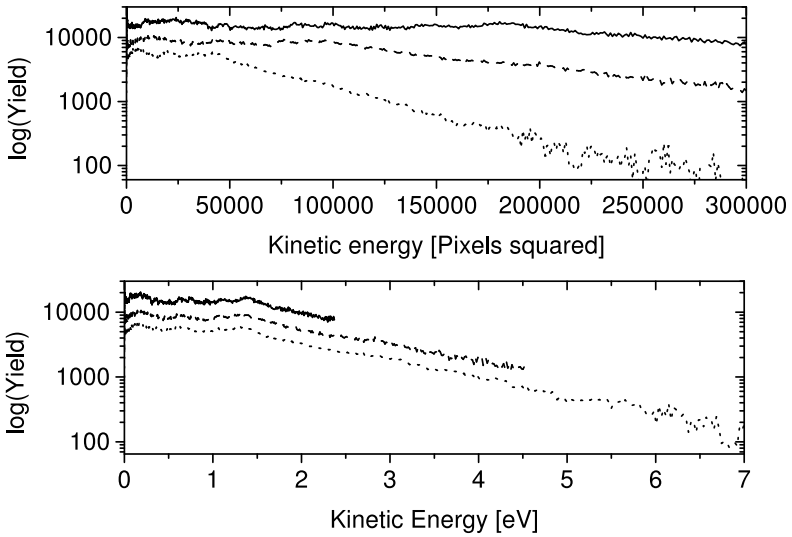

Figure 3.8: Electron spectrum of C_{60} ionized by the fs-laser, 775 nm, 150 fs, at different projection field strengths, HV2/HV1. Solid line: -500 V/-331 V. Dashed line: -1000 V/-661 V. Dotted line: -2300 V/-1520 V. The spectra are shifted in magnitude for display purposes.

Fig. 3.8 shows the photoelectron spectra of fs-laser ionized C_{60} for three different extraction fields with the same ratio, HV2/HV1. The spectra cover the same area of the detector but not the same range of kinetic energies. This is seen in the top frame where the energy scale is in camera pixel units. Bottom figure shows the energy calibrated spectra. The three different projection fields give very similar spectra up to 2.3 and 4.5 eV. Hence the magnitude of the projection field does not affect the electron distributions significantly.

Further, if the detection efficiency differences for the for quadrants A1-A4, discussed above, were essential it would show up in Fig. 3.8.

3.3 Lasers

Three different lasers have been used in this work. The measurements on multi-photon ns-laser ionization of fullerenes and PAH-molecules involved a commercial N_2-laser (Laser Science Inc. VSL337ND-S). The photon energy is 3.68 eV and the pulse duration is specified to be shorter than 4 ns. Typical repetition rates used are 20-40 Hz.

For one photon excitation of clusters of fullerenes (chapter 7) a commercial (Neweks Ltd. PSX-100) excimer laser was used. A fluoride (F_2) gas mixture laser medium gives an output photon energy of 7.9 eV. The pulse duration is specified to 5 ns and the average pulse energy is 10 mJ. Typical repetition rates used are 10-30 Hz.

3.3.1 The femtosecond laser system

The laser used for most of the studies is a commercial (Clark-MXR CPA-2001) Titanium:Sapphire femtosecond laser. The fundamental wavelength is 775±5 nm (1.60 eV) in air, measured with a CCD Spectrometer from "Angewandte Physik und Elektronik GmbH". 388 nm light was generated with a BBO crystal in a doubling unit from Clark-MXR.

The laser beam shape is close to Gaussian and sech^2 [73]. The maximum output power is up to 900 mW at a repetition rate of 1 kHz. The pulse duration was measured by an autocorrelator (APE Pulse Check), in noncollinear mode. The full width at half maximum (FWHM), τ_{AC} of the autocorrelation trace was measured to 230 fs for the fundamental wavelength. The actual pulse duration at FWHM, τ_p, of the intensity profile is related to the autocorrelation function as τ_{AC}/τ_p=R, where R is a reduction factor. The scientific community has agreed to use the reduction factor for a sech^2 pulse regardless of what the actual pulse shape is [73, 74]. The reduction factor for a sech^2 pulse is 1.54, which gives a τ_p=150 fs. For a Gaussian pulse R=1.41. The pulse duration of the 388 nm light is not known but is assumed to be the same as for the 775 nm light, 150 fs. On its way to the interaction chamber

the laser beam travels 25 m and passes a set of optical components which can cause a slight pulse stretching. Attempts were made to position the autocorrelator after the interaction chamber but due to vibrations in the house and the long distance from the laser, causing the laser beam to wiggle in space, it was not possible to measure the pulse duration at this position. Longer pulse durations are achieved by detuning the compressor stage after amplification.

To attenuate the laser beam the combination of a $\lambda/2$-waveplate and a Glan laser calcite polarizer, beamsplitters and neutral density filters were used. The calcite polarizer also serves to control the laser polarization which has to be parallel to the PSD-detector in the photoelectron measurements. The laser beam was focused into the chamber by a lens of 30 cm focal distance.

3.3.2 Femtosecond laser beam characteristics

The peak intensity, I_0, of the focused laser beam has been calibrated by xenon ion yield measurements and compared to the measurement by Larochelle *et al.* [12] where the ion yield is plotted versus laser peak intensity for a 800 nm, 200 fs, pulse. In this way a conversion factor from the pulse energy, E_p, which is measured by a powermeter (Coherent Field Master), right after the interaction area, to an absolute intensity scale is obtained. The conversion factor is $4.44\times10^{11}\frac{\mathrm{W/cm^2}}{\mu\mathrm{J}}$.

From the definition of the peak power,

$$P_0 = C \cdot \frac{E_p}{\tau_p}, \tag{3.1}$$

where C is a constant equal to 0.88 for a sech^2 pulse and 0.94 for a Gaussian pulse, and from the measured peak intensity the beam waist, w, can be estimated from

$$I_0 = \frac{P_0}{\pi w^2}. \tag{3.2}$$

The beam waist corresponds to the distance from the center of the pulse to where the intensity is reduced to a factor $1/e$. Assuming a sech^2 shaped pulse $w = 20.5$ μm and for a Gaussian shaped pulse $w = 21.2$ μm. These numbers can be compared to those reported from direct measurements of the beam waist for similar lenses (30 cm) and 795/800 nm laser pulses. In [30] the beam diameter at FWHM was 30 ± 7 μm and in [35] the beam waist was measured to 25μm.

From the pulse energy and beam waist the laser fluence is calculated as

$$F_p = \frac{E_p}{\pi w^2}. \tag{3.3}$$

For all data where the laser fluence is presented, a beam waist of 21.2 μm is used for the 775 nm beam. For the second harmonic the beam waist is assumed to be half this value according to the following relation,

$$w = \frac{f\lambda}{w_0\pi}, \tag{3.4}$$

where λ is the wavelength, f the focal length and w_0 the waist of the non-focused beam.

3.4 The cold source

Chapter 7 concerns laser ionization of clusters of fullerenes. One way of producing clusters of fullerenes is to use a gas aggregation source which in this text is referred to as the "cold source". A schematic representation of the Göteborg cold source is found in Fig. 3.9. The cold source was connected to the interaction chamber in line with the time of flight mass spectrometer. Nowadays the electron spectrometer is found in the same position (Fig. 3.1). The operational principle is as follows: Fullerene powder is heated up to about 500° C creating a vapour of fullerenes which rises into a cold carrier gas, typically helium or argon. The carrier gas is cooled down by collisions with the chamber walls which are at liquid nitrogen temperature, 77 K. The vapour is quenched in the cold carrier gas and if the fullerene density is high enough the molecules will condense and form clusters where the intermolecular bonds are of van der Waals type [75]. The vapour then expands, supersonically, through a conical nozzle of 2 mm diameter with a measured temperature of 110 K. Following the clusters down-stream they leave the cold source through a skimmer of 3 mm diameter and pass a differential pumping stage before they enter the interaction chamber. The characteristics of a cluster source and the cluster sizes it produces is in general very dependent on nozzle and skimmer geometries, background pressure, carrier gas etc. The most critical parameter for this particular source is the carrier gas pressure, see Fig.1 in Paper IV.

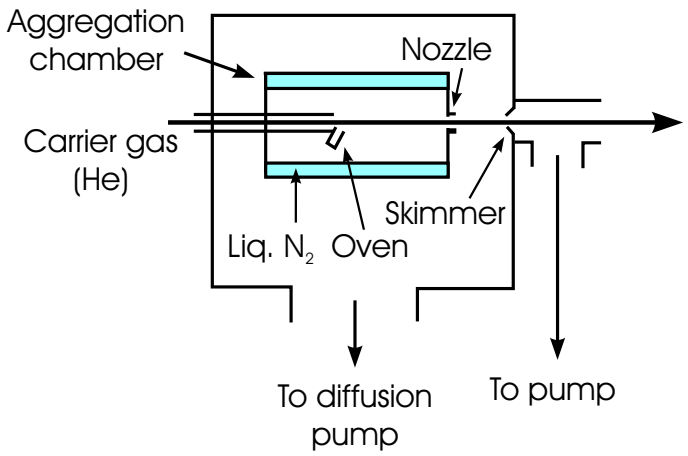

Figure 3.9: The cold source used for production of clusters of fullerenes. Figure from [66].

Chapter 4

Fullerenes - C_{60} & C_{70}

This chapter is about fs-laser ionization of the fullerenes C_{60} and C_{70}. Femtosecond ionization of C_{60} has been extensively studied before and it therefore serves as a good choice of reference for new measurements on other molecules and also as an additional test of the new electron spectrometer. The transient hot electron ionization mechanism of large molecules is the main theme in this thesis and it has been suggested for C_{60} [42], discussed in the background chapter. The main goal is to establish whether it is unique or not for C_{60}. The natural way to start measurements was therefore to repeat the earlier results on C_{60} and from there proceed to a similar molecule, C_{70}. The chapter is based on Paper I with some additional results.

4.1 Mass spectrometry results

The mass spectra for C_{60} after 775 nm, 150 fs laser ionization are shown in Fig. 4.1 for increasing laser intensities from **a** to **f**. For the lowest intensity, Fig. 4.1**a**, only the singly charged C_{60} molecule and the first two fragments C_{58}^+ and C_{56}^+ are observed. For this relatively low laser fluence the excited C_{60} molecule decays mainly via these two channels, ionization and C_2-fragmentation (radiative cooling is negligible here [76]). The ionization potential is 7.64 eV [77] and the C_2 evaporative (fragmentation) energy is ca. 11 eV [50, 52, 78, 79] for C_{60}. Proceeding to higher laser intensities, Fig. 4.1**b** and especially in Fig. 4.1**c**, doubly charged C_{60} and fragment ions are observed. At these laser intensities the absorption of photons is fast enough for a second ionization step before the excitation energy is quenched into the

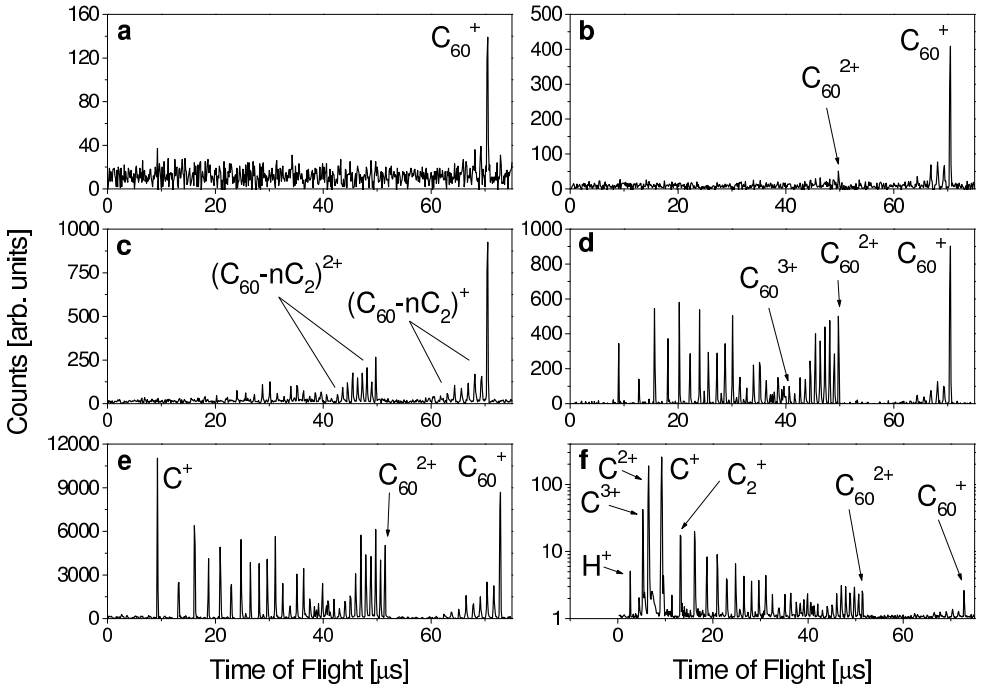

Figure 4.1: Time of flight mass spectra of C_{60} ionized with 150 fs, 775 nm laser pulses at different laser peak intensities. From **a** to **f**: 0.40, 0.49, 0.73, 1.11, 2.22 and 7.01×10^{13} W/cm^2. Notice that the spectra in **e** & **f** are recorded with a different acceleration potential, leading to longer flight times. **f** is plotted in semilogarithmic scale for display purposes.

vibrational system. At even higher intensities, Fig. 4.1**d**, **e** and **f**, a possible triply charged ion is observed. It is however not possible to distinguish a C_{60}^{3+} ion from lighter fragments of lower charge. The main observation at the highest intensities is however the onset of a heavy fragmentation all the way down to C^+ and for the highest intensity in Fig. 4.1**f** even doubly and triply charged carbon atoms are observed.

The mass spectra for fs-laser excitation can, in an instructive way, be compared to the ns-laser spectrum shown in Fig. 4.2 where a strong fragmentation is observed, similar to Fig. 4.1**e**, but where doubly charged ions are absent. The absorption of photons is now too slow for double ionization and a highly excited vibrational system is therefore built up leading to strong fragmentation during the laser pulse duration. The tail, on the high mass side, of C_{60}^+ is due to delayed ionization [46] and is a fingerprint of thermionic emission.

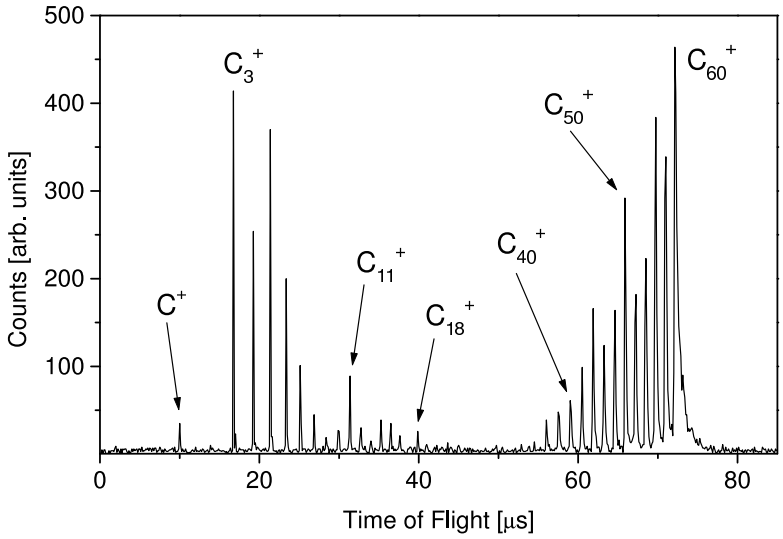

Figure 4.2: Time of flight mass spectrum of ns-laser ionized C_{60}.

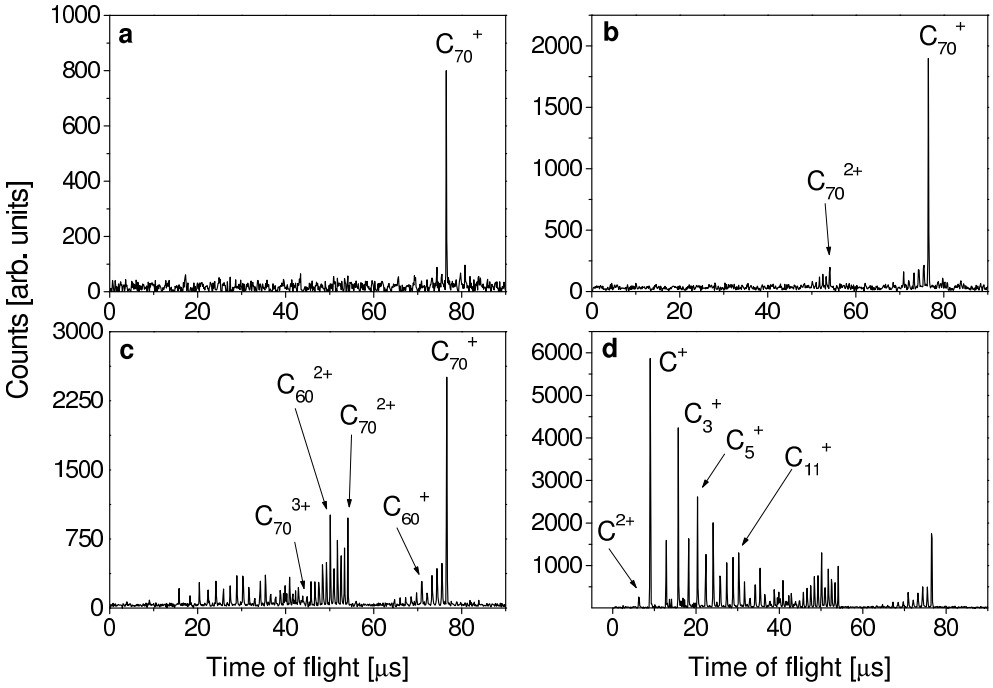

Figure 4.3: Time of flight mass spectra of C_{70} ionized with 150 fs, 775 nm laser pulses at different laser peak intensities. From **a** to **d**: 0.44, 0.62, 1.11 and 2.17 $\times 10^{13}$ W/cm^2.

Both the fs- and ns-mass spectra are in agreement with the previously published mass spectra of C_{60} after fs-laser and 'long' pulse (>ps) excitation [34] and can be understood in relation to the discussion of thermal ionization in the background chapter.

The fs-laser excitation mass spectra of C_{70} for similar laser intensities as for C_{60} are shown in Fig. 4.3. The spectra are very similar to those of C_{60}. This is expected since the two molecules are very similar in most respects. The interpretations of the C_{70} spectra are therefore the same as for C_{60}.

In Fig. 4.4 the mass spectra corresponding to pulse durations from 150 fs up to 1.95 ps at fixed fluence 2.27 J/cm^2 are shown. The important change in going to longer durations is that the doubly charged fragments decrease in abundance relative to the singly charged ions and at 3 ps pulse duration they vanish. Also this finding is similar to what was observed in the mass spectra of C_{60} in [34] where no doubly charged ions were present at 5 ps pulse duration.

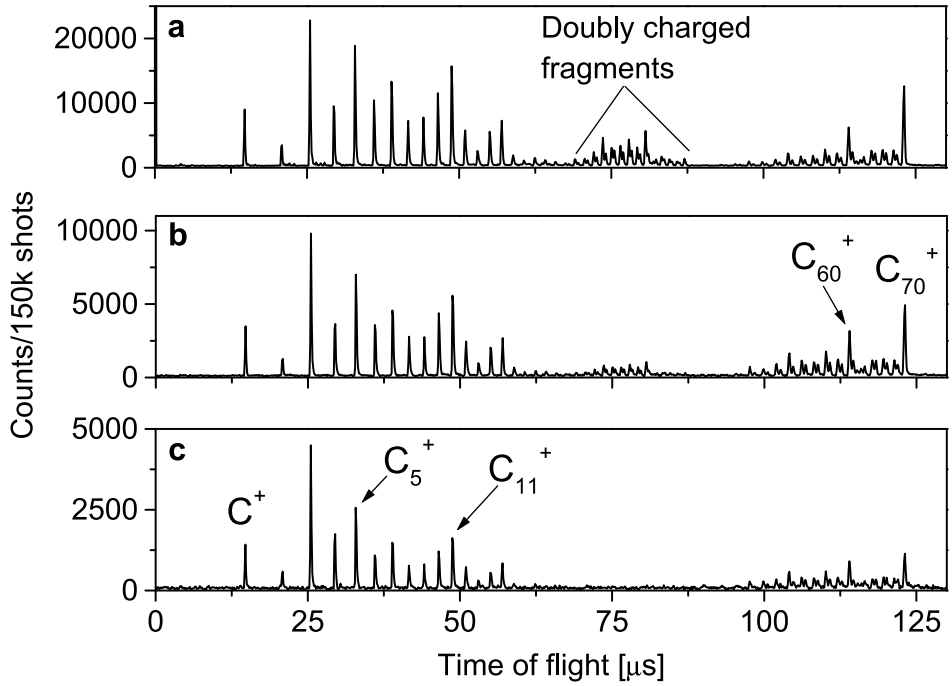

Figure 4.4: Time of flight mass spectra of C_{70} ionized with 775 nm laser pulses at fixed fluence but varying pulse durations. **a**: 150 fs, **b**: 560 fs and **c**: 1.95 ps. The spectra are recorded with the reflectron detuned and the double peak structure appearing at for example the C_{60}^+ peak is due to metastable fragmentation [80].

4.2 Electron spectroscopy

The photoelectron spectra of C_{60} and C_{70} ionized with the fs-laser at 775 nm are extensively discussed in Paper I. Below follows a summary of the findings and conclusions drawn from there with some additional remarks. Spectra of C_{70} recorded at higher laser intensities than reported in Paper I are also included.

The same photoelectron spectra of C_{70} as in Fig. 7 of Paper I are shown with the addition of spectra for higher fluences in Fig. 4.5. For C_{60} spectra, see Fig. 6 of Paper I. The experiments were performed with laser pulse inten-

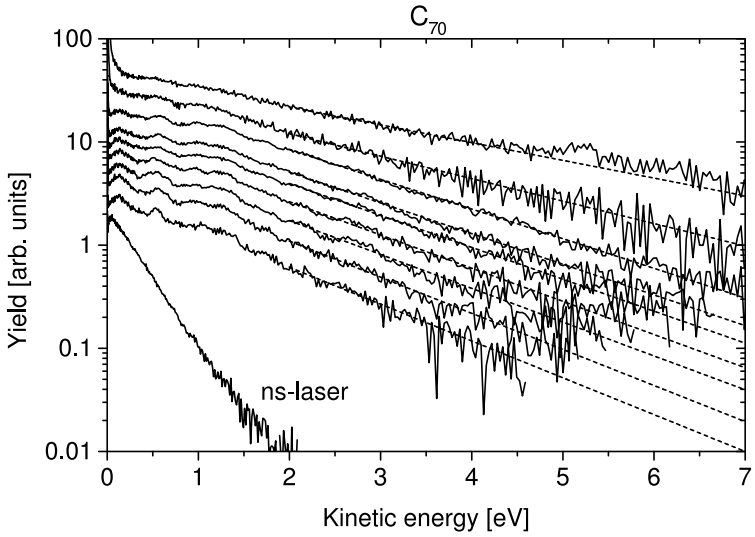

Figure 4.5: Photoelectron spectra of C_{70} ionized with 150 fs, 775 nm, pulses. The fluences and peak intensities are from top to bottom: 3.54 (2.22), 2.69 (1.69), 2.19 (1.38), 1.84 (1.15), 1.70 (1.07), 1.56 (0.98), 1.42 (0.89), 1.27 (0.80) and 1.13 J/cm^2 (0.71×10^{13} W/cm^2). Thermal fits are plotted as dotted lines and the temperatures are presented in Fig. 4.7. The ns-spectrum is included as a reference to thermionic emission and corresponds to an electronic temperature of 0.33 eV.

sities that correspond to the multi-photon ionization regime. The Keldysh parameter, γ, calculated for the laser peak intensity ranges between 1.7 and 3 for the spectra in Fig. 4.7. Recall that the photoelectron spectra of rare gas atoms, ionized at laser intensities corresponding to $\gamma > 1$, are dominated by ATI-peaks. The PES of the fullerenes are however dominated by a smooth distribution of exponential form at energies outside the photon energy 1.6 eV. The same observation was made for similar laser parameters in [34, 35] and

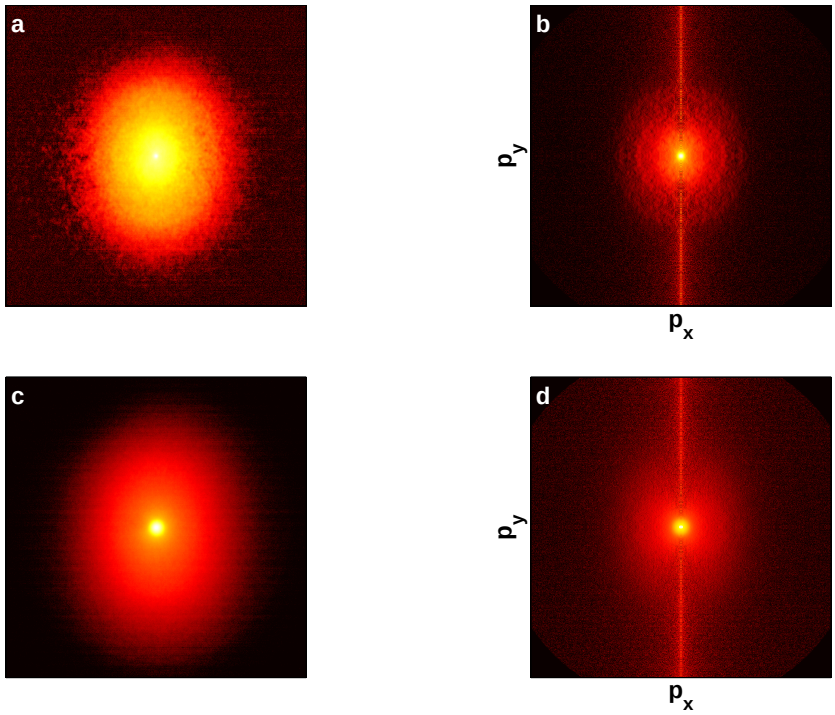

Figure 4.6: Momentum maps of C_{70} after fs-laser ionization. **a**: raw image, **b**: inverted image, at laser peak intensity 7.10×10^{12}W/cm^2 (1.13 J/cm^2). **c**: raw image, **d**: inverted image, at laser peak intensity 2.22×10^{13}W/cm^2 (3.54 J/cm^2). The central rings, vaguely seen in **b**, are associated with resonance enhanced ionization from Rydberg states [66, 81].

as discussed in section 2.2.1 the ionization process is interpreted as *transient hot electron emission*.

Momentum maps for the highest and lowest fluences are shown in Fig. 4.6. In contrast to the momentum map for ns-laser excitation in Fig 3.4**a**, which is isotropic, these clearly show a prolongation along the laser polarization axis. This subject will be further discussed in chapter 6 and for the moment we note that it affects the slope of the photoelectron distributions but not the interpretation of the data.

The observed apparent electronic temperatures after fs-excitation are extremely high, from 10000 K and higher, showing a linear increase with laser fluence, see Fig. 4.7. Such extreme temperatures can only be observed if the heating of the electronic system is very rapid so that the excitation energy does not have time to dissipate into the vibrational modes which cools off the

electronic system. As mentioned in section 2.2.1 the time window for this process is approximately 100 fs to a few ps for C_{60}. Hot electron emission is therefore never observed for ns-ionization. The strong fluence dependence on the electron temperature is due to the low heat capacity of electrons which is yet another difference compared to the ns-case where excitation energy is stored in both electronic and vibrational degrees of freedom.

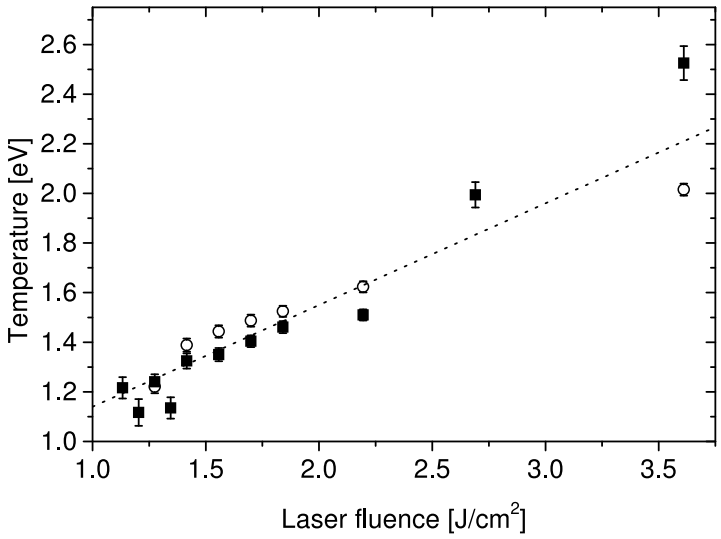

Figure 4.7: The electronic temperatures of C_{60} (circles) and C_{70} (squares). The dotted line is a linear fit to the electronic temperatures of C_{60} measured in [35] where the laser wavelength and pulse duration were 780 nm and 180 fs respectively.

The apparent suppression of the fullerene electron spectra at low kinetic energies, inside ca. 2 eV, raises the question of detector saturation. According to Fig. 3.8 a strong detector saturation can however not be observed, since the magnitude of saturation would be different for different extraction fields. Other possible explanations are peak suppression due to the ponderomotive energy [18], discussed in chapter 2 and secondly, the approximation of the thermal distribution as a simple exponential function is only a first order approximation which is most accurate for high photoelectron energies.

Attempts have been made to extract the lifetime of the hot electron system in C_{70} by observing the drop in temperature with increased pulse duration and in ion pump-probe measurements. For a fixed laser fluence we expect the electronic temperature to decrease with longer pulse duration due to electron-phonon coupling, which is also what is seen in Fig. 10 of Paper I.

However, there is a second factor contributing to this drop and that is the possibility of electron emission before the excitation energy peaks or equivalently before the laser pulse intensity peaks and these two effects could not be disentangled. From the electron spectra in Fig. 4.5 it is clear that there is not only "hot electrons" that build the spectrum but also Rydberg resonances are clearly seen at low energies. Hence, ion yield pump-probe data gives only the combined lifetime of the whole excited system and is only good to show that there is "something" with a lifetime in the molecule.

The measurements at varying pulse duration could however be used in another way. As discussed in the Background chapter the relevance of the standard Keldysh parameter, γ, is questionable when it is applied to molecules. Some publications point to a transition from MPI to field ionization at lower laser intensities for molecules while others argue for the opposite. To exclude field ionization as the dominant mechanism causing the smooth electron distributions observed for the fullerene spectra, not relying on the value of γ, the electronic temperatures for the short, 150 fs pulses, and the stretched pulses were compared. This is shown Fig. 4.8. The plot shows that the electronic temperature, or shape/slope of the spectra, corresponding to two

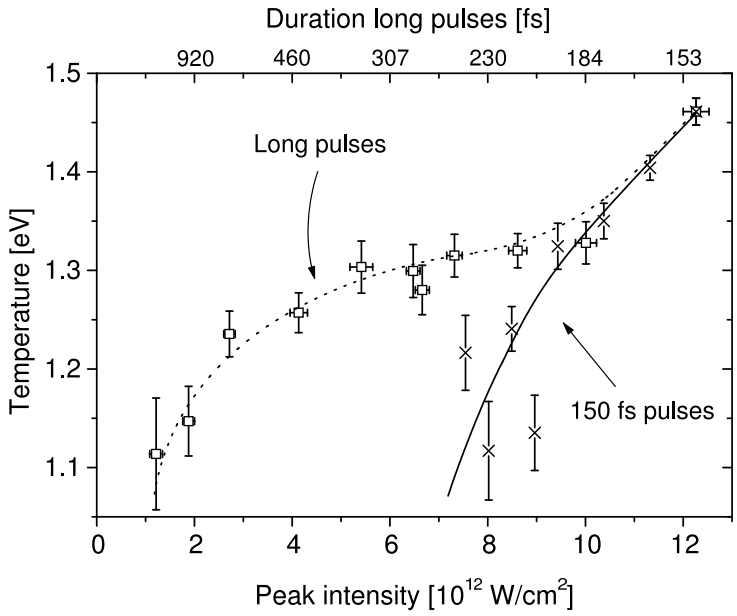

Figure 4.8: The electronic temperatures of C_{70} for 150 fs pulses at varying fluence (crosses) and pulses of fluence 1.84 J/cm^2 at varying pulse duration (open squares). Solid and dotted lines guide the eye.

different laser peak intensities can be identical as long as the low intensity pulse has a higher fluence. Similar electronic temperatures are observed for laser intensities that differ by as much as a factor of 4. This is inconsistent with a field ionization scenario where the laser intensity is the most important parameter for the shape of the photoelectron spectrum but consistent with a thermal ionization mechanism where a higher laser fluence leads to a stronger heating of the electronic system.

4.3 Conclusions

Both the mass- and photoelectron spectra of C_{60} are in good agreement with previously published data, both for ns- and fs-laser excitation [34, 35, 53]. The fs-laser ionization spectra of C_{70} are very similar to those of C_{60} as expected. The apparent electron temperatures are both fluence and laser intensity dependent, which is consistent with a thermal ionization process but not with field ionization. It is therefore concluded that electron emission from C_{70}, like for C_{60}, is thermal; Electrons are emitted from a highly excited electron system where vibrations are still cold.

Chapter 5

Polyaromatic hydrocarbons

In this chapter the results on polyaromatic hydrocarbons (PAH) are presented and discussed. The main motivation for these experiments is to investigate whether the transient hot electron excitation/ionization mechanism is unique for the fullerenes C_{60} and C_{70} or if it is a more general ionization mechanism for large molecules after fs-laser radiation and, if so, for how small molecular systems is it present? The molecules studied are coronene ($C_{24}H_{12}$), benzo[GHI]perylene ($C_{22}H_{12}$) and anthracene ($C_{14}H_{10}$). These are planar molecules consisting of a number of benzene-rings terminated with hydrogen atoms. Coronene consists of seven rings, one central ring surrounded by six outer rings. Benzo[GHI]perylene has the same form as coronene but with two of the outer carbon atoms removed. Anthracene consists of three benzene-rings in a row. The ionization potentials are for coronene 7.39 eV [82], benzo[GHI]perylene 7.19 $\pm$ 0.1 [83] and anthracene 7.439 $\pm$ 0.006 eV [84]. The chapter is based on Paper II.

5.1 Mass spectrometry

Mass spectrometry of PAH-molecules after fs-laser excitation has been extensively studied before [25–27, 85, 86] and the results presented here mainly serve as a reference to the photoelectron spectra and for comparison to the fullerene mass spectra.

Coronene

Mass spectra of coronene after irradiation with 775 nm, 150 fs pulses at different laser intensities are shown in Fig. 5.1. For the lowest intensity in Fig. 5.1**a**, only the singly charged mother ion (M^+) is observed. At slightly higher intensity, Fig. 5.1**b**, the onset of fragmentation sets in and also the doubly charged mother ion appears. At even higher intensities, Fig. 5.1**c** and **d**, the doubly charged ion starts to fragment as well and for the highest applied laser fields singly charged carbon and hydrogen atoms and small molecular ions dominate the spectrum, Fig. 5.1**e** and **f**. This is a similar development of the mass spectra for increased laser intensity as was observed for anthracene after 800 nm, 130 fs laser excitation [27].

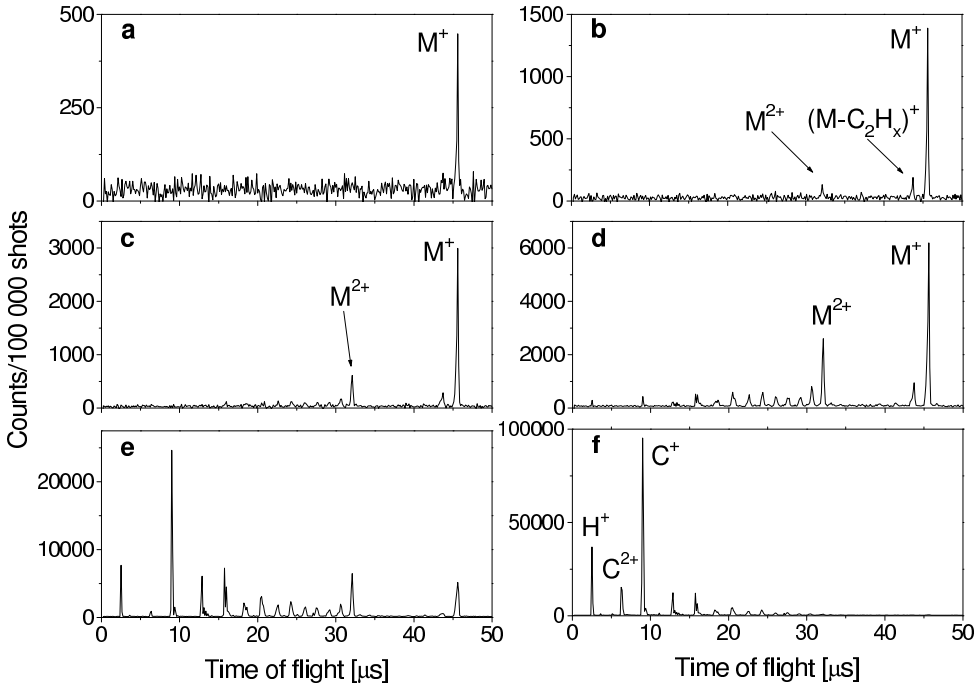

Figure 5.1: Mass spectrum of coronene after 775 nm 150-fs laser ionization. From **a** to **f** the laser peak intensities are: 3.33, 4.88, 7.55, 11.1, 27,8 and 62.8×10^{12} W/cm^2. Recorded in linear ToF-mode.

The fragmentation goes through many different channels. This is most easily seen in Fig. 5.2 which shows a spectrum with a higher resolution. The mother ion fragments mainly via H_2 losses, which is seen as a splitting of the mother

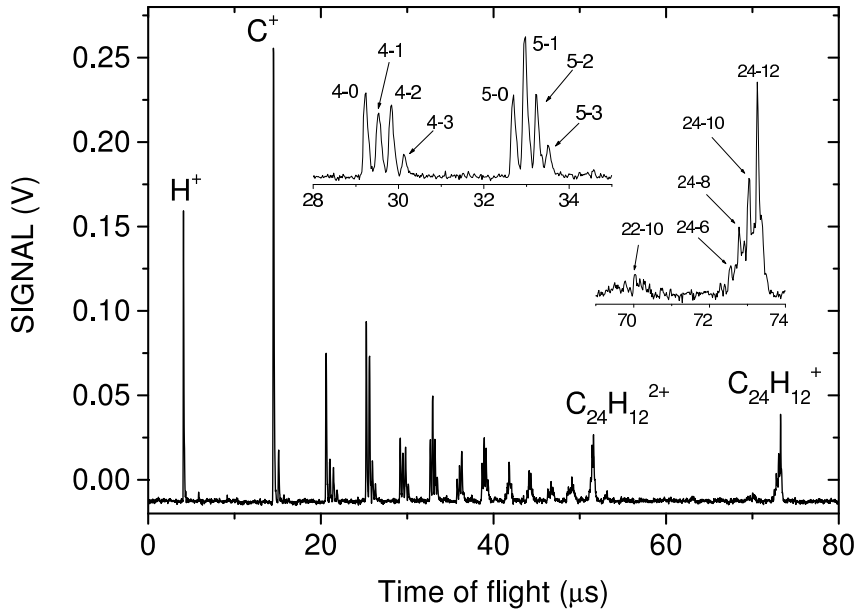

Figure 5.2: Mass spectrum of coronene after 775 nm 150-fs laser ionization. Laser peak intensity 2.06×10^{13} W/cm^2. Recorded in linear mode with oscilloscope.

ion into sub-peaks or it fragments via C_2H_x, where x is mostly even numbered for the largest fragments. The fragment groups seen below the doubly charged mother ion correspond to small C_yH_x-ions. At least for the smallest fragments, the left-most peak within the group of fragments corresponds to the naked C_y ion, and from there single hydrogen atoms are added. Looking at, for example the C_4H_x group (inset in Fig. 5.2), the main sub-peaks correspond to singly charged C_4, C_4H, C_4H_2 and C_4H_3. If there were also doubly charged fragments of twice the mass there should be additional peaks between those, looking like singly charged 4-0.5, 4-1.5 and 4-2.5 masses. Such peaks are absent and hence there are no small doubly charged fragments, with an odd number of hydrogens, in the spectrum. The same argument goes for odd numbered carbon atoms. For the larger fragments, just below M^{2+} this kind of analysis is not possible since the sub-peaks are not resolved. Reports on ionization of anthracene and smaller PAH-molecules with sub-100 fs pulses do however show doubly charged fragments for the first fragmentation steps [26, 86]. The above discussion holds for the benzo[GHI]perylene and anthracene mass spectra too which are presented below.

There are differences but also similarities to the fullerene mass spectra. It appears as if there is, as for fullerenes, a competition between fragmentation and

a second ionization step of the singly charged mother ion. Once the mother ion reaches the doubly charged state it is unlikely that it will ionize again, due to the high ionization potential of the third charge state. Hence, the highly excited M^{2+} ion relaxes through fragmentation and a strong fragmentation tail is observed below the M^{2+} ion, as is also the case for the fullerenes. But according to discussion above it seems, unlike for the fullerenes where the fragments just below M^{2+} are doubly charged, that the small fragments below the coronene M^{2+} have a large contribution of singly charged fragments, which indicates that some doubly charged fragments fission.

Benzo[GHI]Perylene

The mass spectra corresponding to 775 nm, 150 fs ionization are shown in Fig. 5.3. The spectra are very similar to those of coronene so for a discussion see the coronene section above.

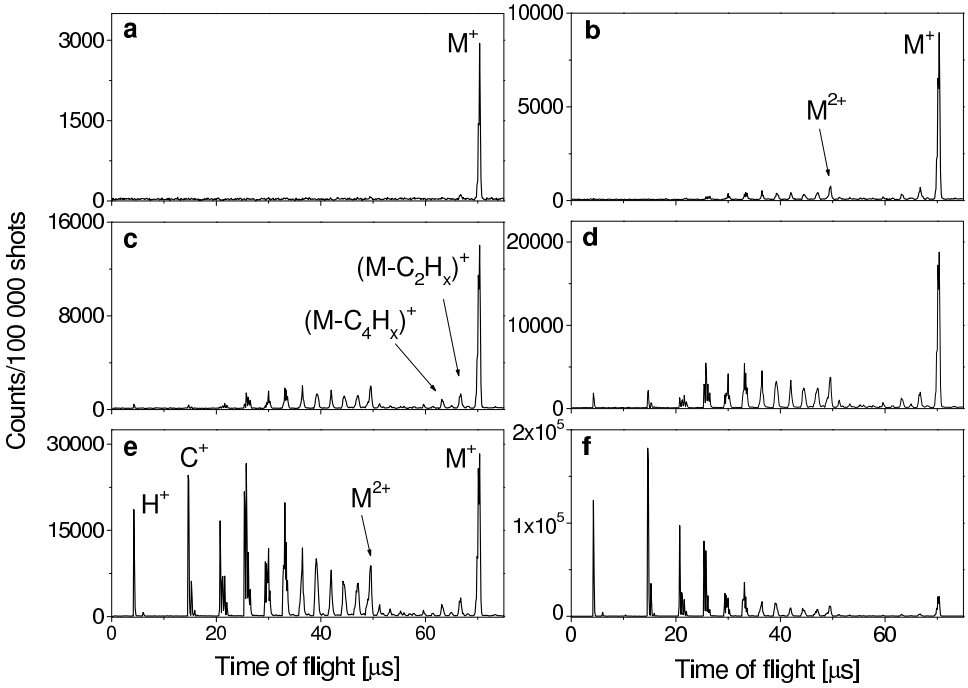

Figure 5.3: Mass spectra of benzo[GHI]perylene after 775 nm 150 fs laser ionization at different laser peak intensities from **a** to **f**: 2.66, 4.44, 6.22, 7.99, 13.1 and 20.9×10^{12} W/cm^2. Recorded in reflectron mode.

The effect of using a longer pulse duration (1100 fs) on the fragmentation pattern is shown in Fig. 5.4. The main difference compared to the short

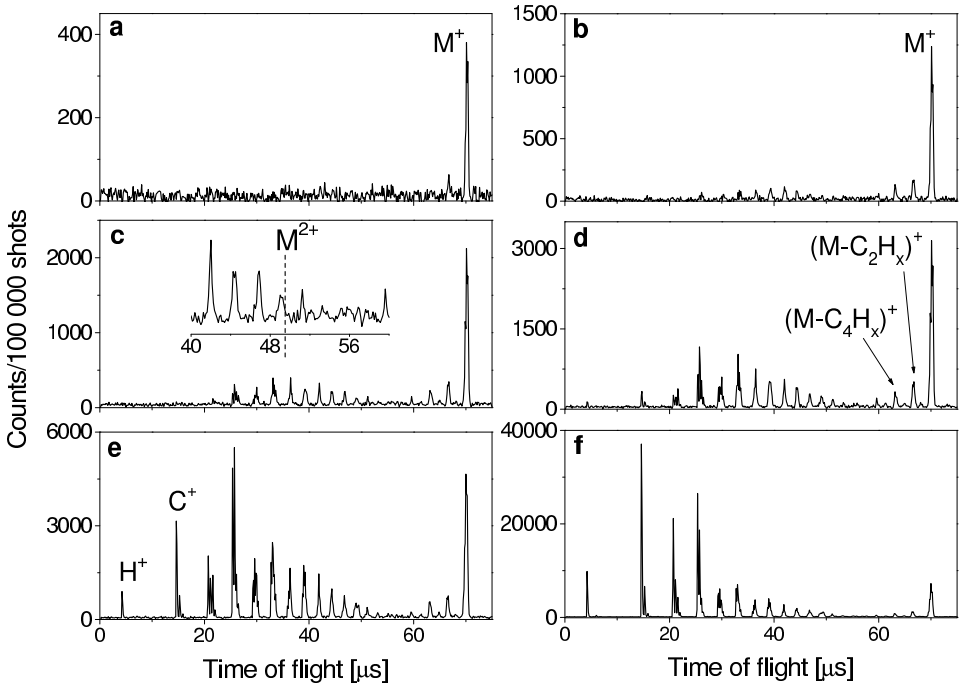

Figure 5.4: Mass spectra of benzo[GHI]perylene after 775 nm 1100 fs laser ionization at the same laser fluences as in Fig. 5.3. Recorded in reflectron mode.

pulse duration in Fig. 5.3 is that the doubly charged mother ion M^{2+} is absent at all laser intensities for the long pulse. As shown in the inset of Fig 5.4**c** the position of the M^{2+} ion does not coincide with a strong peak as it does for the 150 fs ionization case. The peak just to the left of the dotted line in Fig. 5.4**c** corresponds to the position of the shoulder seen on the left side of the M^{2+} peak in Fig. 5.3**e**. This trend of a lower doubly charged ion yield and a lower yield of the small ions C^+ and H^+, by applying longer laser pulses, is the same as was observed for the fullerenes, see chapter 4.

The only experiments performed with the second harmonic, 388 nm, of the fs-laser were on benzo[GHI]perylene and in Fig. 5.5 the mass spectra at varying intensities are shown. The intensities used for the 388 nm pulses are ca. one order of magnitude lower than those of the 775 nm pulses. The spectra are very similar compared to the ones for 775 nm ionization in Fig. 5.3 both in shape and how the spectra develop with increased laser intensity. The clearest difference is that, at least in Fig. 5.5**e** and **f**, the M^{2+} ion is

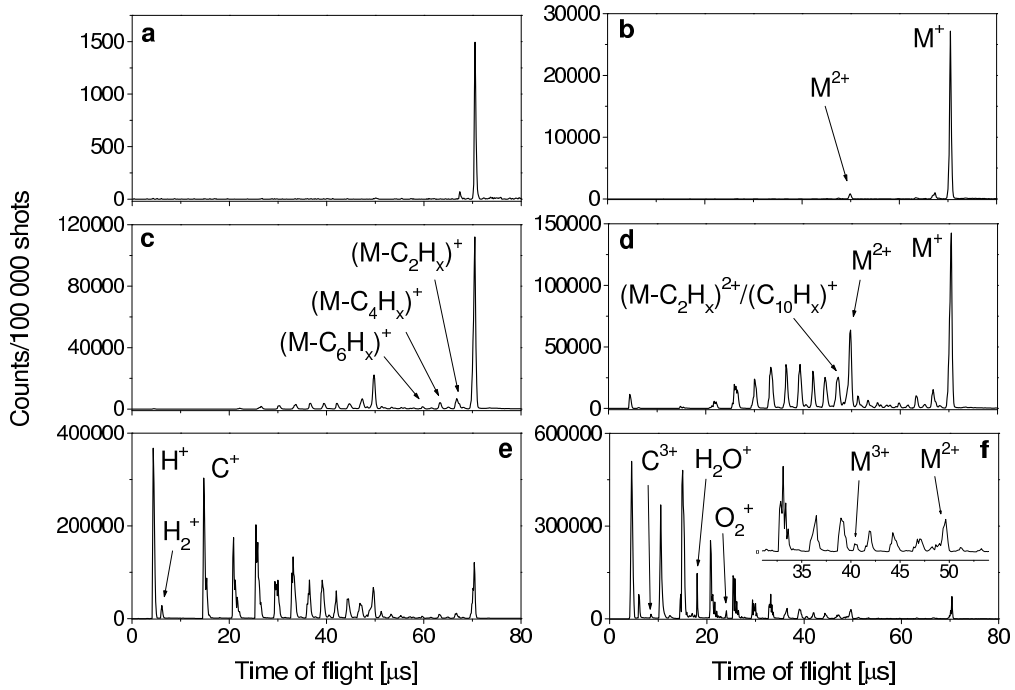

Figure 5.5: Mass spectra of benzo[GHI]perylene after 388 nm 150 fs laser ionization at different laser intensity from **a** to **f**: 7.55×10^{10}, 1.51×10^{11}, 3.40×10^{11}, 5.52×10^{11}, 1.58×10^{12} and 8.96×10^{12} W/cm^2. Recorded in reflectron mode.

stronger in relation to the lighter fragments compared to what is observed at any intensity in the 775 nm spectra. Further, for the highest intensity, 8.96×10^{12} W/cm^2, in Fig. 5.5**h** triply charged carbon appears and the rest gas of water and oxygen is ionized.

The fact that the fragmentation spectra are so similar for 388 and 775 nm light suggests that the fragmentation of the ions is to first order driven by the amount of energy that the molecules have absorbed and high electric (laser) field effects are secondary and no major contribution to the fragmentation due to re-colliding electrons can be argued for.

Anthracene

The mass spectra for anthracene, Fig. 5.6, are similar to those of coronene and benzo[GHI]perylene and also to mass spectra of anthracene reported in the literature for similar laser paramters [25]. Differences to coronene

and benzo[GHI]perylene are first of all that anthracene ionizes at lower laser intensity. Considering the low intensity spectra Fig. 5.6**a-d** and the coronene spectra in Fig. 5.1 it is clear that anthracene is already heavily fragmented at an intensity of 3.33×10^{12}W/cm^2 which is close to the appearance threshold for singly charged coronene ions in Fig. 5.1**a**. The explanation for that is not related to the ionization potential since the IP of anthracene, 7.439 ± 0.006 eV, is higher than for both coronene, 7.39 eV and benzo[GHI]perylene, 7.19 ± 0.1. It is however consistent with the results presented in [20–22] that it is easier to ionize smaller molecules with few delocalized electrons and where the explanation lies in the screening effect of those electrons. Secondly, in the coronene and benzo[GHI]perylene spec-

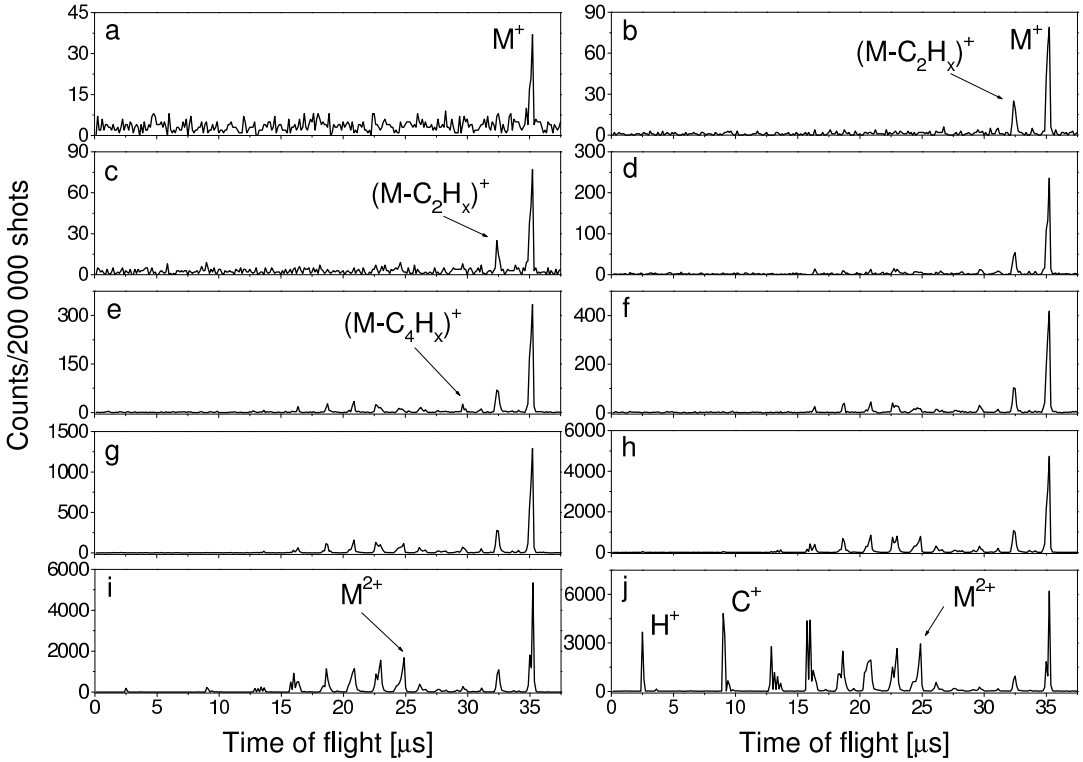

Figure 5.6: Mass spectra of anthracene after 775 nm, 150 fs laser ionization. From **a** to **j** the peak intensities are: 1.33, 1.78, 2.22, 2.66, 3.11, 4.00, 5.33, 7.99, 12.0 and 20.4×10^{12} W/cm^2. Recorded in linear mode.

tra, the M^{2+} ion signal appears before the lighter fragments and it is also more abundant, at least for the low laser intensity spectra in Fig. 5.1**b-d**. For anthracene this is not the case. For the lowest fluences, Fig. 5.6**a-g**, the

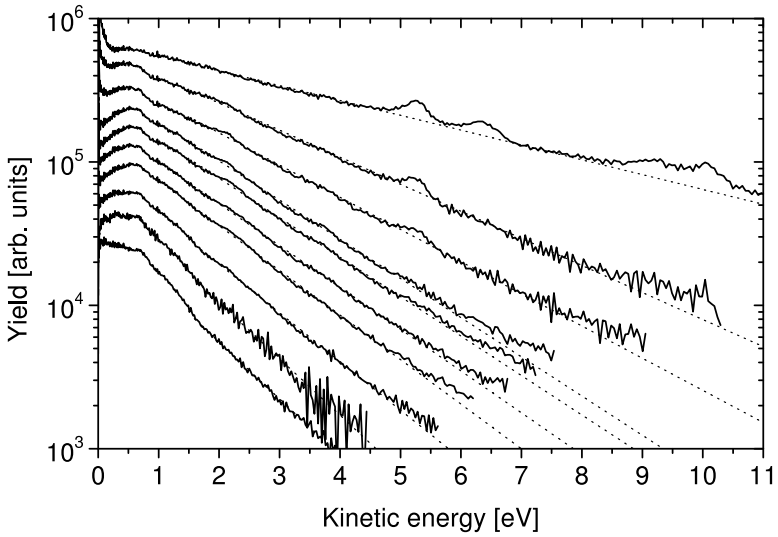

Figure 5.7: Electron spectra of coronene at constant pulse duration 150 fs. Wavelength 775 nm. From bottom to top the laser intensities are: 3.55, 4.88, 6.66, 7.99, 9.32, 10.9, 11.5, 21.1, 27.5 and 61.3×10^{12} W/cm^2. The spectra are shifted vertically for display purposes.

trend is that the mother ion first loses a C_2H_x unit (Fig. 5.6**b**), which is similar to coronene. But then at increasing laser intensity it seems as if a strong fragmentation sets in and that a M^{2+} ion peak is never dominant, in contrast to what is observed for coronene and benzo[GHI]perylene. At the highest laser intensities, Fig. 5.6**h-j**, it seems as if the M^{2+} ion increases in abundance compared to the lighter fragments.

5.2 Electron spectroscopy

5.2.1 Coronene

The electron spectra of coronene, ionized with 775 nm 150 fs light, for the same range of intensities that was used in the mass spectrometry measurements, Fig. 5.1, are shown in Fig. 5.7. with corresponding momentum maps in Fig. 5.8. As for the fullerenes the spectra are dominated by a smooth electron distribution of exponential form for electron kinetic energies greater than the photon energy, at least for the lowest intensities. For the highest intensity two strong pairs of peaks appear at 5.3/6.3 eV and 9.3/10.3 eV,

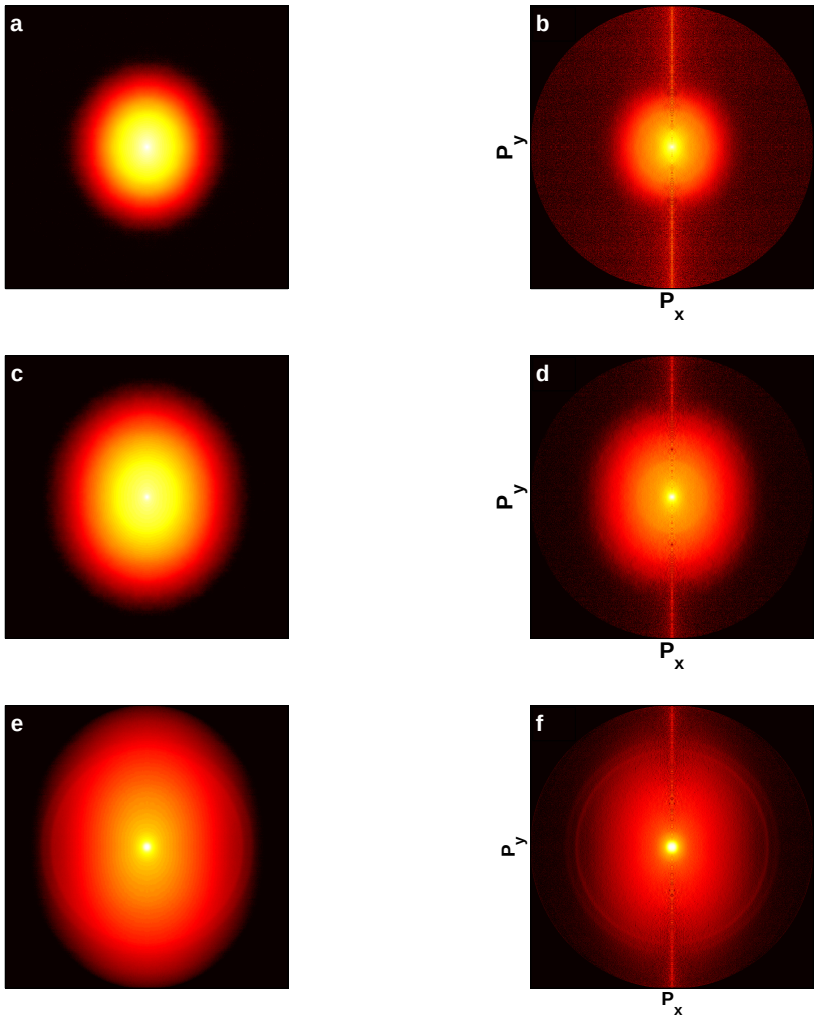

Figure 5.8: Electron momentum maps of coronene after 150 fs, 775 nm ionization. Left column are symmetrized images and right column are the inverted images. Laser peak intensities are for **a** & **b** 0.36, **c** & **d** 1.15 and **e** & **f** 6.13×10^{13}W/cm^2

superimposed on the smooth distribution. These peaks are clearly seen as rings in Fig. 5.8**f** and will be further discussed below. The ATI-series can be seen, weakly, in the 4:th top most spectrum with the first, second and third peak at energies 2.15, 3.74 and 5.33 eV respectively. For the lowest intensities, up to 9.32×10^{12} W/cm^2, the corresponding mass spectra are dominated by the singly charged mother ion and hence the contribution to the electron distribution from small fragments can be disregarded. Further, the Keldysh parameter ranges from 2.75-4.1 for these spectra, which is far from the field

ionization regime. Hence, the similarities to the fullerenes are striking. For laser intensities in the MPI-regime and for single ionization conditions of the coronene molecule, Boltzmann-like electron distributions are observed with no major contribution of ATI-peaks. This observation, together with the similarities between the coronene and fullerenes mass spectra, suggests that the transient hot electron ionization is present also for coronene.

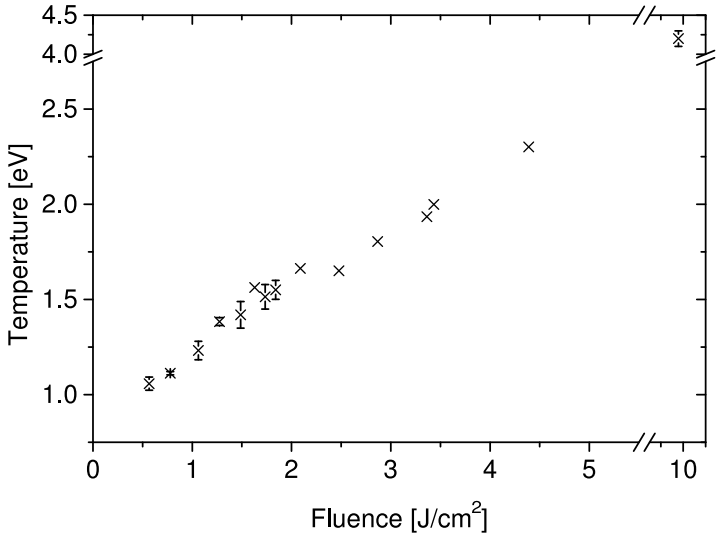

Figure 5.9: Electron temperatures of coronene extracted from the spectra in Fig. 5.7. Error bars are those of the mean value where several data points are available. The point at highest fluence is fitted by hand and the error is estimated.

The electron temperatures extracted from linear fits to the photoelectron distributions are shown in Fig. 5.9. The main observations here are that electron temperatures and the close to linear increase of the temperature with increasing laser fluence is very similar to those of the fullerenes.

For increasing laser intensities, above 9.32×10^{12} W/cm^2 (1.49 J/cm^2), there is in fact nothing in the electron spectra that indicates that the transient hot electron ionization mechanism is no longer present, the smooth electron distribution is still there. But because of the stronger contribution of doubly ionized ions and the heavy fragmentation, seen in Fig. 5.2**d-f**, and the smaller Keldysh parameters, which becomes equal to unity for the highest intensity 6.13×10^{13} W/cm^2, these photoelectron spectra are not easily interpreted.

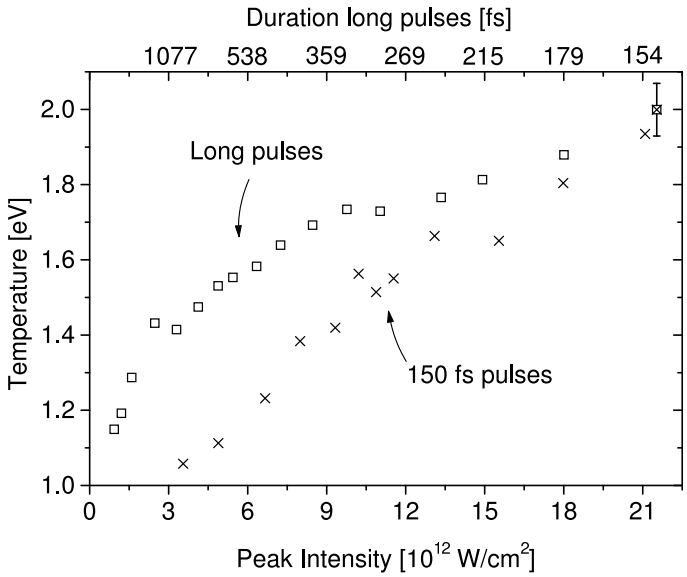

Figure 5.10: Same electron temperatures as in Fig. 5.9 and 5.11 but here as a function of laser peak intensity. Crosses: Varying fluence at 150 fs pulse duration. Open squares: Varying pulse duration at a fixed laser fluence, 3.43 J/cm^2. The error bar represents the largest standard deviation, of the mean value, of those measurements where more than one point for the same laser parameter are available. The error bar represents the reproducibility of the measurements. The errors in the fitting procedure are much smaller.

The same experiment as was performed on C_{70}, Fig. 4.8, to eliminate field ionization as the main active ionization mechanism in the experiments presented in this work, was also done for coronene, Fig. 5.10. Recall, the idea is to measure the electron temperature as a function of laser intensity at different laser fluences and pulse durations. In a pure field ionization process the shape/temperature of the photoelectron distribution should depend only on the laser intensity. In the coronene measurements the laser fluence was chosen to be higher (3.43 J/cm^2) for the stretched pulses compared to what was used in the C_{70} measurements (1.84 J/cm^2). This was to try to get a better separation between the two branches. The result is similar to that observed in the C_{70} measurements. For identical laser peak intensities, the laser pulse with the longest pulse duration (highest fluence), generates the highest electron temperature. For the lowest temperatures observed, around 1.2-1.3 eV, the short, 150 fs pulse, needs to be ca 4 times more intense than the more energetic stretched pulses to give the same electron temperature.

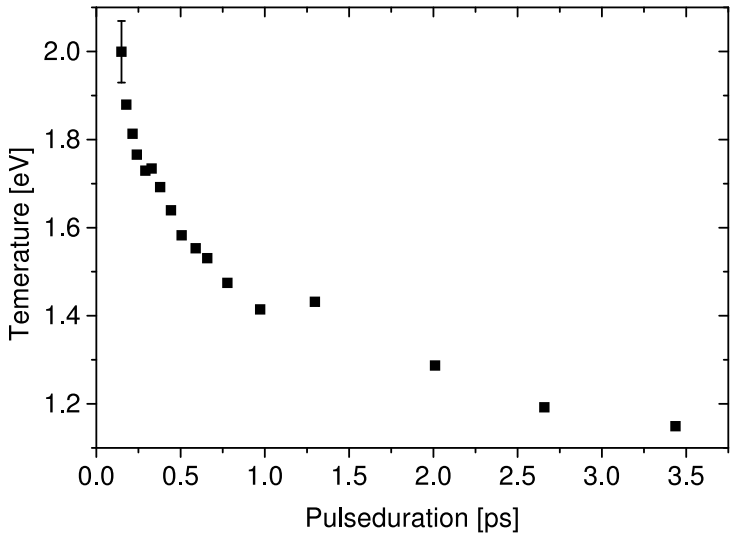

Figure 5.11: Electron temperatures of coronene extracted from the spectra in Fig. 5.12. Same error bar as in Fig 5.10.

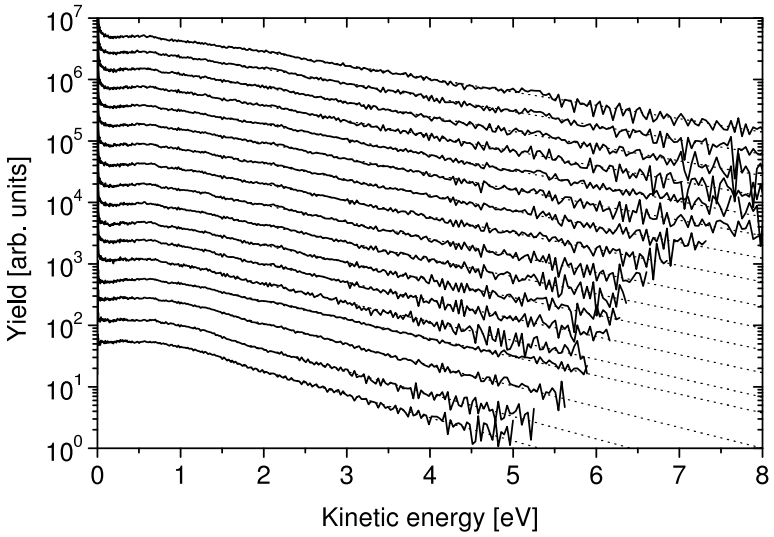

Figure 5.12: Electron spectra of coronene at constant fluence 3.43 J/cm^2. Wavelength 775 nm. From bottom to top the laser pulse durations are: 3440, 2660, 2010, 1299, 974, 779, 659, 590, 507, 444, 380, 329, 292, 241, 216, 179 and 150 fs. The spectra are shifted vertically for display purposes.

The same data as shown in Fig. 5.10 for the stretched laser pulses is shown in Fig. 5.11 but here versus the pulse duration. The electron spectra corre-

sponding to the stretched laser pulses used in Fig. 5.10 and 5.10 are shown in Fig. 5.12 which show that the electron energy distributions for energies beyond the photon energy are strongly dominated by a thermal distribution also for the stretched laser pulses.

5.2.2 Benzo[GHI]Perylene

The same photoelectron measurements, with minor differences in laser intensity, as were performed on coronene with the fundamental wavelength of the fs-laser, 775 nm, were also done for benzo[GHI]perylene. The results are presented in Fig. 5.13 to 5.16. The benzo[GHI]perylene is a close relative to coronene and in analogy to the similarities between the fullerenes C_{60} and C_{70}, no major differences were expected between coronene and benzo[GHI]perylene. Judging from the results presented in Fig. 5.13 to 5.10 they are more or less the same. One minor, but still clear, difference is that the ATI-peaks in Fig. 5.13 are slightly enhanced compared to the coronene PES, most easily seen for the 1.31×10^{13} W/cm^2 spectra. This will however not change the interpretation of the photoelectron spectra for benzo[GHI]-perylene compared to the coronene data so, for a discussion of the data, I will therefore refer to the discussion above in the coronene section.

In addition to the 775 nm measurements on benzo[GHI]perylene the second harmonic, 388 nm, was also used for both mass spectrometry (see the mass spectrometry section above) and for photoelectron measurements. The PES are shown in Fig. 5.17, and the corresponding momentum maps for four of the intensities are shown in Fig. 5.18. First we notice that for all laser intensities the MMs are much more symmetric than the red-light MMs, possibly because of the significantly lower laser intensities applied with the blue light, about one order of magnitude. That is because only three photons are now required for ionization instead of five for the red light. The detailed analysis of the angular photoelectron distribution will be further discussed in chapter 6. Regarding the PES, Fig. 5.17, they are very similar to the ones obtained with the 775 nm light, Fig. 5.13. Outside the photon energy, now 3.20 eV, the spectra are smooth and well described by Boltzmann distributions and there is no sign of a major ATI-series. This is consistent with the transient hot electron ionization process which is not wavelength dependent (except for cross section), as long as the photon energy is smaller than the IP. For the spectrum corresponding to the highest laser intensity 3.73×10^{13} W/cm^2, the two non-ATI peaks at 5.3/6.3 eV appear again. These peaks were also

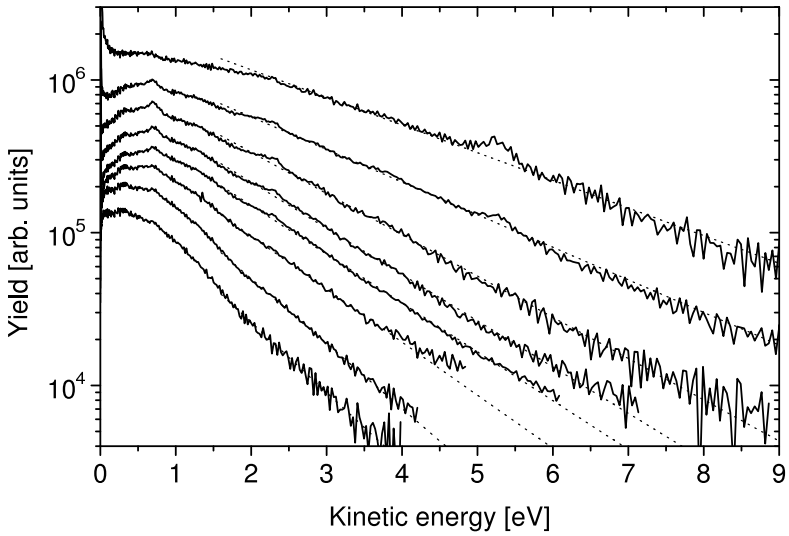

Figure 5.13: Electron spectra of benzo[GHI]perylene at constant pulse duration 150 fs. Wavelength 775 nm. From bottom to top the laser intensities are: 1.78, 2.66, 4.44, 6.22, 7.99, 13.1, 20.9 and 33.3×10^{12} W/cm^2. The spectra are shifted vertically for display purposes.

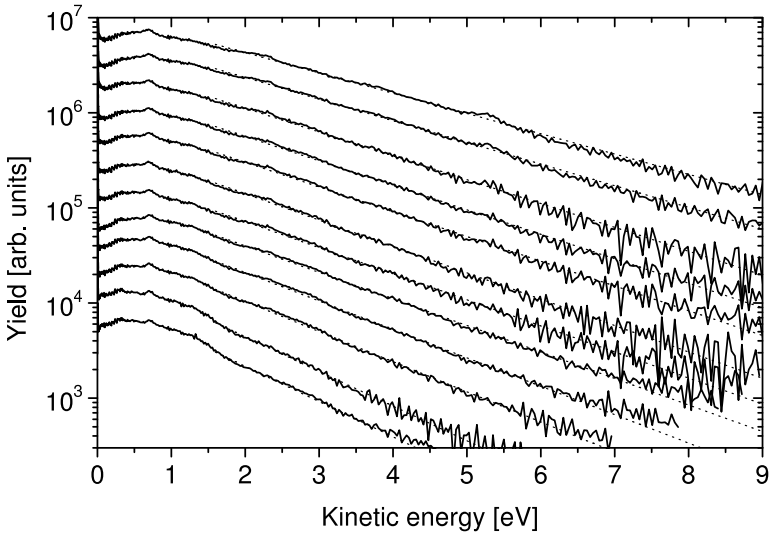

Figure 5.14: Electron spectra of benzo[GHI]perylene at constant fluence 3.26 J/cm^2. Wavelength 775 nm. From bottom to top the laser pulse durations are: 2920, 2270, 1360, 1140, 690, 495, 405, 379, 335, 253, 177 and 150 fs. The spectra are shifted vertically for display purposes.

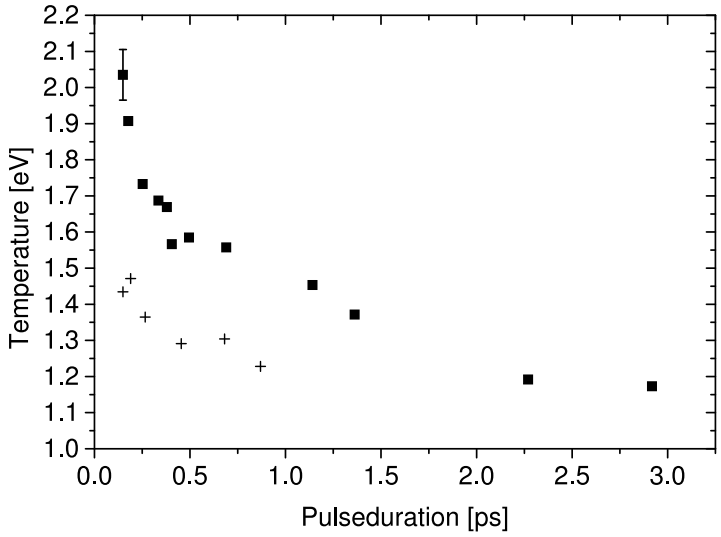

Figure 5.15: Electron temperatures of benzo[GHI]perylene. Squares: fixed laser fluence 3.26 J/cm^2, data from Fig. 5.14. Crosses: fixed laser fluence, 1.27 J/cm^2. Same error bar as in Fig 5.10.

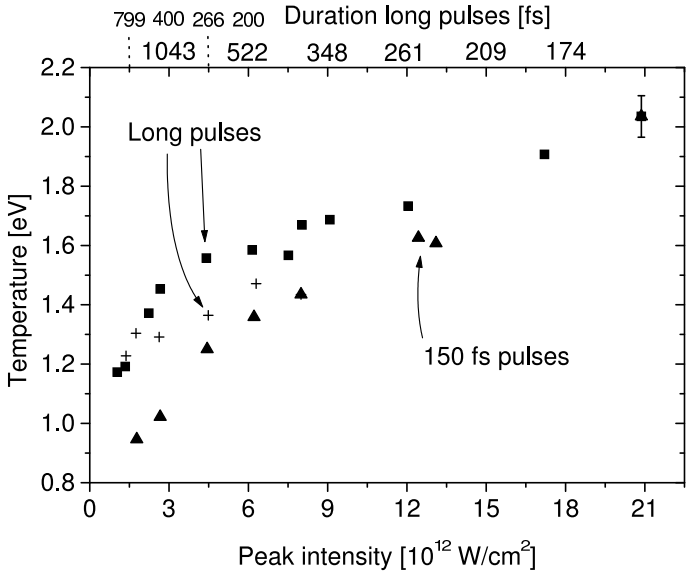

Figure 5.16: Electron temperatures of benzo[GHI]perylene as a function of laser peak intensity. Solid triangles: Varying fluence at 150 fs pulse duration. Solid squares: Varying pulse duration at a fixed laser fluence, 3.26 J/cm^2. Crosses: Varying pulse duration at a fixed laser fluence, 1.27 J/cm^2. Same error bar as in Fig 5.10. Large pulse duration labels refer to solid squares and small numbers to crosses.

observed for all the other molecules with high intensity 775 nm light.

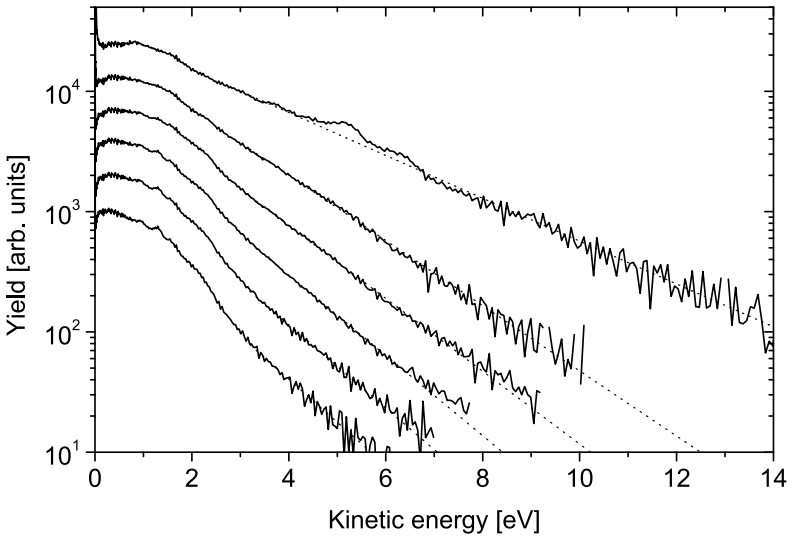

Figure 5.17: Electron spectra of benzo[GHI]perylene. Laser parameters: 150 fs and 388 nm. From bottom to top the laser intensities are 0.43, 0.76, 1.28, 2.22, 6.57 and 37.3×10^{12} W/cm^2. The spectra are shifted vertically for display purposes. A stronger projection field was used here compared to all other photoelectron measurements, which enables detection of photoelectrons of higher kinetic energies.

The PES for high electron kinetic energies (>3.2 eV) in Fig. 5.17 are regarded to be thermal and the electronic temperatures are shown in Fig 5.19. The observed temperatures fall into the same "ball park" as what was observed for 775 nm ionization. Differences are however that the temperatures at low fluences are higher for blue light excitation compared to red light excitation. For higher fluences the difference evens out.

A perhaps more interesting effect seen in Fig. 5.19 is how well the data points for both the 388 nm and 775 nm light fit with a square root dependence on the laser fluence which is consistent with a transient hot electron ionization mechanism [35]. The temperature in a Fermi gas goes as $T_{el} \propto \sqrt{U}$, where U is the internal thermal energy and where U, in a crude estimate is, directly proportional to the laser fluence, in case of a constant, time independent, cross section.

A careful look at the same plot for the fullerenes, Fig. 4.7 reveals a similar trend for C_{60} and for C_{70} at low fluence. Data points for equally low fluences

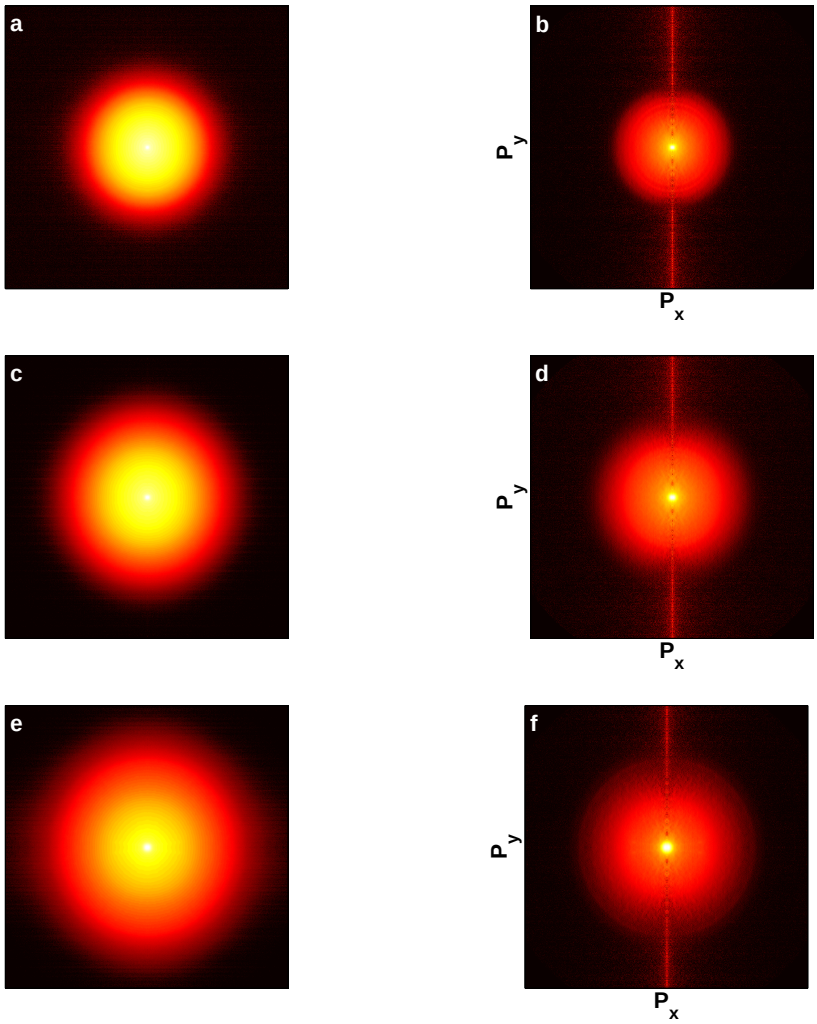

Figure 5.18: Electron momentum maps of benzo[GHI]perylene after 150 fs, 388 nm ionization. Left column are symmetrized images and right column are the inverted images. Laser peak intensities are for **a** & **b** 0.43, **c** & **d** 6.57 and **e** & **f** 37.3×10^{12} W/cm^2.

as for benzo[GHI]perylene are however not available here. For coronene, Fig. 5.9, the curve is different but the trend is also that the temperature rise is more rapid at the low fluences up to ca. 2 J/cm^2.

A comparison of the electronic temperatures with the mass spectra of 775 nm and 388 nm light gives more information. In Fig. 5.20 mass spectra are shown for 388 nm and 775 nm of 150 fs duration and also for 775 nm of longer pulse durations. The mass spectra of every row are selected to have similar elec-

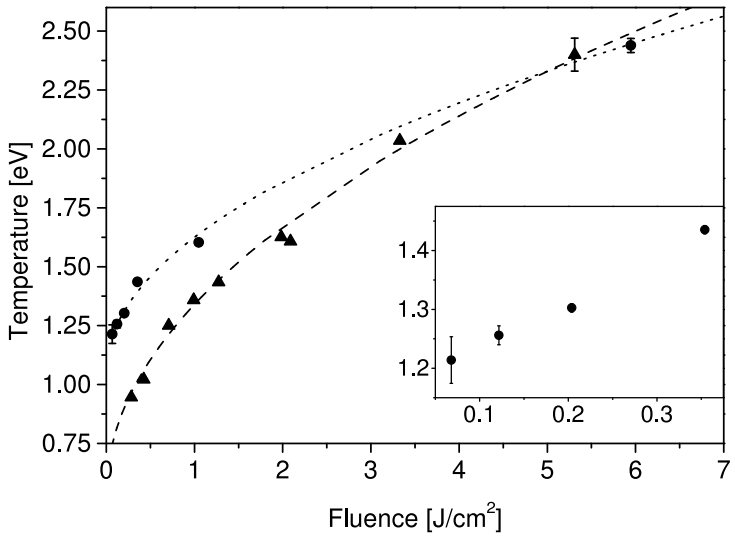

Figure 5.19: Apparent electronic temperatures for benzo[GHI]perylene extracted from the PES in Fig. 5.13 and 5.17. Solid circles 388 nm excitation and solid up triangles 775 nm excitation. Inset shows the 388 nm data for the four lowest fluences. The lines are "hand made" fits of the form $A+\sqrt{F}B$, where F is the laser fluence and A and B are constants. 775 nm: A=0.54 eV, B=0.8 eV/(J/cm^2)$^{1/2}$. 388 nm: A=1.055 eV B=0.57 eV/(J/cm^2)$^{1/2}$.

tron temperatures. For the 150 fs, 388 nm and 775 nm, laser pulses it is clear that the mass spectra evolve similarly for increasing electron temperatures. A somewhat stronger fragmentation is observed for the red pulse for the lowest temperatures, compare Fig. 5.20**a** to **b**, and **d** to **e**. This is however inside the uncertainties of this comparison. Now, considering the mass spectra for the stretched 775 nm pulses, Fig. 5.20**c**, **f** and **i**, these show a strong fragmentation, at all electron temperatures, much different from what is observed for the 150 fs pulses. Also this observation is consistent with a thermal ionization process. The blue and red 150 fs pulses heat the electron system quickly, resulting in a transient hot electron ionization. The process is statistical and not state specific and therefore the hot electron system has no memory of how it was excited (blue or red light). Hence, electron systems that are equally highly excited, emit electrons of the same emission temperature leaving ions behind with equal charge states and excitation energy, which then couple to the vibrational modes, leading to the same fragmentation pattern. For the longer, 775 nm pulses, the photon absorption is not quick enough to prevent substantial quenching of excitation energy into the vibrational modes during the laser pulse. Therefore, these pulses result in

strong fragmentation already at low electron temperatures since a lot of the excitation energy has coupled between the electronic and vibrational subsystem before electron emission takes place. Figure 5.20 is consistent with, although no proof of, a thermal ionization mechanism of benzo[GHI]perylene.

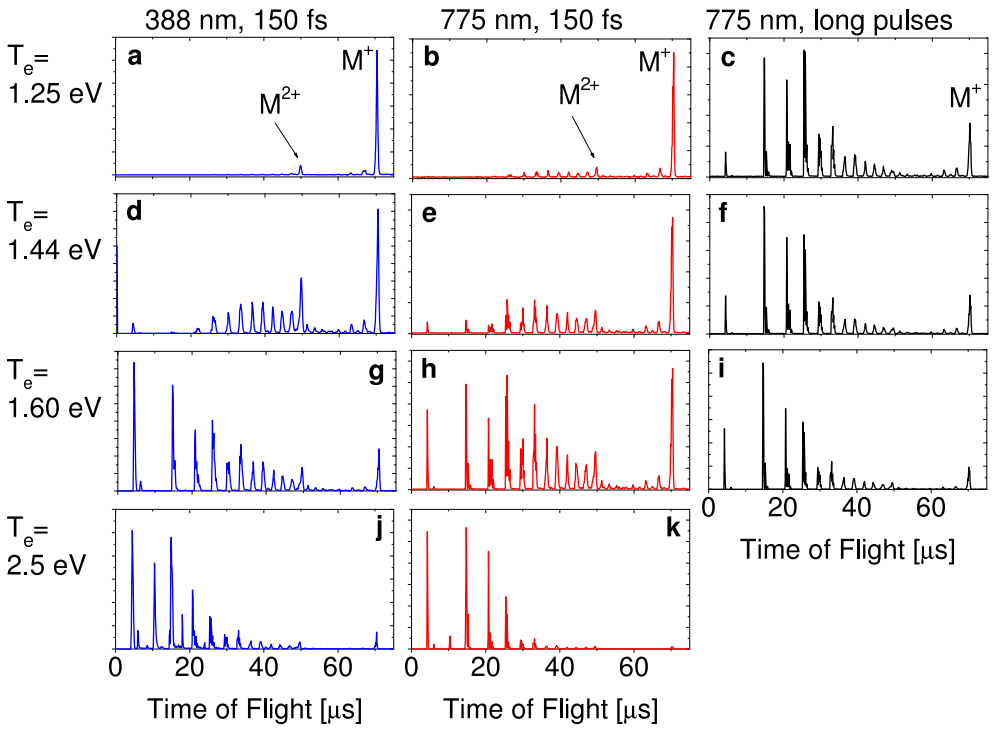

Figure 5.20: Mass spectra of benzo[GHI]perylene at different laser intensities, wavelengths and pulse durations. The figure shows that similar electron temperatures gives similar mass spectra for both 775 nm and 388 nm laser light when the pulse is short, 150 fs. The mass spectra corresponding to stretched pulses (**c** 2270 fs, **f** 1360 fs, **i** 380 fs), at constant laser fluence 3.26 J/cm^2, give a stronger fragmentation pattern already at the lowest laser intensity in (**c**).

5.2.3 Anthracene

The electron spectra of anthracene after 150 fs, 775 nm ionization are shown in Fig. 5.21, where the laser intensities are similar to those used in the mass spectrometry measurements, presented in Fig. 5.6. The electron spectra are

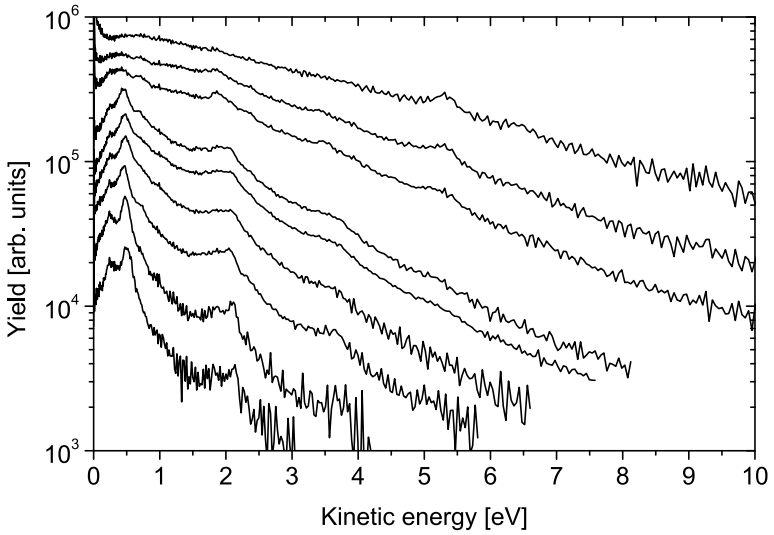

Figure 5.21: Electron spectra of anthracene at constant pulse duration 150 fs. Wavelength 775 nm. From bottom to top the laser intensities are: 1.78, 3.11, 4.44, 7.99, 9.32, 10.88, 20.65, 27.31 and 61.05×10^{12} W/cm^2. The spectra are shifted vertically for display purposes .

dominated by series of ATI-peaks for the intensities up to ca 10^{13} W/cm^2. The ATI-peaks are clearly seen as rings in the momentum map in Fig. 5.22.

At higher laser intensities the spectra are seen to be smeared out to a smooth distribution of exponential form. It is not possible to say what causes this transition but candidates are tunneling ionization or the onset of a strong thermal ionization process.

Comparing the photoelectron spectra of anthracene, at relatively low laser intensities, to those of the fullerenes C_{60} and C_{70} and the PAH-molecules coronene and benzo[GHI]perylene it is clear that the thermal component, due to the transient hot electron emission, is suppressed in favor of the ATI-series. The fact that the ATI-peaks become more dominant for anthracene than for the larger molecules is unknown. It may be a result of the smaller molecular system and the smaller number of delocalised electrons for anthracene which makes a thermal ionization process less probable. The results presented here are in agreement with the electron spectra reported by Levis *et al.* [7] and [8, 23], which are discussed in the Background chapter, where smaller molecules were observed to enhance the ATI-peak structures. Their interpretation of the spectra were however different.

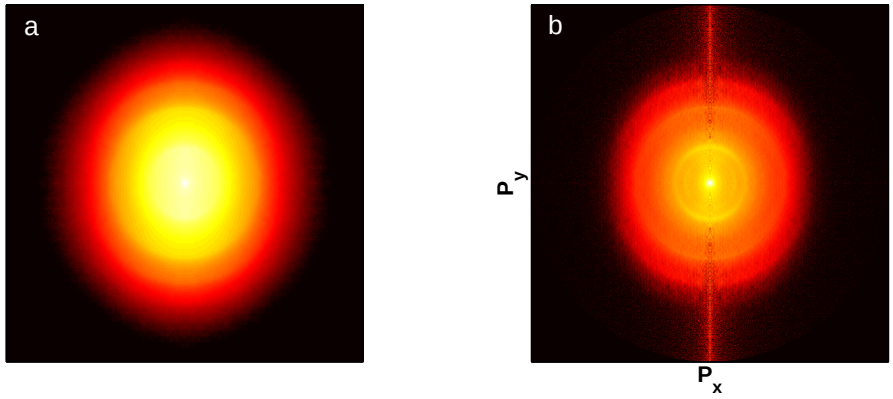

Figure 5.22: Momentum map of anthracene, **a**: symmetrized image and **b**: inverted image. Laser parameters: 775 nm, 150 fs and 7.99×10^{12} W/cm^2.

ATI-ionization and a transient hot electron ionization mechanism can be active at the same time, and the strong ATI-peaks in the anthracene spectra do not exclude a thermal component for anthracene. At first glance, all the spectra in Fig. 5.21, could be seen as ATI-peaks superimposed on a thermal component. A fit of Lorentzian peaks to these ATI-peaks, to separate them from a thermal component, is not possible since the ATI-peaks are built up of an unknown number of sub-peaks, corresponding to resonance enhanced ATI-ionization [13, 15–17]. See for example the double peak structure at ca. 0.25 and 0.45 eV and also the shoulder at ca. 0.7 eV.

Instead a thermal component with a temperature of 1.72 eV (dotted line) was subtracted from the PES, giving the bottom spectrum in Fig. 5.23**a**. If the PES is built up of a thermal distribution and an ATI-series, then this is the ATI-contribution to the PES. The first and second ATI-peak were then shifted by one and two photon energies respectively, as indicated by the arrows in Fig. 5.23**a**, and then scaled to have the same peak value. The result is shown in Fig. 5.23**b**, where the black, red and blue curves correspond to the 1:st, 2:nd and 3:rd ATI-peak respectively. Notice that the thermal component cuts the 1:st ATI-peak at low energies so it is only the high energy side of the ATI-peaks that should be compared. Within the experimental uncertainties regarding peak broadening, due to reduced resolution at higher photoelectron energies, and the rather crude method described here, the three peaks are similar. In Fig. 5.23**c** the ATI-peaks were shifted without the subtraction of the thermal component and then scaled to approximately

equal peak values. This gives a slightly worse agreement between the three ATI-peaks.

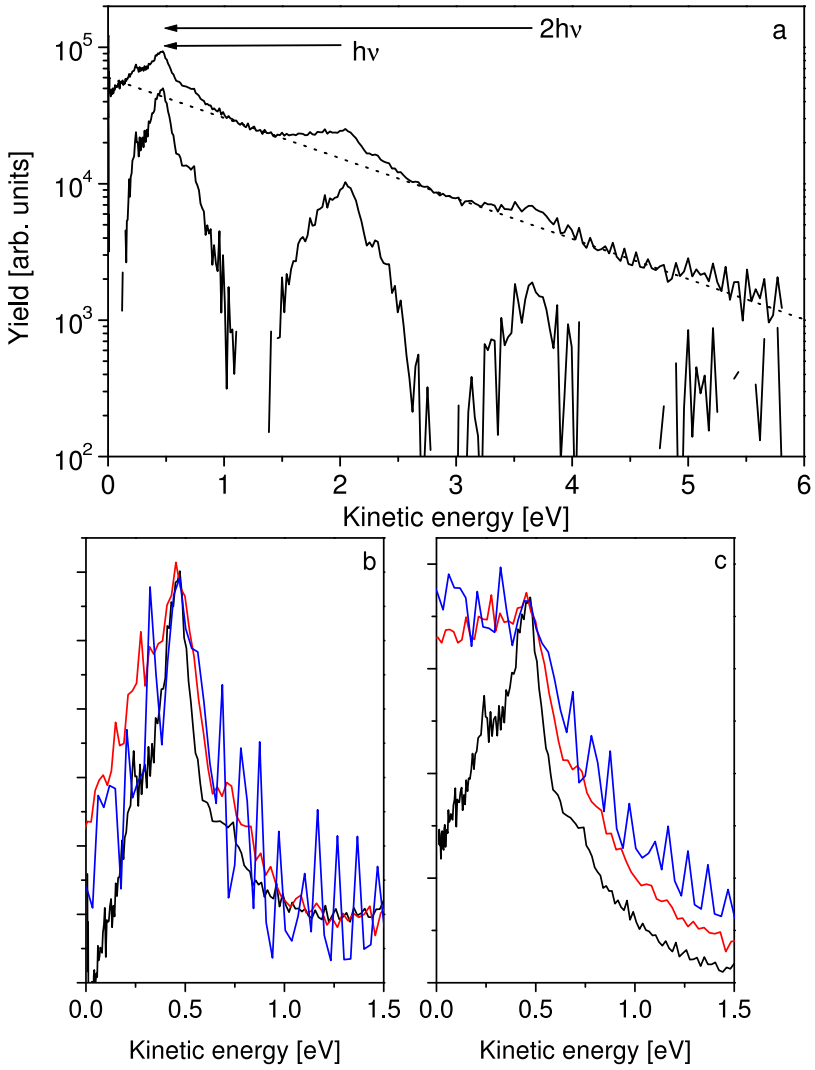

Figure 5.23: **a**: A thermal component (dotted line) is removed from the anthracene PES. The resulting spectrum is shown below. **b**: The second (red) and third (blue) ATI peaks are translated by one and two photon energies and scaled to the same peak value as the first (black) ATI-peak. **c**: Same as **b**, but without a thermal component removed. Laser parameters: 150 fs, 775 nm and 4.44×10^{12} W/cm^2.

The above procedure is arbitrary and it is unclear if there is a thermal ionization process active also for anthracene. Since the ATI-ionization mainly depends on the laser intensity while the transient hot electron ionization also is sensitive to the laser fluence the obvious experiment is to stretch the laser pulse and use a relatively high fluence, and possibly that way conclude whether anthracene ionizes thermally. In Fig. 5.24 the electron spectra recorded at three of the lowest laser intensities and longest pulse durations used in these experiments are shown (black lines) together with two reference spectra (red and blue lines) for 150 fs ionization. The red spectrum corresponds to a similar laser fluence as the black spectra and the blue spectrum to a two times lower fluence. The second ATI-peak at ca. 2.1 eV is clearly seen in the spectra corresponding to long pulse durations, but reduced by a factor of two compared to the 150 fs spectra. This is indicated by the vertical lines under the ATI-peaks. For the bottom spectrum, corresponding to a pulse duration of 1.49 ps and laser intensity of 4.0×10^{11} W/cm^2 the second ATI peak

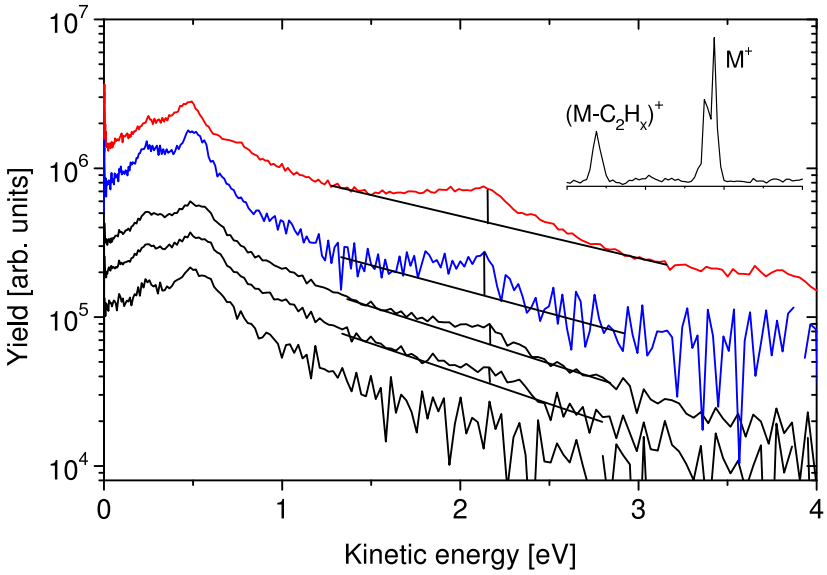

Figure 5.24: Electron spectra of anthracene at three of the lowest laser intensities used in this study (black lines), together with two 150 fs reference spectra (red and blue lines). From top to bottom the laser pulse durations and intensities are: 150 fs/ 4.44×10^{12} W/cm^2, 150 fs/ 1.78×10^{12} W/cm^2, 1.10 ps/ 7.8×10^{11} W/cm^2, 1.49 ps/ 5.8×10^{11} W/cm^2 and 1.49 ps/ 4.0×10^{11} W/cm^2. The spectra are shifted vertically for display purposes. Vertical lines indicates the height of the second ATI-peak. Inset: Mass spectrum corresponding to ionization with a 1.49 ps/ 3.8×10^{11}W/cm^2 pulse.

is revealed when a smoothing function is applied to the spectrum (not shown here). This observation shows that the ATI-series is suppressed and replaced by a smooth, thermal like, photoelectron distribution for longer pulse durations. The inset in Fig. 5.24 shows the mass spectrum of anthracene ionized with a 1.49 ps pulse of peak intensity 3.8×10^{11}W/cm^2, which is the same as what is used in one of the photoelectron measurements. There is no sign of delayed ionization on the mother ion peak (M^+) and hence the smooth electron distribution cannot be attributed to thermionic emission on the μs-ns time scale. This result suggests that also anthracene can ionize thermally from a transient hot electron system, even though the process is suppressed in favor of ATI-ionization.

5.2.4 The non ATI-peaks

The peaks observed in the photoelectron spectra at 5.3/6.3 eV (for coronene also at ca 9.3/10.3 eV) for high laser intensities cannot, due to their position on the energy axis and the 1 eV/4 eV separation, origin from ATI-ionization with 1.6 eV photons. They show no angular dependence in count rate relative to the laser field polarization and they become pronounced in the electron spectra when C^+ and C^{2+} appear in the mass spectra. The explanation for these peaks is suggested to be a secondary electron recombination process followed by electron emission. The first excited state of C^+ (^{4}P $2s2p^2$) is at 5.33 eV and the second excited state (^{2}D $2s2p^2$) at 9.29 eV. The 6.3 eV peak fits rather well with the first excited state of C^{2+} (^{3}P$^\circ$ $1s^22s2p$) at 6.50 eV.

5.3 Conclusions

The large molecules coronene and benzo[GHI]perylene are shown to give rise to smooth electron spectra outside the photon energy after fs-laser excitation, similarly to the fullerenes. Also the development of the mass- and electron spectra with increased pulse duration follow a similar scheme as the fullerenes. The transient hot electron ionization mechanism, active for fullerenes, is therefore most likely present also for coronene and benzo[GHI]perylene. Going to anthracene the ATI-series becomes significantly more dominant in the electron spectra. The results do however suggest that the transient hot electron ionization mechanism is present also for anthracene, but suppressed in favor of direct ATI-ionization.

Chapter 6

Anisotropy in the photoelectron distributions.

Throughout this thesis it has been argued for multielectron dynamics and a thermal ionization process of large molecules after fs-laser excitation. The distribution of emitted particles in a thermal/statistical decay is expected to be isotropic. The photoelectron momentum maps of the fullerenes and PAH-molecules in chapters 4 and 5 did however show a prolongation in the direction of the laser polarization which at first points against a thermal ionization mechanism. In this chapter some of the previously presented data are analyzed as a function of emission angle relative to the laser polarization direction.

The theoretical analysis is far from completed and this chapter mainly serves as a presentation of the experimental data. A model, taking the laser field into account in a thermal ionization process is also presented.

6.1 Results and observations

The photoelectron spectra of coronene after 775 nm, 150 fs, excitation at emission angles 0-10, 40-50 and 80-90 degrees are presented in Fig. 6.1. From this figure it is clear that the photoelectron distribution along the polarization is flatter (has a higher effective temperature) than the distribution perpendicular to the polarization. Further, thermal distributions dominate for all

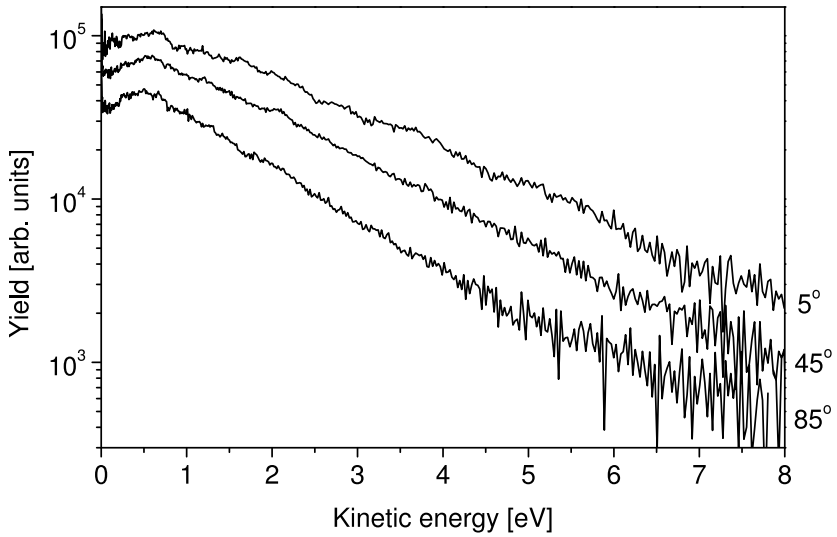

Figure 6.1: The photoelectron spectrum of coronene for the emission angles 0-10°, 40-50° and 80-90° relative the laser polarization axis. The laser polarization direction corresponds to 0°. The laser peak intensity is 1.15×10^{13} W/cm^2, pulse duration 150 fs and wavelength 775 nm.

three spectra but with weakly visible resonance structures, which are possibly ATI-peaks, in the polarization direction. This is consistent with the observation made in for example Fig. 3.3 of xenon or Fig. 5.22 of anthracene where the ATI-peaks are stronger in the laser polarization direction. More important is however that the thermal distributions observed after integration of the whole momentum map, which was done in chapter 4 and 5, cannot be attributed to smearing, caused by the ellipticity of the distribution, since thermal distributions are observed also for small angular segments. This is a general observation for all molecules showing thermal electron spectra.

The temperatures and the number of counts for 9 angular segments between 0° and 90° are shown in Fig. 6.2 for three different laser intensities. A clear trend is that the asymmetry increases both for the count rate and the electronic temperature with increasing laser intensity.

To exclude that the asymmetry is caused by experimental artifacts the polarization was flipped by 90°, so that it pointed into the detector plane. This was done for C_{70} and the result is presented in Fig. 6.3. With a polarization perpendicular to the detector the count rate and the apparent electron temperature are nearly constant for all emission angles and the variations

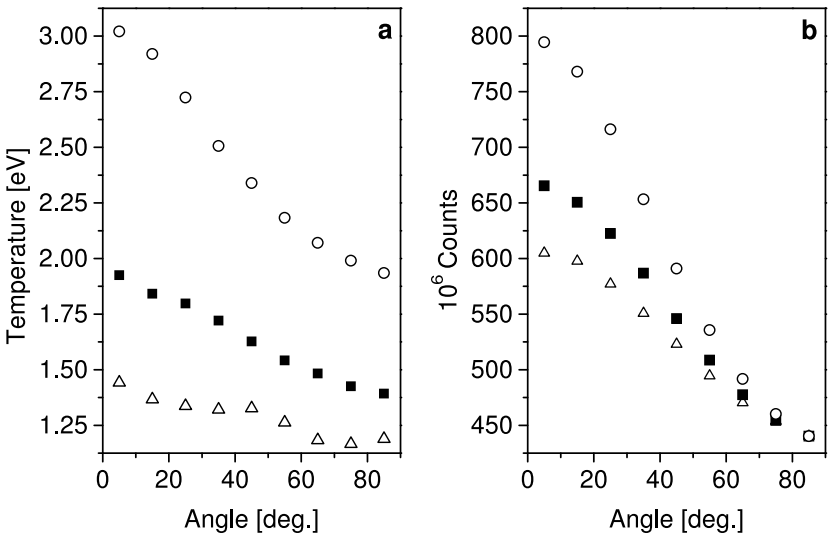

Figure 6.2: **a**: The angular dependence on the apparent electron temperatures for three different laser peak intensities for coronene. Open triangles 6.66×10^{12} W/cm^2, solid squares 1.15×10^{13} W/cm^2 and open circles 2.75×10^{13} W/cm^2. **b**: The corresponding number of counts which are normalized to the same number at 80-90°.

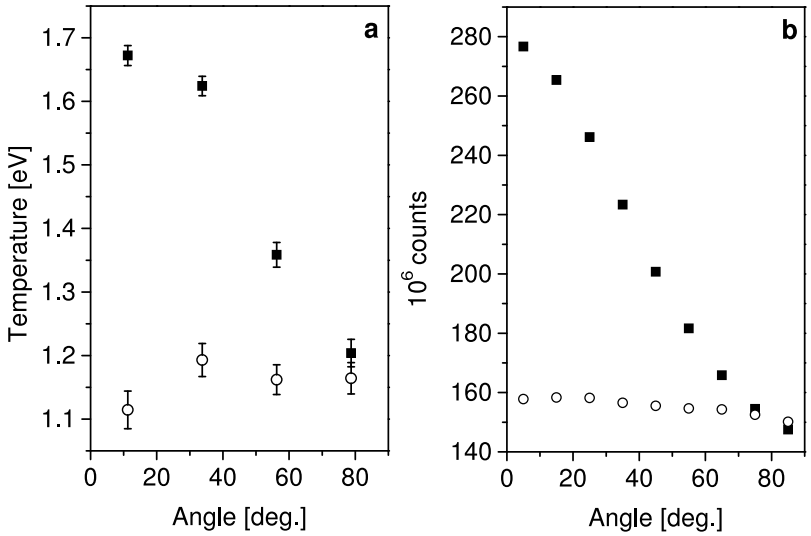

Figure 6.3: **a**: The angular dependence on the apparent temperature for C_{70} for perpendicular (open circles) and parallel (solid squares) laser polarization with respect to the detector plane. **b**: The corresponding number of counts. Laser parameters: 775 nm, 150 fs and 1.07×10^{13} W/cm^2.

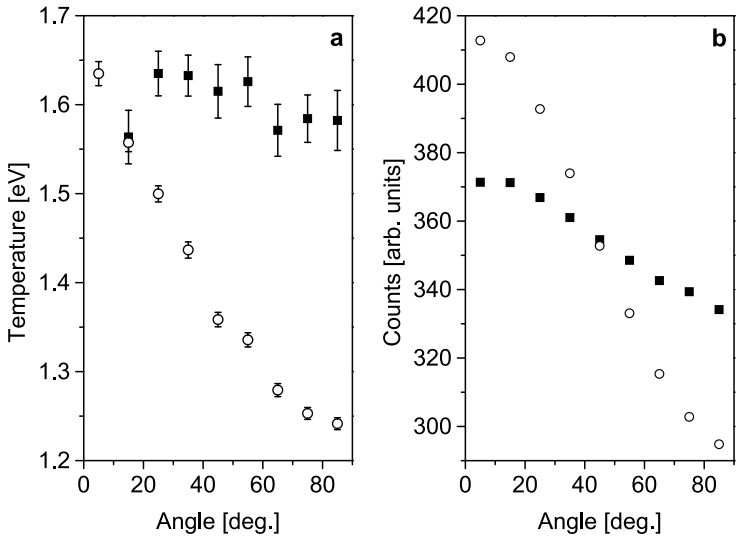

Figure 6.4: **a**: The angular dependence on the apparent temperature for benzo[GHI]perylene after 775 nm (open circles) and 388 nm (solid squares) at laser intensities 6.22×10^{12} W/cm^2 and 6.57×10^{12} W/cm^2 respectively. **b**: The corresponding number of counts.

observed lies within the experimental uncertainties. This result establishes that it is the laser field that is responsible for the ellipticity of the electron distributions.

Finally a comparison is made for benzo[GHI]perylene for 388 and 775 nm excitation at similar laser intensity shown in Fig. 6.4. The momentum maps of benzo[GHI]perylene after 388 nm excitation in Fig. 5.18 did not show a pronounced prolongation compared to 775 nm excitation (Fig. 5.8 for coronene is representative), even though the laser intensities are similar. That is also verified in Fig. 6.4 where the 775 nm light ionization is seen to result in a stronger angular dependence. One possibility for this is that it is not the peak intensity alone of the laser field which is the most important parameter. Instead it suggests that it can be the ponderomotive potential and/or the Keldysh parameter, eq. 2.3 and 2.4, which are both intensity and wavelength dependent. An increased wavelength results in a higher ponderomotive potential and a stronger suppression of the binding potential. A second possibility is that with 388 nm light the molecules ionize earlier in the rise of the laser pulse, at lower intensities. For example, only 3 photons are required for ionization compared to 5 photons for 775 nm light.

6.2 Thermal electron emission in an electric field

The transient hot electron ionization mechanism is based on detailed balance as applied by Weisskopf to describe neutron emission from hot nuclei [44]. The rate constant for statistical emission of electrons from an electronic heat bath reads

$$k(E,\epsilon)d\epsilon = \frac{2m_e\sigma(\epsilon)}{\pi^2\hbar^3}\epsilon\frac{\rho_d(E-\Phi-\epsilon)}{\rho_p(E)}d\epsilon, \tag{6.1}$$

where m_e is the electron mass, σ the electron capture cross section, ϵ the kinetic energy of the electron, E the total excitation energy, Φ is the ionization potential and ρ_p and ρ_d are the level density of the parent and daughter respectively [35]. The factor of 2 is the spin degeneracy of the electron. We can further assume that the hot electron gas has an excitation energy which is much greater than both the ionization potential and the kinetic energy of one emitted electron. Hence the heat capacity can be considered constant when an electron is removed and also the temperature of the electron gas is unaffected. Equation 6.1 can then be approximated with Boltzmann expansions of the daughter level density, $\rho_d(E-\Phi-\epsilon)$, as

$$k(E,\epsilon)d\epsilon = \frac{2m_e\sigma(\epsilon)}{\pi^2\hbar^3}\epsilon\frac{\rho_d(E)}{\rho_p(E)}\exp\left(-\frac{\Phi}{k_BT}\right)\exp\left(-\frac{\epsilon}{k_BT}\right)d\epsilon. \tag{6.2}$$

The idea is that the ionization potential is varying in time when the electric field oscillates and that the suppression of the potential is directional, along the laser polarization axis. That is,

$$\Phi(t) = \Phi_0 + qE_0r_0\sin(\omega t)\cos(\theta), \tag{6.3}$$

where Φ_0 is the undisturbed ionization potential, E_0 is the electric field strength, r_0 the radius of the molecule, ω the frequency of the laser field and θ the angle relative to the laser polarization. This does not lower the ionization potential when averaged over a whole period since the second term vanishes, but since the ionization potential goes into the exponent in eq. 6.2 it does affect the distribution of photoelectrons, with an enhanced yield in the direction of the laser polarization.

Chapter 7

Molecular fusion of fullerenes

In this chapter the redistribution of energy in highly excited molecules will be studied on a different system, clusters of fullerenes. The cold source described in chapter 3 produces clusters of fullerenes (Fig. 7.1), where the intramolecular bonds are of weak van der Waals type. Clusters of fullerenes were ionized by both the F_2- and femtosecond laser (775 nm, 150 fs), perpendicular to the cluster beam, and analyzed with the mass spectrometer. The mass spectra revealed unexpected results after fs-laser ionization. The chapter is based on Papers III-V.

7.1 Results and discussion

A mass spectrum of the cluster distribution generated by the cold source is shown in Fig. 7.2**a**. The clusters were ionized with a F_2-laser which has a photon energy 7.9 eV, which is 0.3 eV higher than the ionization potential of C_{60}. One electron is removed from the fullerene in a direct ionization process, leaving the electronic and vibrational systems cold and the cluster unaltered by the ionization. Hence, this is a fingerprint of the cluster distribution generated by the cold source. Two distributions of cluster sizes are seen in Fig. 7.2**a**, one is centered around N=15-20 (inset) and then a second one of unresolved peaks starts at ca. N=50 and extends up to hundreds of C_{60} molecules. The by far most abundant sizes in the spectrum are the monomers and dimers which exceeds the scale in this figure. These do however have a much higher detection efficiency than the largest clusters in the spectrum. The cluster size distribution is very sensitive to the carrier gas

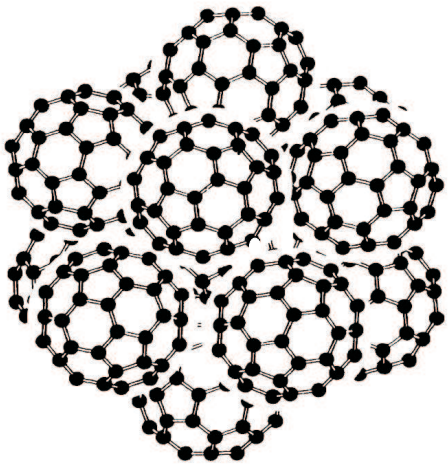

Figure 7.1: Cluster of C_{60}. Figure from [75].

pressure and the trend is that larger clusters are created at higher pressure. This is further discussed in Papers III and IV.

The corresponding mass spectrum after fs-laser ionization is shown in Fig. 7.2**b**. The C_{60}^+ peak with fragments (C_{58}^+, C_{56}^+...) dominates the spectrum completely and there seems to be no trace of clusters of fullerenes. The tail on the high mass side of the C_{60}^+ peak is not delayed ionization but due to fragmentation of cluster ions to C_{60}^+ during the acceleration time in the spectrometer. Zooming in on the high mass side of the C_{60}^+ peak does however reveal four small groups of peaks, where the peaks are separated by C_2-units, indicating fragmentation of excited fullerenes.

These four groups are surprising for two reasons. First of all, in contrast to the C_{60}^+ fragments (C_{58}^+, C_{56}^+...) which show a monotonic decrease in abundance (except local stability effects), these distributions peak and are close to symmetric around a specific fragment size. This will be discussed later. Secondly, their positions in the mass spectra are surprising. The position where the $(C_{60})_2{}^+$ peak is expected is indicated in Fig. 7.2**b** and it is reasonable to assume that the left most distribution of fragments are originating from this dimer ion. The intramolecular van der Waals bond of the $(C_{60})_2{}^+$ ion is however very weak (ca 0.4 eV [87]) compared to the C_2 evaporation energy of C_{60} (ca. 11 eV) and it is therefore very unlikely that the two C_{60} cages stay together while one or both evaporate C_2 units, leading to the fragment

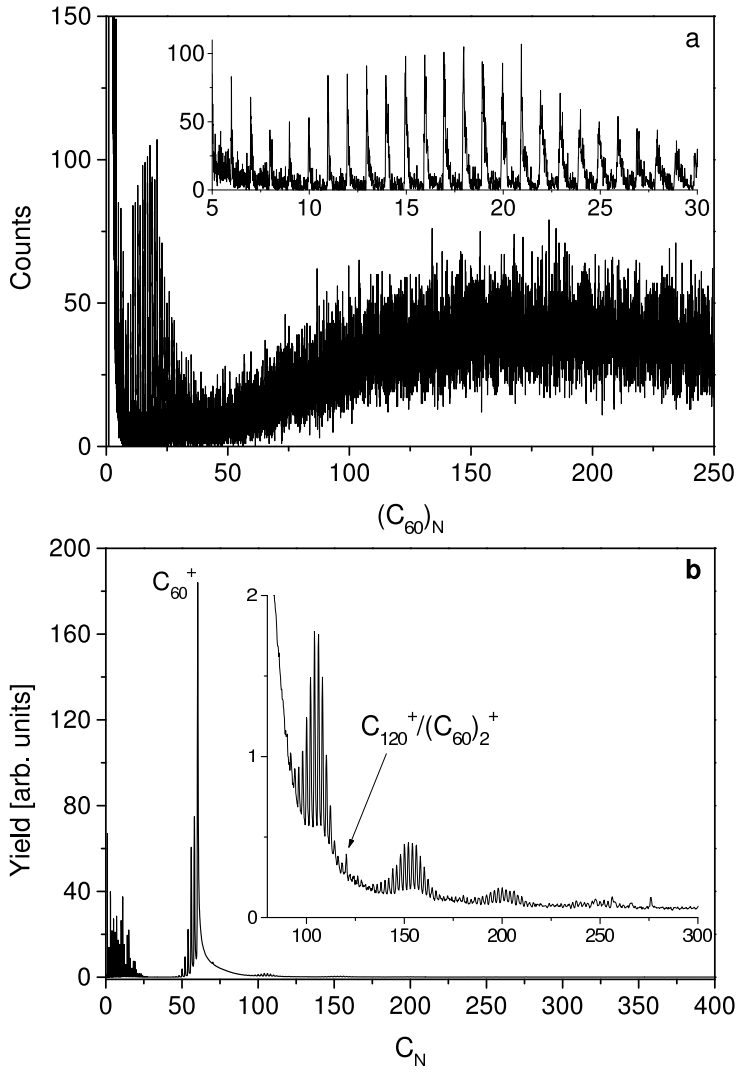

Figure 7.2: **a**: Single photon ionization of $(C_{60})_N$ showing the precursor distribution. **b**: The corresponding mass spectrum after 775 nm, 150 fs radiation at laser peak intensity 1.73×10^{14} W/cm^2.

distribution which is centered at 106 carbon atoms. They will rather first fall apart to C_{60} monomers which then fragment. So there must be another decay route to the fragment distributions observed in Fig. 7.2**b**.

What is suggested here is a rapid fusion of the C_{60} cages upon femtosecond laser excitation, creating a highly excited C_{120}^+ fullerene which decays by C_2 evaporation. Femtosecond laser excitation is crucial here since the

electronic system must be heated to extreme temperatures to overcome the fusion barrier of ca. 80 eV before too much energy is transferred to the vibrational system, causing the weakly bonded cluster to fall apart. Because of this reason, fusion of gas phase fullerene clusters is never observed after multi-photon ns-excitation. Notice that this is the same description of *transient hot electrons* which is used to explain the high apparent electron emission temperatures of fullerenes and PAH molecules in chapter 4 and 5.

Fusion of fullerenes has been observed before by a number of groups. Yeretzian *et al.* reported molecular fusion of fullerenes in the hot and dense vapour generated by laser desorption of a fullerene film [88–90]. The vapour expanded into a pulsed flow of helium carrier gas and was analyzed in a time of flight mass spectrometer. Spectra analogous to the one in Fig. 7.2**b** were observed, except that the fragment groups were centered closer to the precursors.

Also in single collision experiments, $C_{60}{}^{+}$+C_{60}, $C_{60}{}^{+}$+C_{70} and $C_{70}{}^{+}$+C_{70} fusion of fullerenes has been observed [91, 92]. The fusion barrier of C_{60}+$C_{60}^{+}\rightarrow$ C_{120}^{+} was experimentally measured to 60-80 eV in good agreement with molecular dynamics simulations and it was found that the fusion barrier increases with increasing size of the fullerenes. As the collision energy increases it was also observed that the fused fullerenes fragment stronger due to a higher excitation energy.

The shape of the fusion fragment distribution is understood as follows. The high mass cut-off is defined by the minimum amount of fragmentation that a fused C_{120}^{+} will undergo on the experimental timescale. The excitation energy is at least ca. 100 eV resulting from the fusion barrier of 80 eV and the heat of fusion ca. 20 eV [93]. The high mass cut-off dependence on the fusion barrier is seen in Fig. 7.3 as a shift of the peak position of the fusion fragments. For C_{70} the peak position is shifted by 2-3 C_2 units compared to C_{60} which is consistent with a higher fusion barrier for C_{70} [91, 92]. Similarly the excitation energy is larger for the fused $C_{240}{}^{+}$ and hence the fragmentation is stronger than for $C_{180}{}^{+}$ and $C_{120}{}^{+}$. The number of lost C_2 units to the center of the fragment distributions are 20, 14 and 8 C_2 units respectively.

The low mass cut-off is not that easily understood. In [94], Fig. 2, it is shown that the low mass cut-off stays constant when the fluence is varied and it is further observed that the yield of fusion fragments is reduced when the fluence exceeds a certain limit. The naive thought here is that by increasing the fluence there will be more energy available for the fullerenes to fuse which

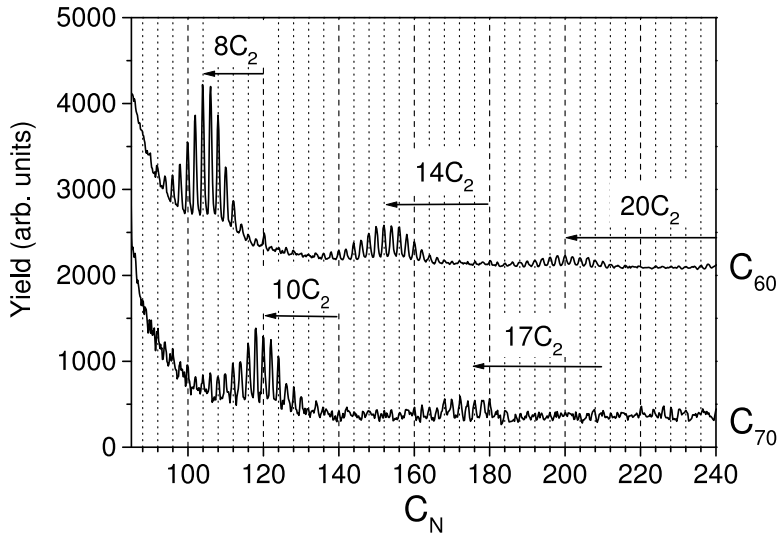

Figure 7.3: Fusion fragment distributions for C_{60} and C_{70}. The effect of a higher fusion barrier for C_{70} is seen as a larger shift of the fusion fragments from its precursor.

would increase the yield and also move the low mass cut-off to smaller masses.

The observation is explained as being due to the onset of a competing decay channel - multiple ionization. With the huge laser fluences applied here the $(C_{60})_2{}^+$ dimer ion will be extremely hot (50 000 K) during and a few hundred fs after the laser pulse has passed [35]. If it gets too hot the double ionization decay channel will become dominant over the fusion channel and due to the high charge mobility of fullerene clusters it is reasonable to assume that two singly charged monomers are created and separated by Coulomb repulsion [95] before fusion takes place. No C_{60}^{2+} ions are observed in the mass spectrum in Fig. 7.2**b**. This explains both the stable low mass cut-off with increased laser fluence and the reduced yield of fusion products at high laser fluences. The excited monomer ions will, after coulomb repulsion and when energy has coupled to vibrations, decay by C_2 evaporation. This is probably why the C_{60}^{+} peak dominates the spectra and why we never see any doubly charged clusters of fullerenes after ionization with the fs-laser. The competition between fusion and multiple ionization is further discussed in Paper IV where a simple model in a satisfactory way explains and reproduces the shape of the fusion fragment distributions.

The fusion fragment distributions have also been studied for different precursor distributions, Fig. 1 and 2 in Paper III and IV. The main observation in these experiments was that the yield of fusion fragments increases when there are many large, N>100, $(C_{60})_N$ clusters in the cluster beam, indicating that the fusion fragments we do observe have their origin in large clusters. Apart from that the shape of the fragment distributions were observed to be fairly stable for varying precursor cluster size.

The last study on the molecular fusion of fullerenes is a pump-probe (PP) experiment. The experiment was performed on C_{60} and at source conditions giving large $(C_{60})_N$ clusters. The femtosecond laser beam was divided into two identical beams in a Michaelson interferometer and the delay time, Δt, between the pump and probe beams was controlled by moving one of the mirrors in the interferometer. The laser fluence was adjusted, by defocusing the light, to not give rise to any fusion fragments in the mass spectra with the pump beam alone. A smooth background was subtracted from the spectra and the total dimer fusion signal was integrated. A normalized fusion fragment yield is seen as a function of Δt in Fig. 7.4, where a delay of 300 fs corresponds to unity. The dashed line is a decay fit curve with a decay constant of 630 fs.

In analogy to the previous discussion on the apparent electron temperature for different laser pulse durations, Fig. 11 Paper I and ref. [34], it is tempting to interpret the reduced fusion signal with increased pump-probe delay as electron-phonon coupling which cools the electronic system and reduces the probability for fusion. Electron-phonon coupling is part of the reason for the reduced signal with increased PP-delay but there are most likely others too and therefore the decay constant observed here cannot be identified with the electron-phonon coupling time. Even though the laser fluence of the pump pulse alone is too small to produce fused molecules it is still strong enough to completely vaporize the cluster into C_{60} molecules. Hence, there will be losses of molecules from the cluster between the pump and probe pulse and we know that the size of the cluster affects the yield of fusion products. Secondly, the vibrations will be heated to varying degree depending on the PP-delay time which may alter the photon absorption cross section. These two effects, at least, will influence the observed decay time.

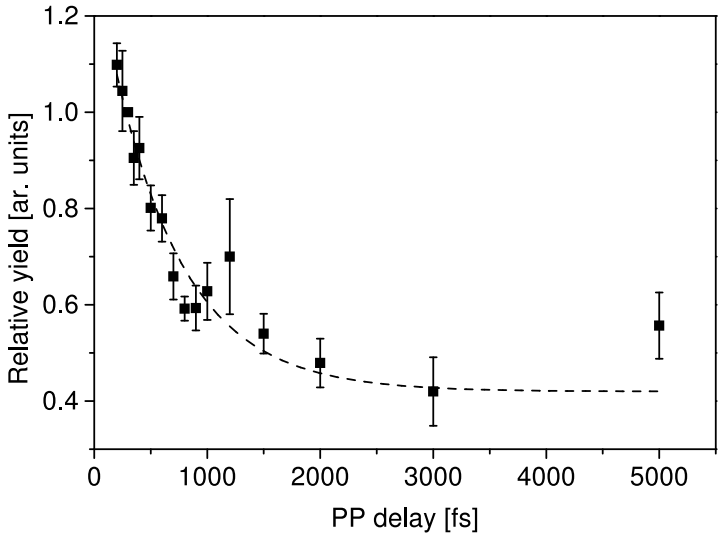

Figure 7.4: Pump-probe ion yield, y, of the integrated dimer fragment distribution. Dashed line is an exponential fit of the form $y = y_0 + C{\cdot}\exp(-\Delta t/\tau)$, where y_0=0.42, C=0.90 and the decay constant τ=630 fs.

7.2 Conclusions

Clusters of fullerenes are shown to fuse after fs-laser excitation. The highly excited fused fullerenes decay via C_2 evaporation. The fragment distribution is defined by the fusion barrier and the competing decay channel, multiple ionization. Further, no intact clusters ions are observed in the mass spectra after intense fs-excitation which show that the clusters are completely evaporated.

Chapter 8

Conclusion & Outlook

The decay dynamics of polyaromatic hydrocarbons, fullerenes and clusters of fullerenes after fs-laser excitation has been studied by mass- and electron spectroscopy.

A momentum-map photoelectron spectrometer has been installed and the performance has been checked on reference systems. For optimization of resolution and energy calibration, the above threshold ionization rings of xenon have been used. The xenon momentum-maps are similar to the ones reported in [17]. Photoelectron spectra of C_{60} after ns- and fs-excitation have been extensively studied before [34, 35, 53] and served as additional tests of the detector performance.

The electron spectra after 150 fs, 775 nm, excitation were found to be dominated by Boltzmann like distributions beyond the photon energy but of much higher temperatures than what is observed with ns-excitation, on the order of 1.5 eV (17000 K). They were also found to depend on laser fluence and the results are in good agreement with the data published in [35]. For these short laser pulses the excitation energy is equilibrated in the electronic system before energy couples to vibrations after a few hundred femtoseconds. A transient highly excited electron system is created from which electrons of high kinetic energies are emitted statistically [34, 35].

Photoelectron spectra with a dominating thermal component outside the photon energy were observed also for C_{70}, coronene and benzo[GHI]perylene after 150 fs, 775 nm, laser excitation and it was therefore suggested that the *transient hot electron* mechanism is present also for these molecules. This

argument was strengthened by the observation that the mass spectra of the PAH-molecules develop similarly to the fullerene spectra with pulse duration and fluence variations. For anthracene it was observed that the ATI-series became significantly stronger. The suppression of the thermal component for anthracene is tentatively assigned to be the result of fewer delocalized electrons compared to the larger PAH-molecules and fullerenes. ATI-peaks were observed even for ionization with pulse durations longer than 1 ps. The hight of the ATI-peaks were however reduced compared to a smooth background distribution of thermal shape, which suggests that transient hot electron ionization is present for anthracene too.

Photoelectron spectroscopy measurements have been performed on C_{70}, coronene and benzo[GHI]perylene for varying laser pulse durations at fixed laser fluence. With increased pulse duration, decreased electron temperatures were observed. This was an expected result due to electron-phonon coupling. The same data could also be used to exclude field ionization as the main cause of the smooth photoelectron distributions. It was observed that the spectra could have identical apparent temperatures for laser pulses of different peak intensities as long as the pulse of lowest intesity was longer in duration (higher fluence). This finding is consistent with a thermal ionization process but inconsistent with a field ionization mechanism.

The momentum-maps of all the studied molecules after 775 nm, fs-laser ionization showed a prolongation of the distribution along the axis of the laser polarization. Thermal distributions were observed in all emission directions but the count rate and electron temperatures were higher in the laser polarization direction. The anisotropy increases with increased laser intensity. With 388 nm radiation of the same intensity as the 775 nm light, the asymmetry is less pronounced. A lowering of the ionization potential in the laser polarization direction was suggested to affect the rate constant for thermal electron emission, causing the asymmetric momentum-maps.

The decay dynamics of clusters of fullerenes excited by fs-laser pulses has also been studied. In [94] molecular fusion of $(C_{60})_N$ clusters was observed after fs-laser excitation. Further studies of the fusion process have been done in this work. Experiments on the precursor size dependence showed that large precursors leads to a higher yield of fusion products indicating that evaporation of fullerens from the cluster limits the process. Apart from that the fusion fragment distributions were found stable in position in the mass spectra with varying precursor cluster size. The higher fusion barrier of C_{70} compared to C_{60}, leading to a higher excitation energy, was experimentally

observed as a stronger fragmentation of the fused $(C_{70})_N$ clusters. The shape of the fusion fragment distribution was shown to depend on the fusion barrier, defining the high mass cut-off in the resulting mass spectra, and the competition between molecular fusion and multiple ionization, which define the low mass cut off. Pump-probe studies on the fusion fragment yield of $(C_{60})_N$ clusters gave a decay constant of 630 fs. This decay constant is similar to, but cannot be identified as, the electron-phonon coupling time.

Open questions

There are several open questions of general interest regarding thermal electron emission after photo-excitation. One is ionization of large molecules with photon energies larger than the ionization potential. For such systems the experimental interest has focused on state specific ionization, but an interesting question is if also such systems can emit thermal electrons. A second system of interest is fs-laser multiphoton ionization of atoms. For the rare gas atoms the photoelectron spectra are dominated by ATI-peaks and for atoms with closed electron shells the probability for a thermal process must be expected to be very low. But according to [62–64] electron recombination of highly charged ions result in a chaotic multielectron excitation. One could therefore suspect a similar behavior after intense laser excitation of atoms or atomic ions with many electrons in an outer non-filled shell, and a possible thermal emission process.

Acknowledgements

Many people have contributed to this work and I would now like to take the chance and express my gratitude.

I am grateful to Klavs Hansen who has been my supervisor for five years. Through these years your door has always been open, every day, for questions, discussions and guidance which is something I have appreciated very much. From you I have also learnt to look at my own and others' scientific results, interpretations and conclusions with a fair and critical eye.

Thanks to Eleanor Campbell who gave me the chance to do a PhD and has been my examiner for 98% of the time. Thanks for all help finishing the thesis, correcting my "swenglish" and solving the riddle of the mystic peaks.

I am also grateful to Dag Hanstorp for taking the job as my second examiner with short notice.

I would like to thank Martin Hedén for introducing me to the lab, teaching me how to run the machine and telling me about the lab-demons.

Thanks to Olof Johansson who joined me in the lab at the time of his master's project and wrote the inversion code.

I thank Alexander Bulgakov who has been a frequent guest in the lab for invaluable help in the installation and set up of the electron spectrometer.

Juraj Fedor and Jakob Stenfalk did a lot of work on the asymmetric electron distributions and came up with the interpretation.

Sophie Canton, a big set of applause for all good laughs in the lab even at times when there was only noise.

Motoshi Goto joined the group for two months in 2008 and will now continue my work. Thanks for great guiding in Tokyo! Seeing Tokyo from above was amazing.

I am grateful to Christian Bordas who gave us the drawings of the electron spectrometer, Fredrik Jonsson who made the necessary modifications and Jan-Åke Wiman who built it.

I also thank Mats Rostedt for solving technical problems regarding electronics, computers and cooling water. Heinrich Riedl for helping me getting the GHI-muck out of the chamber.

My room-mate, Erika Sundén, thank you for a good office atmosphere, danish-swedish translations and for being a MATLAB queen. :)

The lab crew Anton Lindahl, Pontus Andersson, Peter Klason, Johan Rohlén, Vladimir Popok, Saša Vučković, Martin Sveningsson, Martin Jönsson and all other past and present members of the former atomic physics group have made this to a pleasant workplace.

Finally I thank my parents and my love, Elisabeth, for supporting and encouraging me all the way to the finish line.

Mikael Kjellberg
Göteborg, February 2010

Bibliography

[1] J. Mauritsson, P. Johnsson, E. Mansten, M. Swoboda, T. Ruchon, A. L'Huillier, and K. J. Schafer, *Phys. Rev. Lett.*, **100**, 073003, (2008)

[2] M. Dantus, M. J. Rosker and A. H. Zewail, *J. Chem. Phys.*, **87**, 2395, (1987)

[3] B. H. Bransden and C. J. Joachain, *Physics of atoms and molecules. Second edition*, Pearson Education, (2003)

[4] M. Protopapas, C. H. Keitel and P. L. Knight *Rep. Prog. Phys*, **60**, 389, (1997)

[5] P. Agostini, F. Fabre, G. Mainfray, G. Petite and N. K. Rahman *Phys. Rev. Lett*, **42**, 1127, (1979)

[6] P. Agostini and L. F. DiMauro, *Contemp. Phys*, **49**, 179, (2008)

[7] M. J. DeWitt and R. J. Levis, *Phys. Rev. Lett.*, **81**, 5101, (1998)

[8] T. Hatamoto, M. Okunishi, T. Lischke, G. Prümper, K. Shimada, D. Mathur, and K. Ueda, *Chem. Phys. Lett*, **439**, 296, (2007)

[9] E. E. B. Campbell, K. Hoffmann, H. Rottke, and I. V. Hertel, *J. Chem. Phys*, **114**, 1716, (2001)

[10] P. Corkum, *Phys. Rev. Lett*, **71**, 1994, (1993)

[11] X. F. Li, A. L'Huillier, M. Ferray, L. A. Lompré and G. Mainfray, *Phys. Rev. A*, **39**, 5751, (1989)

[12] S. F. J. Larochelle, A. Talebpour and S. L. Chin, *J. Phys. B: At. Mol. Opt. Phys*, **31**, 1215, (1997)

[13] R. R. Freeman, P. H. Bucksbaum, H. Milchberg, S. Darack, D. Schumacher and M. E. Geusic, *Phys. Rev. Lett.*, **59**, 1092, (1987)

[14] R. R. Freeman and P. H. Bucksbaum, *J. Phys. B*, **24**, 325, (1991)

[15] H. G. Muller, H. B. van Linden van den Heuvell, P. Agostini, G. Petit, A. Antonetti, M. Franco and A. Migus, *Phys. Rev. Lett.*, **60**, 565, (1988)

[16] P. Agostini, P. Breger, A. L'Huillier, H. G. Muller, G. Petit, A. Antonetti and A. Migus, *Phys. Rev. Lett.*, **63**, 2208, (1989)

[17] V. Schyja, T. Lang and H. Helm, *Phys. Rev. A*, **57**, 3692, (1998)

[18] T. J. McIlrath, P. H. Bucksbaum, R. R. Freeman and M. Bashkansky, *Phys. Rev. A*, **35**, 4611, (1987)

[19] L. V. Keldysh, *Sov. Phys. JETP*, **20**, 1307, (1965)

[20] S. M. Hankin, D. M. Villeneuve, P. B. Corkum and D. M. Rayner *Phys. Rev. A*, **64**, 013405, (2001)

[21] S. M. Hankin, D. M. Villeneuve, P. B. Corkum and D. M. Rayner *Phys. Rev. Lett*, **84**, 5082, (2000)

[22] M. Lezius, V. Blanchet, M. Yu Ivanov and A. Stolow, *J. Chem. Phys.*, **117**, 1575, (2002)

[23] D. Mathur, T. Hatamoto, M. Okunishi, G. Prümper, T. Lischke, K. Shimada and K. Ueda, *J. Phys. Chem*, **111**, 9299, (2007)

[24] M. Lezius, V. Blanchet, D. M. Rayner, D. M. Villeneuve, A. Stolow and M. Yu Ivanov, *Phys. Rev. Lett.*, **86**, 51, (2001)

[25] M. J. DeWitt and R. J. Levis, *J. Chem. Phys.*, **110**, 11368, (1999)

[26] A. N. Markevitch, N. P. Moore and R. J. Levis, *Chem. Phys.*, **267**, 131, (2001)

[27] M. Murakami, R. Mizoguchi, Y. Shimada, T. Yatsuhashi and N. Nakashima, *J. Chem. Phys.*, **403**, 238, (2005)

[28] M. Murakami, M. Tanaka, T. Yatsuhashi and N. Nakashima, *J. Chem. Phys.*, **126**, 104304, (2007)

[29] V. R. Bhardwaj, P. B. Corkum and D. M. Rayner *Phys. Rev. Lett.*, **93**, 043001-1, (2004)

[30] M. Tchaplyguine, K. Hoffmann, O. Dühr, H. Hohmann, G. Korn, H. Rottke, M. Wittmann, I. V. Hertel and E. E. B. Campbell, *J. Chem. Phys.*, **112**, 2781, (2000)

[31] I. Shchatsinin, T. Laarmann, G. Stibenz, G. Steinmeyer, A. Stalmashonak, N. Zhavoronkov, C. P. Schulz and I. V. Hertel, *J. Chem. Phys*, **125**, 194320, (2006)

[32] I. V. Hertel, I. Shchatsinin, T. Laarmann, N. Zhavoronkov and C. P. Schulz, *Phys. Rev. Lett*, **102**, 023003-1, (2009)

[33] I. Shchatsinin, T. Laarmann, N. Zhavoronkov, C. P. Schulz and I. V. Hertel, *J. Chem. Phys*, **129**, 204308, (2008)

[34] E. E. B. Campbell, K. Hansen, K. Hoffmann, G. Korn, M. Tchaplyguine, M. Wittmann and I. V. Hertel, *Phys. Rev. Lett.*, **84**, 2128, (2000)

[35] K. Hansen, K. Hoffmann and E. E. B. Campbell, *J. Chem. Phys.*, **119**, 2513, (2003)

[36] K. Hosaka, R. Itakura, K. Yokoyama, K. Yamanouchi and A. Yokoyama, *Chem. Phys. Lett.*, **475**, 19, (2009)

[37] Q. Wang, D. Wu, M. Jin, F. Liu, F. Hu, X. Cheng, H. Liu, Z. Hu, D. Ding, H. Mineo, Y. A. Dyakov, A. M. Mebel, S. D. Chao and S. H. Lin, *J. Chem. Phys.*, **129**, 204302, (2008)

[38] Q. Wang, D. Wu, D. Zhang, M. Jin, F. Liu, H. Liu, Z. Hu, D. Ding, H. Mineo, Y. A. Dyakov, Y. Teranishi, S. D. Chao, A. M. Mebel and S. H. Lin, *J. Chem. Phys.*, **113**, 11805, (2009)

[39] M. Tanaka, M. Kawaji, T. Yatsuhashi and N. Nakashima, *J. Phys. Chem. A*, **113**, 12062, (2009)

[40] G. G. Paulus, W. Nicklich, H. Xu, P. Lambropoulos and H. Walther, *Phys. Rev. Lett.*, **72**, 2851, (1994)

[41] I. V. Hertel, H. Steger, J. de Vries, B. Weisser, C. Menzel, B. Kamke and W. Kamke, *Phys. Rev. Lett*, **68**, 784, (1992)

[42] J. M. Weber, K. Hansen, M. -W. Ruf, and H. Hotop, *Chem. Phys.*, **239**, 271, (1998)

[43] D. S. Bethune, G. Meijer, W. C. Tang, H. J. Rosen, W. G. Golden, H. Seki, C. A. Brown and M. S. de Vries, *Chem. Phys. Lett.*, **179**, 181, (1991)

[44] V. Weisskopf, *Phys. Rev.*, **52**, 295, (1937)

[45] J. U. Andersen, E. Bonderup and K. Hansen, *J. Phys. B: At. Mol. Opt. Phys*, **35**, R1, (2002)

[46] E. E. B. Campbell, G. Ulmer, and I. V. Hertel, *Phys. Rev. Lett*, **67**, 1986, (1991)

[47] C. Lifshitz, *Int. J. Mass. Spectrom.*, **200**, 423, (2000)

[48] D. Ding, R. N. Compton, R. E. Haufler and D. L. Huestis, *J. Phys. Chem.*, **97**, 2500, (1993)

[49] B. Baguenard, J. C. Pinaré, C. Bordas and M. Broyer, *Phys. Rev. A*, **63**, 023204-1, (2001)

[50] K. Hansen and O. Echt, *Phys. Rev. Lett.*, **78**, 2337, (1997)

[51] J. U. Andersen, E. Bonderup, P. Hvelplund, B. Liu, U. V. Pedersen and S. Tomita, *Eur. Phys. J. D*, **24**, 191, (2003)

[52] K. Hansen, E. E. B. Campbell and O. Echt, *Int. J. Mass. Spec*, **252**, 79, (2006)

[53] F. Lépine and C. Bordas, *Phys. Rev. A*, **69**, 053201-1, (2004)

[54] R. Schlipper, R. Kusche, B. v. Issendorff and H. Haberland, *Appl. Phys. A*, **72**, 255, (2001)

[55] M. Maier, M Astruc Hoffmann and B. von Issendorff, *New J. Phys.*, **5**, 3.1, (2003)

[56] S. I. Anisimov, B. L. Kapeliovich, T. L. Perel'man, *Sov. Phys. JETP*, **39**, 375, (1974)

[57] M. Perner, S. Gresillon, J. März, G. von Plessen, J. Feldmann, J. Porstendorfer, K. -J. Berg and G. Berg *Phys. Rev. Lett*, **85**, 792, (2000)

[58] B. Rethfeld, A. Kaiser, M. Vicanek and G. Simon, *Phys. Rev. B*, **65**, 214303, (2002)

[59] J. Wang and C. Guo, *Phys. Rev. B*, **75**, 184304, (2007)

[60] A. Gloskovskii, D. A. Valdaitsev, M. Cinchetti, S. A. Nepijko, J. Lange, M. Aeschlimann, M. Bauer, M. Klimenkov, L. V. Viduta, P. M. Tomchuk and G. Schönhense, *Phys. Rev. B*, **77**, 195427, (2008)

[61] A. A. Unal, A. Stalmashonak, G. Seifert and H. Graener, *Phys. Rev. B*, **79**, 115411, (2009)

[62] G. F. Gribakin, A. A. Gribakina and V. V. Flambaum, *Aust. J. Phys.*, **52**, 443, (1999)

[63] V. V. Flambaum, A. A. Gribakina, G. F. Gribakin and C. Harabati, *Phys. Rev. A*, **66**, 012713, (2002)

[64] G. F. Gribakin and S. Sahoo *J. Phys. B*, **36**, 3349, (2003)

[65] W. C. Wiley and I. H. McLaren, *Rev. Sci. Inst.*, **26**, 1150, (1955)

[66] M. Hedén, *Optical excitation and decay dynamics of fullerenes*, Ph.D thesis, Göteborg University, 2005

[67] H. Helm, N. Bjerre, M. J. Dyer, D. L. Huestis and M. Saeed, *Phys. Rev. Lett.*, **70**, 3221, (1993)

[68] A. T. J. B. Eppink and D. H. Parker, *Rev. Sci. Instrum.*, **68**, 3477, (1997)

[69] B. Baguenard, J. B. Wills, F. Pagliarulo, F. Lépine, B. Climen, M. Barbaire, C. Clavier, M. A. Lebeault and C. Bordas, *Rev. Sci. Instrum.*, **75**, 324, (2004)

[70] C. Bordas, F. Paulig and H. Helm, D. L. Huestis, *Rev. Sci. Instrum.*, **67**, 2257, (1996)

[71] O. Johansson, *Ionization of C_{60} using velocity map imaging photoelectron spectroscopy*, Master's thesis, University of Gothenburg, 2007

[72] E. Cormier, P. -A. Hervieux, R. Wiehle, B. Witzel and H. Helm *Eur. Phys. J. D*, **26**, 83, (2003)

[73] Gerald Jung, private communication.

[74] C. Rullière (Ed.), *Femtosecond laser pulses. Principle and methods. Second edition*, Springer, (2005)

[75] T. P. Martin, U. Näher, H. Schaber and U. Zimmermann, *Phys. Rev. Lett.*, **70**, 3079, (1993)

[76] K. Hansen and E. E. B. Campbell, *J. Chem. Phys.*, **104**, 5012, (1996)

[77] J. de Vries, H. Steger, B. Kamke, C. Menzel, B. Weisser, W. Kamke and I. V. Hertel *Phys. Rev. Lett.*, **118**, 159, (1992)

[78] S. Díaz-Tendero, M. Alcamí and F. Martín, *J. Chem. Phys.*, **119**, 5545, (2003)

[79] S. Tomita, J. U. Andersen, K. Hansen and P. Hvelplund, *Chem. Phys. Lett.*, **382**, 120, (2003)

[80] M. Hedén, K. Hansen, F. Jonsson, E. Rönnow, A. Gromov and E. E. B. Campbell *J. Chem. Phys.*, **123**, 044310, (2005)

[81] M. Boyle, K. Hoffmann, C. P. Schulz, I. V. Hertel, R. D. Levine and E. E. B. Campbell, *Phys. Rev. Lett.*, **87**, 273401, (2001)

[82] E. Clar, J. M. Robertson, R. Schloegl and W. Schmidt, *J. Am. Chem. Soc.*, **103**, 1320, (1981)

[83] R. Boschi, J. N. Murrell and W. Schmidt, *Faraday Discuss. Chem. Soc.*, **54**, 116, (1972)

[84] J. W. Hager and S. C. Wallace, *Anal. Chem.*, **60**, 5, (1988)

[85] M. Castillejo, S. Couris, E. Koudoumas and M. Martín, *Chem. Phys. Lett.*, **289**, 303, (1998)

[86] K. W. D. Ledingham, D. J. Smith, R. P. Singhal, T. McCanny, P. Graham, H. S. Kilic, W. X. Peng, A. J. Langley, P. F. Taday and C. Kosmidis, *J. Phys. Chem. A*, **103**, 2952, (1999)

[87] W. Branz, N. Malinowski, A. Enders and T. P. Martin, *Phys. Rev. B*, **66**, 094107, (2002)

[88] C. Yeretzian, K. Hansen, F. Diederich and R. L. Whetten, *Nature*, **359**, 44, (1992)

[89] C. Yeretzian, K. Hansen, F. Diederich and R. L. Whetten, *Z. Phys. D*, **26**, 300, (1993)

[90] R. D. Beck, P. Weis, G. Bräuchle and M. M. Kappes, *J. Chem. Phys.*, **100**, 262, (1994)

[91] F. Rohmund, A. V. Glotov, K. Hansen and E. E. B. Campbell, *J. Phys. B: At. Mol. Opt. Phys.*, **29**, 5143, (1996)

[92] F. Rohmund, E. E. B. Campbell, O. Knospe, G. Seifert and R. Schmidt, *Phys. Rev. Lett.*, **76**, 3289, (1996)

[93] G. Seifert, R. Gutierrez and R. Schmidt, *Phys. Lett. A*, **211**, 357, (1996)

[94] M. Hedén, K. Hansen and E. E. B. Campbell, *Phys. Rev. A*, **71**, 055201, (2005)

[95] B. Manil, L. Maunoury, B. A. Huber, J. Jensen, H. T. Schmidt, H, Zettergren, H. Cederquist, S. Tomita and P. Hvelplund, *Phys. Rev. Lett.*, **91**, 215504, (2003)

Paper I

Paper II

Paper III

Paper IV

Paper V